2012

EXPERIMENTAL BENCHMARKING OF SURFACE TEXTURED LIP SEAL MODELS

Wei Li
University of Kentucky, liweiseu@gmail.com

STUDENT AGREEMENT:

I represent that my thesis or dissertation and abstract are my original work. Proper attribution has been given to all outside sources. I understand that I am solely responsible for obtaining any needed copyright permissions. I have obtained and attached hereto needed written permission statements(s) from the owner(s) of each third-party copyrighted matter to be included in my work, allowing electronic distribution (if such use is not permitted by the fair use doctrine).

I hereby grant to The University of Kentucky and its agents the non-exclusive license to archive and make accessible my work in whole or in part in all forms of media, now or hereafter known. I agree that the document mentioned above may be made available immediately for worldwide access unless a preapproved embargo applies.

I retain all other ownership rights to the copyright of my work. I also retain the right to use in future works (such as articles or books) all or part of my work. I understand that I am free to register the copyright to my work.

REVIEW, APPROVAL AND ACCEPTANCE

The document mentioned above has been reviewed and accepted by the student's advisor, on behalf of the advisory committee, and by the Director of Graduate Studies (DGS), on behalf of the program; we verify that this is the final, approved version of the student's dissertation including all changes required by the advisory committee. The undersigned agree to abide by the statements above.

Wei Li, Student

Dr. Lyndon S. Stephens, Major Professor

Dr. James M. McDonough, Director of Graduate Studies

EXPERIMENTAL BENCHMARKING OF SURFACE TEXTURED LIP SEAL MODELS

DISSERTATION

A dissertation submitted in partial fulfillment of the
requirements for the degree of Doctor of Philosophy
in the Department of Mechanical Engineering in the College of Engineering
at the University of Kentucky

By
Wei Li
Lexington, Kentucky

Director: Dr. Lyndon S. Stephens, Professor of Mechanical Engineering
Co-director: Dr. Jonathan F. Wenk, Professor of Mechanical Engineering

ABSTRACT OF DISSERTATION

EXPERIMENTAL BENCHMARKING OF SURFACE TEXTURED LIP SEAL MODELS

A thorough investigation on the existing hydrodynamic lubrication theories and the reverse pumping theories for the conventional lip seal is conducted. On that basis, the algorithms and the methods used in the numerical modeling of the conventional lip seal are modified and applied to the study of the lip seal running against surface textured shafts. For each step of the study, the numerical model is benchmarked against the experimental results. Important physical mechanisms which explain the reverse pumping ability of the triangular surface structures are revealed. Meanwhile, the accuracy of the numerical model is tested. In general, the numerical simulation results match the experimental observation well. However, there are several important discrepancies. For each discrepancy the possible causes are discussed, which benefits the further attempts of the modeling work on the lip seal running against surface textured shafts. The conclusions of this study themselves can be used as a guidance to the design of the surface textured shafts for the lip seal applications. Finally the limitation of the current theories and the modeling methods are discussed and reasonable improvements which can be done are proposed for the future work.

KEYWORDS: Lip Seal, Hydrodynamic Lubrication, Reverse Pumping, Surface Texturing, Experimental Benchmarking

Wei Li

_____

28th November, 2012

_____

(Date)

EXPERIMENTAL BENCHMARKING OF SURFACE TEXTURED LIP SEAL MODELS

By

Wei Li

(Dr. Lyndon S. Stephens)

Director of Dissertation

(Dr. Jonathan F. Wenk)

Co-Director of Dissertation

(Dr. James M. McDonough)

Director of Graduate studies

28th November, 2012

(Date)

ACKNOWLEGMENTS

I would like to thank my advisor, Dr. L. S. Stephens and my co-advisor J. F. Wenk for their support, motivation and guidance during my study and research at the University of Kentucky. I would like to thank my dissertation committee members: Dr. Alexandre Martin, Dr. Keith Rouch and Dr. Qiang Ye. I also wish to thank Dr. James McDonough and Dr. Tim Wu for their additional and important guidance and help. I would like to thank K. H. Warren and K. Vetrivel who I am working with for the experimental testing. I would like to thank the Timken Company for their assistance in this project.

I would also thank to my family members especially my wife Lu Huang for their unconditional and persisting support and encouragement. I would like to thank my friends and members of the Bearing and Seals Laboratory who make my study at the University of Kentucky pleasant and memorable.

TABLE OF CONTENTS

LIST OF FIGURES

LIST OF TABLES

CHAPTER 1 — INTRODUCTION

1.1 Introduction to Tribology

Tribology studies the interacting surfaces in relative motion including lubrication, friction and wear. Having a great diversity, tribological systems include the piston ring, the journal bearing, the thrust bearing, mechanical face seal and the radial lip seal, just to name a few. The conventional tribological problems can be classified in the following categories.

Hydrodynamic lubrication:

This type of system refers to the complete separation of the two sliding surfaces by a layer of lubricant (oil) so that there is no direct solid contact. Hydrodynamic lubrication usually happens when the working load for the bearing components is relatively small or the sliding speed is high. Figure 1.1.1 shows the hydrodynamic lubrication case between two hard sliding surfaces like the shaft and the journal bearing.

Elasto-hydrodynamic lubrication (EHL):

EHL is similar to hydrodynamic lubrication except that one or both of the mating surfaces deform under the fluid pressure or the contact pressure. The EHL can be divided into the soft- EHL and the hard-EHL. Soft-EHL is when one of the surfaces deforms in bulk like rubber or plastic. Where hard-EHL is when both of the surfaces deform in

non-conformed contacts resulting in the Hertzian contact sphere like in gears. The study of the lip seal belongs to the soft-EHL. The deformation of the surface and the fluid (oil) flow mutually influence each other as the surface deformation changes the oil film thickness and in return the oil film pressure determines the surface deformation.

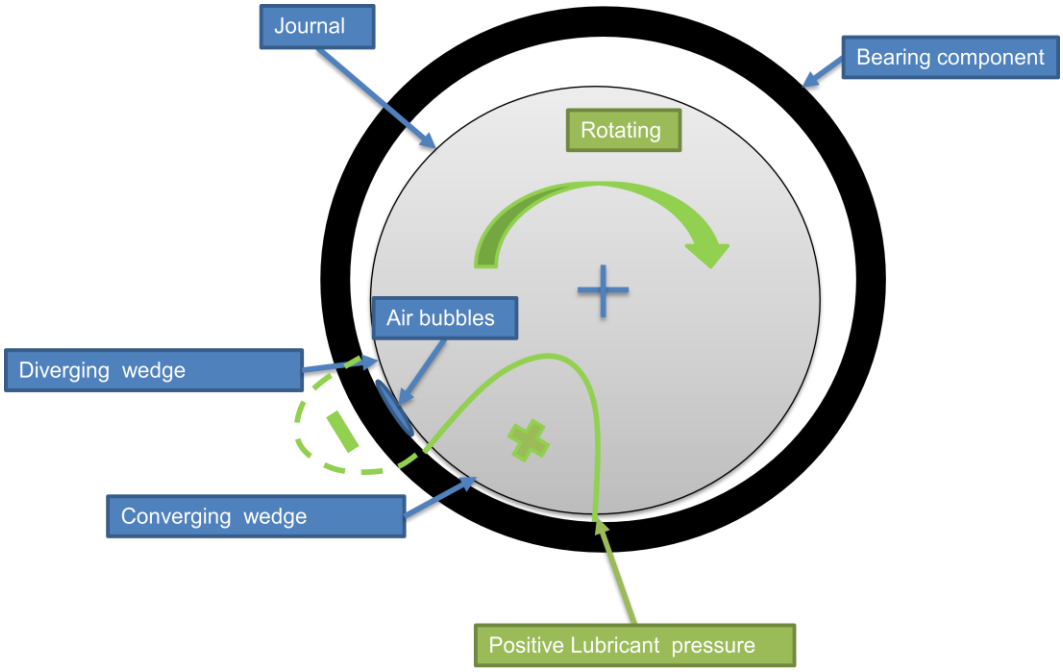

Figure 1.1.1 Hydrodynamic lubrication for the journal bearing (caused by the eccentricity)

The coupling property makes thEHL analysis more complicated. EHL usually happens between a hard sliding surface like the steel shaft and a soft sliding surface like the elastomer of the lip seal. EHL model needs at least two sub models: a fluid dynamics model for determining the oil film pressure and a solid mechanics model for determining the deformation of the soft surface. These two models are coupled to ensure the continuity of the pressure at the fluid-solid interface.

Mixed elasto-hydrodynamic lubrication (Mixed-EHL):

Mixed-EHL is a special case of the EHL. In mixed-EHL partial contact happens between the two sliding surfaces because of a high working load or a low operating speed. Oil film is ruptured locally in the mixed-EHL due to the contact between two surfaces. A fluid dynamics model, a solid deformation model plus a contact model are indispensable in the Mixed-EHL analysis. These three sub models are coupled as it is in the EHL.

A key feature of the hydrodynamic lubrication is the separation of the two sliding surfaces by the hydrodynamic lifting force generated by a thin lubricant film. The hydrodynamic lifting force is mainly caused by the wedge effect. Figure 1.1.1 shows a journal bearing system. During the operation, the eccentricity of the shaft leads to a non-uniform lubricant film distribution. The relative motion of the surface and the viscous shearing force of the fluid drag/squeeze the lubricant into the converging wedge causing the rise of the fluid pressure. The fluid pressure will drop when the lubricant reaches the diverging wedge. The fluid pressure distribution is not perfectly anti-symmetrical on the two wedges as shown in Figure 1.1.1. Thus a net supporting force is generated. Another important physical phenomenon "cavitation" (vapor bubbles) contributes to an extra portion of supporting force. As the fluid pressure drops, cavitation forms due to the vaporization of the lubricant. The pressure within the vapor bubbles is usually constant and is known as the "cavitation pressure" or the "cavitation threshold pressure" P_c, for example $P_c = 0$ Pa. Cavitation aggravates the asymmetry of the fluid

pressure distribution by truncating the negative fluid pressure and thus provides an extra net supporting force. Figure 1.1.2 from Shen [1] demonstrates the link between the cavitation and the extra supporting force.

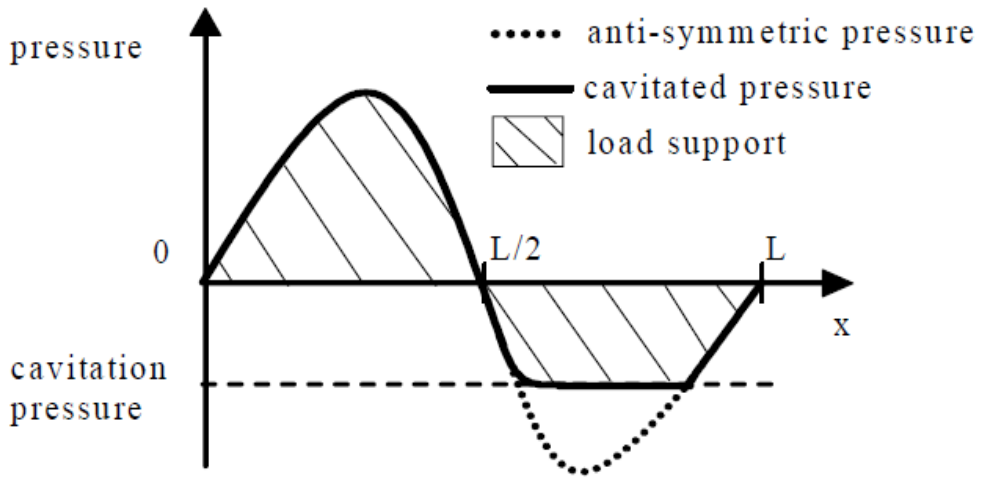

Figure 1.1.2 Anti-symmetric pressure distribution truncated by the cavitation (from Shen [1])

Besides the eccentricity, the surface irregularities could also trigger the hydrodynamic lubrication effect as shown in Figure 1.1.3. Surface asperities act just like many mini sliding bearings blocking the local flow and elevating the local fluid pressure. Inter-asperity cavitation is also observed during the experiment and is believed to be important to the load carrying ability of the rough surface. Surface roughness induced hydrodynamic lubrication effect is widely accepted as the main working mechanism of the radial lip seal. The hydrodynamic lubrication effect of the radial lip seal is one of the major topics of this study.

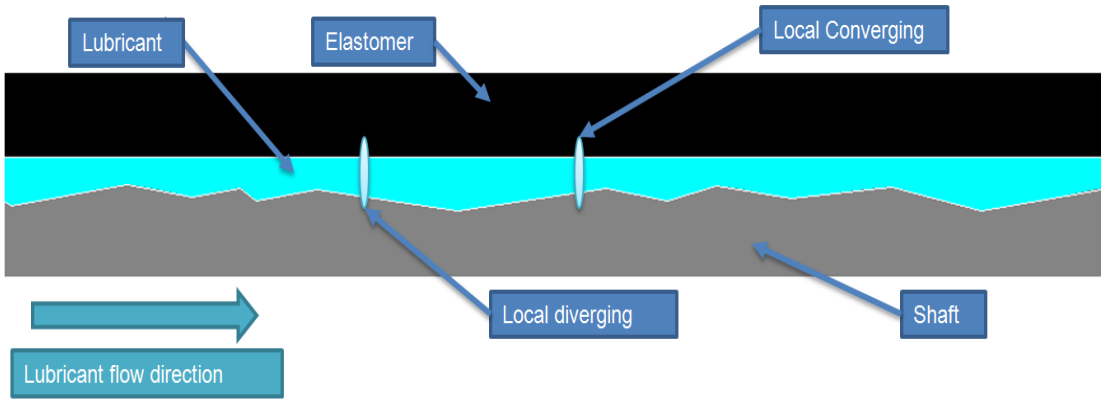

Figure 1.1.3 Hydrodynamic lubrication caused by the surface roughness

1.2 Introduction to Conventional Radial Lip Seal

Radial lip seal is widely used in industry to prevent the leakage of the lubricant and keep the contamination out of the lubrication system. Figure 1.2.1 (a) shows the structure and the sub components of the radial lip seal. Figure 1.2.1 (b) shows the lip seal in pair with its mating shaft. A conventional lip seal is composed of a rigid steel frame ring, a rubber elastomer ring and a garter spring. After the shaft is inserted into the lip seal, the elastomer of the lip seal is tightly fitted onto the shaft by the sealing force which is generated by the interference fit and the garter spring, as shown in Figure 1.2.2 (b). When the shaft starts to rotate, a hydrodynamic lifting force generates and tends to separate the elastomer from the shaft as shown in Figure 1.2.2 (c). In the beginning stage, the sealing force is too large for the hydrodynamic lifting force to counterbalance it. Consequently there is solid contact between the elastomer tip and the shaft. The total sealing force gradually decreases during the operation due to the wear of the elastomer, which leads to an increase in elastomer surface roughness. A microscopic study shows that many more

surface asperities formed on the elastomer surface because of the wear while the shaft surface becomes smoother because of the polishing effect. The beginning stage last for 20-100 hours and is called “run in” stage or “break in” stage Horve [2]. Figure 1.2.3 is a photo of the elastomer surface taken after the “break in” stage using Scanning Electron Microscope (SEM) by KanaKasabai [3]. In Figure 1.2.3 (a) the wear scar on the elastomer as well as (b) the surface cavities or (c) asperities formed during the “break in” staged can be seen.

After the “break in” stage, the rough elastomer surface eventually generates sufficient hydrodynamic lifting force to separate the elastomer from the shaft. From this point, it is assumed that the behavior of the lubricant is dominated by the hydrodynamic lubrication theory and the Reynolds equation could be used for the fluid calculation (see chapter 4 for details). It is also recognized that after the “break in” stage, the lip seal enters its functioning stage and provides a sealing ability (reverse pumping oil from the atmosphere side to the oil reservoir side shown in Figure 1.2.1 (a)) which is essentially the major function of the lip seal. There are many theories trying to explain the reverse pumping ability of the conventional lip seal during the functioning stage. The most popular theory is that after being sheared by the fluid viscous shear stress, the surface roughness on the elastomer forms the vane-like reverse pumping paths (see Chapter 2 for details). Another theory is related to the misalignment of the sealing ring, which will lead to a reciprocal motion of the shaft relative to the sealing ring. This reciprocal motion will lead to a reverse pumping effect just like the screw pumper (see Chapter 2 for details).

Because of the reverse pumping ability of the lip seal, the lubricant oil is retained within the sealing zone and keeps the sealing zone lubricated. “Reverse pumping” of the lip seal is one of the major topics of this study. The functioning stage of the conventional lip seal usually lasts for hundreds or thousands of hours. Ultimately the lip seal fails and a large leakage happens because the elastomer material has hardened and cracked due to thermal effect, chemical reaction or fatigue.

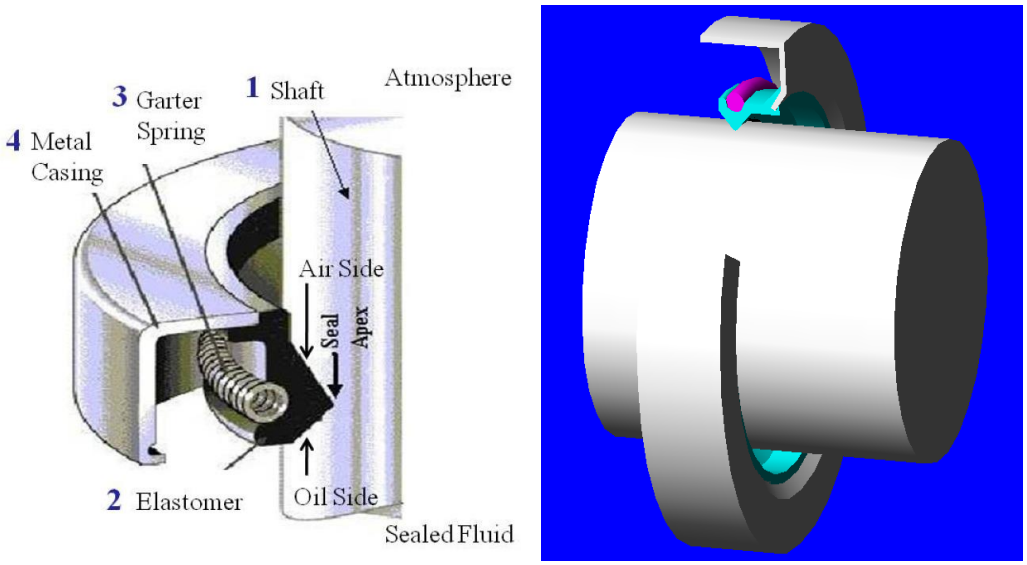

(a) (b)

Figure 1.2.1 (a) Components of the lip seal (from Chicago Rawhide), (b) lip seal and its mating shaft

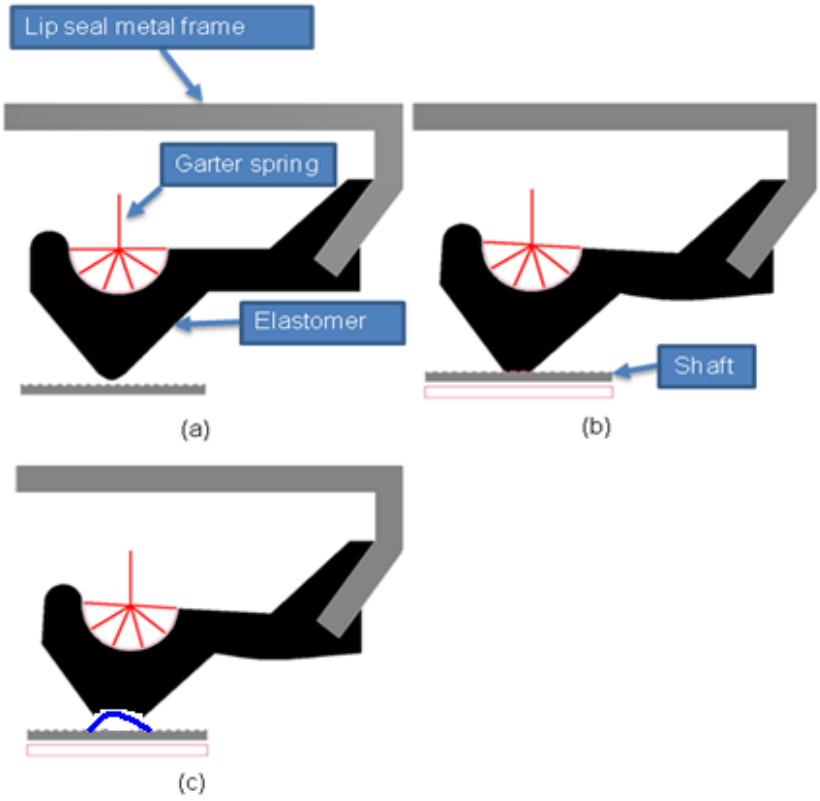

Figure 1.2.2 Demonstration of the operation of the lip seal

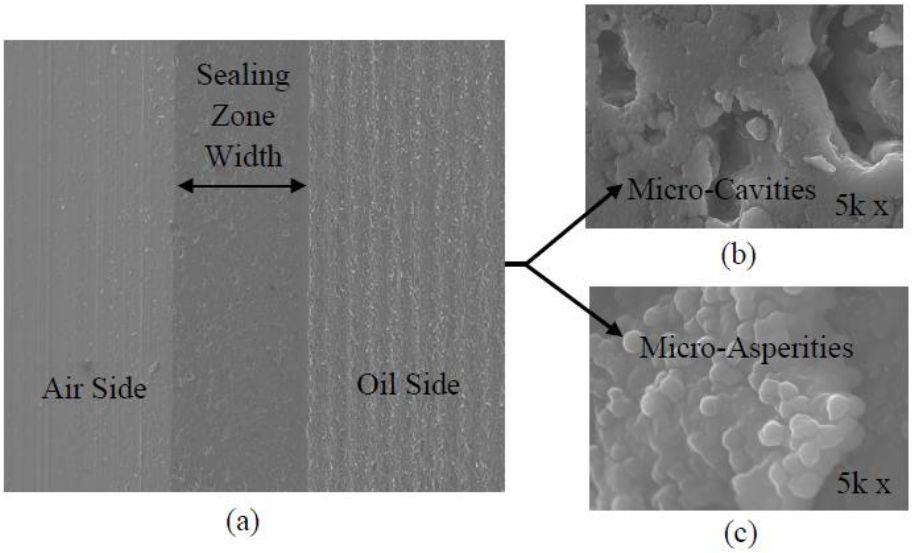

Figure 1.2.3 (a) Wear scar on the elastomer (b) Micro-cavities c) Micro-asperities (from KanaKasabai [3])

1.3 Surface Texturing

Inspired by the hydrodynamic lubrication theory and the natural reverse pumping theory for the conventional lip seal, many researchers and laboratories attempt to enhance the performance of the bearings and the seals with surface texturing. For example, Etsion et al. [4] used laser surface texturing (LST) technology to improve the quality of different bearing and sealing products. Figure 1.3.1 shows the laser textured surface of a bearing component. Stephens et al. [5,6] developed a method to produce deterministic surface textures with a modified LIGA technique or ultraviolet photolithography technique at the University of Kentucky. Figure 1.3.2 shows the hexagonal surface asperities produced by the modified LIGA technique. Hass et al. [7] also used laser texturing technique to process the mating shaft for the conventional lip seal (see Figure 2.5.1). The surface textures could interfere with the fluid dynamics of the lubricant to provide more hydrodynamic lifting force and to control the flow direction of the lubricant. Some experiments conducted have proven that properly designed surface textures on the shaft could enhance the forward pumping effect (leakage) or the backward pumping (reverse pumping) effect of the lip seal and simultaneously reduce the friction.

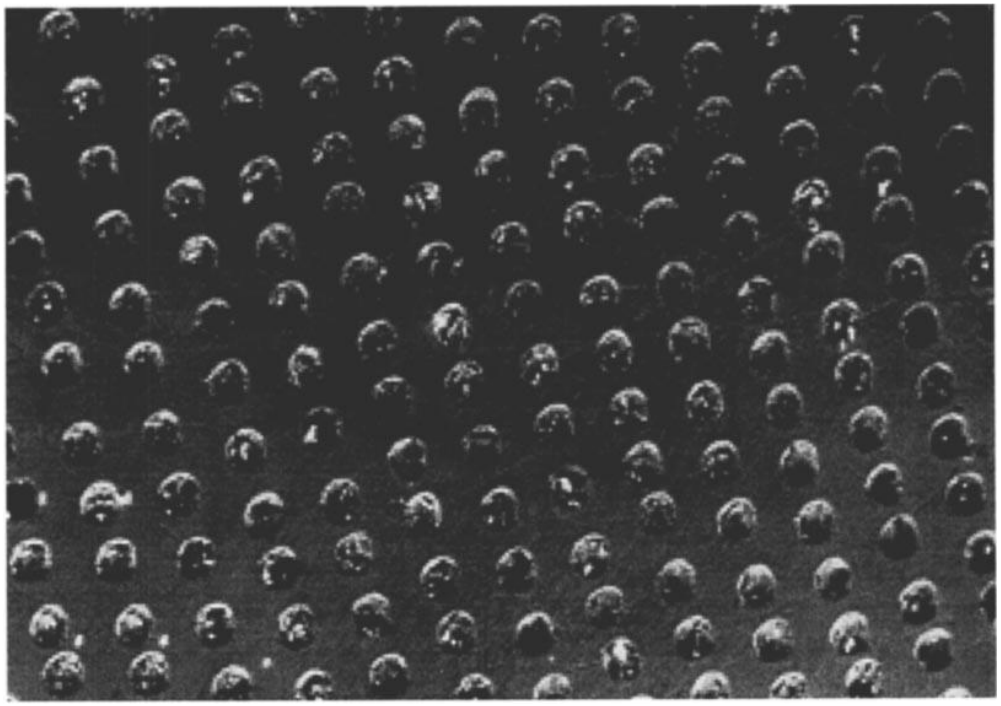

Figure 1.3.1 Laser textured bearing surface (from Etsion [4])

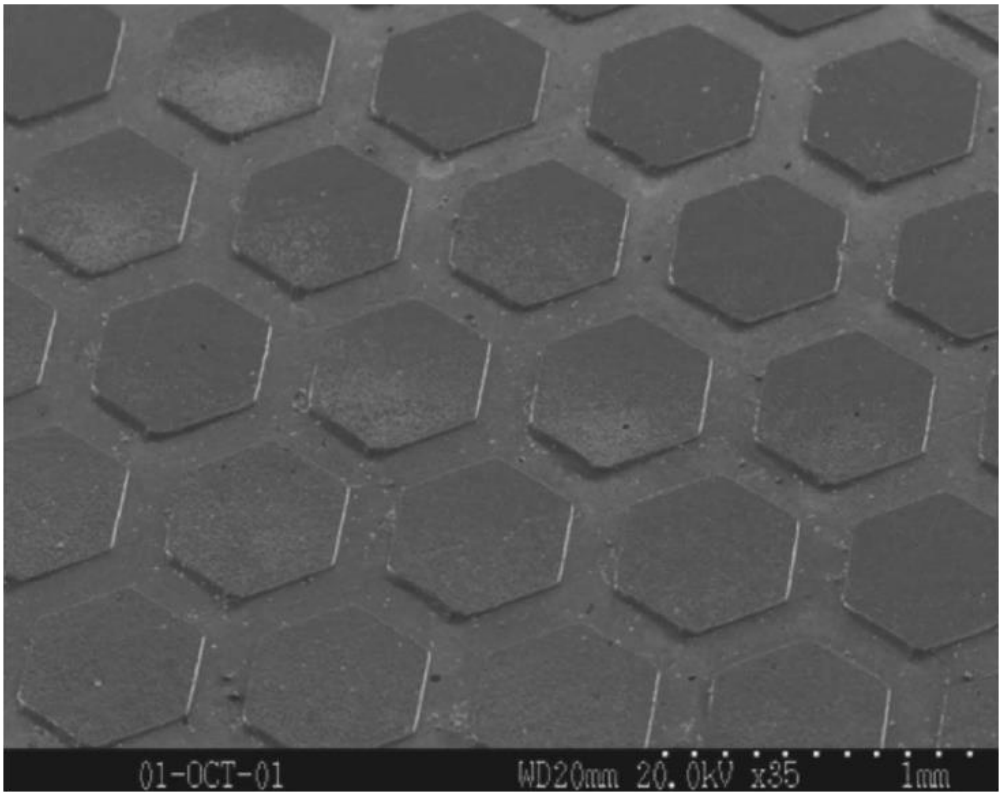

Figure 1.3.2 Hexagonal surface textures made by LIGA (from [5-6])

1.4 Research Objectives

The research objective of this study is to compare numerical models and experimental results of the radial lip seal running against surface textured shaft. Pilot research has thoroughly studied the conventional lip seal running against smooth shaft and reveals the mechanisms for both hydrodynamic lubrication and reverse pumping ability of the conventional lip seal to a certain extent (the research related to the conventional lip seal is introduced in details in Chapter 2). Recently, several designs and experiments were conducted regarding the lip seal running against a surface textured shaft. Many interesting and important phenomena that are different from the conventional seals are observed. But there lacks a theoretical analysis which explains the experimental results. The experiment results also provide an opportunity for benchmarking the existing theories and the algorithms.

This research builds upon many existing theories and focuses on applying them to the numerical analysis of the radial lip seal running against surface textured shaft. The numerical analysis covers many important physics and phenomena including cavitation, hydrodynamic load carrying capacity and reverse pumping. The experimental results are used to benchmark the model for the analysis. It will be shown that the numerical analysis provides a general explanation to the experimental results. It will also be seen that the deficits of the current analysis approach are found through the investigation of the discrepancies between the numerical model and the experiment. The numerical model can be further improved based on these findings

1.5 Brief Summary of Each Chapter

Chapter 2 systematically reviews the research work that has been done by the pilot researchers for the conventional lip seal and the surface texturing. It presents many theories and techniques useful for the modeling and the benchmarking work in this study.

Chapter 3 introduces the solid mechanics model employed by this study including fundamentals for the finite element method, incremental scheme for the nonlinear finite element analysis and a contact algorithm specifically designed for this study based on the linear finite element method.

Chapter 4 focuses on the fluid dynamics model. Basic assumptions for the lubrication problem are given. On that basis, the governing equation, Reynolds equation including the JFO cavitation condition, is given. Further, the numerical aspects necessary for solving the Reynolds equation are inspected.

In Chapter 5 Experimental results are used to benchmark the model introduced in the previous chapters. Important physical mechanisms explaining the experimental results are revealed. Discrepancies between the experiment and the model are well discussed.

In Chapter 6 Conclusions are given. Novel findings for the lip seal running against surface textured shaft are outlined. Recommendations are given for some future reasonable improvements.

CHAPTER 2 — LITERATURE REVIEW

2.1 Working Mechanisms of the Conventional Radial Lip Seal

Though the radial lip seal has been used and studied for a long time, a comprehensive and thorough understanding of its behavior has not been reached. This is because the physical mechanisms governing the behavior of the radial lip seal are complicated, hard to observe and coupled. Thus an analytical or a numerical tool for the design of the lip seal is absent from the choices of the tribology engineers. But accumulated knowledge from the experiments has advanced the understanding of the lip seal system since the 1950's. Two most important questions for the study of the radial lip seal are 1) whether there is a thin oil film separating the seal lip from the shaft (whether the seal lip is lubricated) 2) what mechanism causes the reverse pumping of the lip seal.

For the first question, Jagger [8-11] first demonstrated that during the functioning stage operation (after the "break in" stage) of the lip seal there is a continuous thin oil film separating the elastomer lip from the shaft surface. He came to this conclusion by measuring the oil film thickness indirectly through the viscous friction and directly through the capacitance of the oil film. The measured oil film thickness is typically 1~2μm. Following Jagger, Ogata [12], Gabelli [13], Poll [14], van Leeuwen and Wolfert [15] did similar oil film thickness measurement through electrical resistance, magnetic resistance, with a fluorescent image-processing technique and with an optical open-loop focus error signal detection technique respectively. These early experimental studies

proved the existence of a hydrodynamic lubricating oil film during the functioning stage operation of the lip seal and indicated that the oil film may be ruptured at a low operating speed.

There are two main theories explaining the existence of a continuous thin oil film. Ishiwata and Hiano [16-17] believe the thin oil film is supported by the shaft roughness. The studies by Jagger [11] [18] come to a different theory that the elastomer roughness supports the thin oil film. Jagger found that a shaft roughness of $0.25 - 0.5\ \mu m$ results in the best sealing performance. He also noticed the wear scar on the elastomer lip. He found that initial shaft roughness breaks through the rubber skin of the elastomer lip and creates many micro-asperities on the elastomer surface while the shaft surface gets polished and becomes smoother. This process is called "run in" or "break in" in the literature. Jagger concluded that the hydrodynamic lifting force should mainly be attributed to the elastomer roughness rather than the shaft roughness since the elastomer surface is much rougher than the shaft surface after the "break in" stage. Further studies by Hamilton [19], Johnston [20] and Horve [21] show that both the elastomer roughness and the shaft roughness contribute to the hydrodynamic lifting force for the lip seal. The surface roughness is believed to induce the hydrodynamic lubrication effect through two mechanisms: the mini inclined bearing and cavitation which have been introduced in section 1.1. The cavitation effect is observed in the experiments [19] [22-23].

For the second question, regarding the reverse pumping, there are also several theories. Initially it was popularly believed that surface tension prevents the lubricant

from leaking to the atmosphere until Kawahara and Hirabayshi reported [24-25] in 1978 that if the lip seal ring was installed reversely serious leakage would happen. Kawahara and Hirabayshi also found that the leakage rate of a conversely installed lip seal is dependent on the operating speed, viscosity, surface condition and the "break in" time. These findings indicate that hydrodynamic effect (fluid dynamics) rather than the surface tension is the main reason for the directional pumping ability of the lip seal. The studies by Horve [21] [26] show that a seal made of rubber material that easily generates surface roughness during the "break in" stage is more likely to pump reversely while the seal made of rubber that hardly generates surface roughness does not reversely pump well. Experiments like [15] [22] [27-28] also associated the reverse pumping effect of the lip seal to the surface roughness. Besides the surface roughness, research by Iwasaki [29] shows that a successful reverse pumping lip seal has a larger shear deformation on the elastomer surface at the location closer to the oil side than to the air side, which indicates an uneven axial sealing pressure distribution across the sealing zone. This uneven pressure distribution is later thought to be crucial to the reverse pumping ability of the lip seal. All these experimental studies show that the surface topology and the sealing pressure distribution play dominating roles in the reverse pumping phenomenon of the conventional lip seal. However, there still lacks comprehensive theories which could explain the joint influence of the above factors to reverse pumping.

Kammüller [30] and Müller [31] proposed a reverse pumping mechanism that the surface roughness on the elastomer sheared by the viscous friction force forms the

vane-like pumping paths as shown in Figure 2.1.1 The shear deformation of the elastomer surface is not uniform across the sealing zone because the sealing pressure distribution across the sealing zone is uneven. The maximum sealing pressure occurred at the location (sealing point) closer to the oil side. Consequently the maximum shearing deformation occurred closer to the oil side as shown in Figure 2.1.1. It is believed that this non-uniform shearing pattern leads to a net reverse pumping effect. Obviously, the uneven sealing pressure distribution is the key factor to this theory because the fluid shear stress is proportional to the normal sealing pressure as a higher local sealing pressure means a thinner local oil film and consequently means a stronger viscous shearing flow.

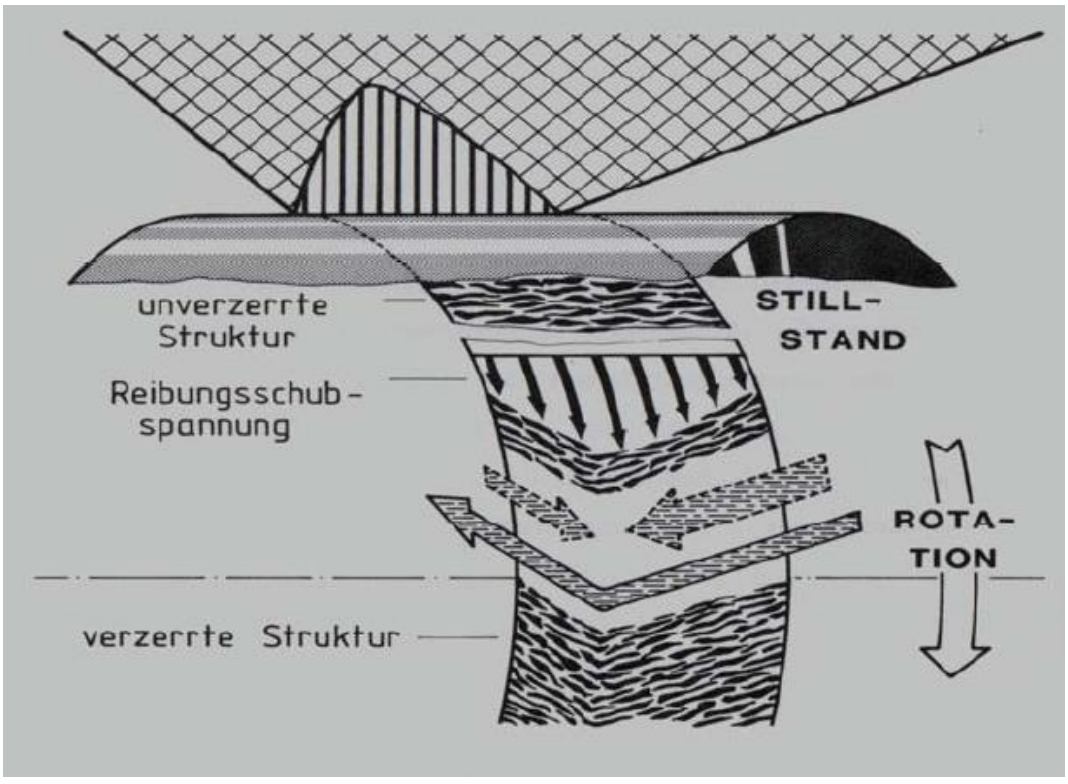

Figure 2.1.1 Reverse pumping caused by the uneven sealing pressure (from [30])

The reverse pumping is then generated because the sheared vane-like surface roughness disrupts the fluid dynamics of the thin oil layer. This theory is consistent with the experiment conducted by Kawahara and Hirabayshi [24-25], where if the lip seal is installed inversely, the pumping direction will also reverse because of the inversing of the sealing pressure distribution. It should be noted that the sealing pressure distribution across the sealing zone is an important design parameter for the lip seal. A desirable sealing pressure distribution can be achieved through modifying the geometry of the elastomer or adjusting the center line position (R value in Figure 2.1.2) of the garter spring.

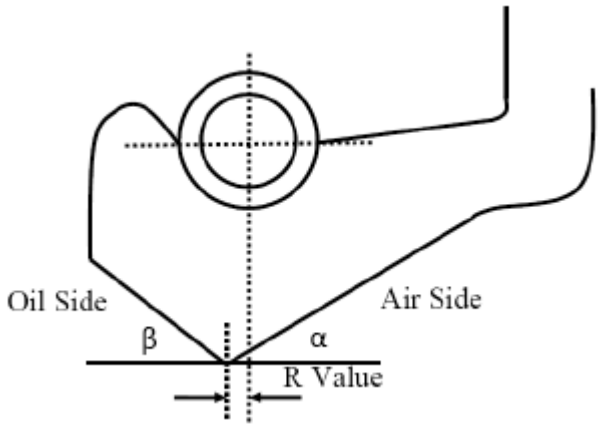

Figure 2.1.2 Design parameters of the lip seal (from KanaKasabai [3])

Another theory proposed by Horve [32] believes the misalignment of the sealing ring is an important reason for reverse pumping. As shown in Figure 2.1.3 the shaft has a reciprocal motion relative to the seal lip due to the misalignment (caused by the improper installation of the lip seal). When the shaft is moving inward, it directs the oil into the

sealing zone and creates reverse pumping. When the shaft is moving outward, it directs the oil out of the sealing zone and creates leakage. Because of the oil side angle (angle β in Figure 2.1.2) for the lip seal is steeper than the air side angle (angle α in Figure 2.1.2), more oil is drawn into the sealing zone than out of the sealing zone. In total, a net reverse pumping is expected. This theory is also consistent with the experiment conducted by Kawahara and Hirabayshi reported [24-25] where if the lip seal is installed inversely, the pumping direction will also reverse because of the inversing of the design angle on two sides of the sealing zone. Horve also believed that this theory could be used to explain why multiple circumferential sine waves designed by some seal manufacturers could enhance the reverse pumping ability. Because during operation the shaft has a similar reciprocal motion relative to these circumferential sine waves.

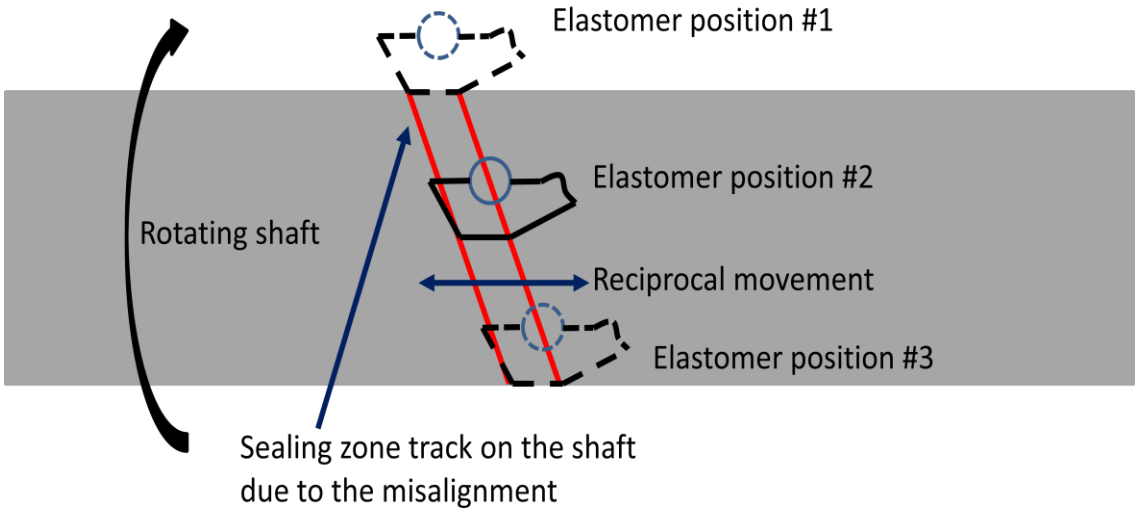

Figure 2.1.3 Reciprocal movement of the lip seal due to the misalignment

The experiments mentioned above, ran over a long period of time, gradually reveal the operation of the conventional lip seal from a historical point of view. The running of the lip seal can be generally divided into three stages. In the first stage, "break in" stage, the elastomer and the shaft surface are in contact under an excessively large sealing force due to the interference fit and the garter spring force. The elastomer tip gets worn and becomes rougher while the shaft surface is polished. In the second stage, functioning stage, the surface roughness on both the elastomer and the shaft generates sufficient hydrodynamic lifting force which separates the elastomer from the shaft and a thin oil film formed between the two mating surfaces. In the "functioning stage" the lip seal shows a reverse pumping ability due to the surface roughness, the uneven sealing pressure distribution and the possible misalignment. In the third stage, the seal material gradually loses its flexibility and cracks due to the thermal and chemical attack as well as fatigue. Eventually the seal fails.

2.2 Development of the Fluid Dynamics Model

After the theories explaining the working mechanisms have been developed, a numerical tool is needed for the theoretical study. The lubrication of the lip seal belongs to the Soft-EHL or mixed-EHL problem, depending on the stage in which the seal is operating. As introduced in Chapter 1 for a Soft-EHL problem, two sub models are need and for a Mixed-EHL problem, three sub models are needed. A fluid dynamics model is required in both cases.

Reynolds equation for the strong viscous flow as a branch of Computational Fluid Dynamics (CFD) is believed to govern the fluid behavior in the thin film lubrication problem. However, original Reynolds equation is not compatible with cavitation which is an important physical phenomenon. Half Sommerfeld and Reynolds cavitation conditions are first established to account for the cavitation. These two cavitation algorithms simply replace the fluid pressure below the "cavitaion threshold pressure" with the "cavitation threshold pressure", without any compensation, and are not mass conservative. However the mass conservation is especially important for the pumping rate calculation for the study of the radial lip seal. In 1957 and 1965 Jakobsson, Floberg [33] and Olsson [34] looked into the cavitation phenomenon separately, and established a theory collectively known as the JFO cavitation condition. Unlike previous cavitation conditions, the JFO cavitation condition preserves the continuity of the fluid within the cavitation region and is mass conservative. In 1974 and 1981 Elrod and Adams [35-36] extended the JFO theory by developing several numerical models which could automatically switch the form from full film flow (Elliptic PDE) to the cavitated flow (Hyperbolic PDE). Vijayaraghavan and Keith [37-40] made some further modifications to the JFO model by applying advanced CFD techniques. Brewe [41] used the JFO model to analyze dynamically loaded journal bearings. Salant and Flaherty [42-43] established a JFO model capable of predicting both the load support and the pumping rate when they applied the JFO theory to the radial lip seal.

Treating the surface roughness is another important issue for fluid dynamics model.

All the fluid dynamics models discussed above treat the surface roughness in a deterministic way by sampling the surface roughness with a certain resolution. The sampled surface topology, represented in the form of the grid function, is then inserted into the Reynolds equation in the form of the oil film thickness variation. Since the dimension of the surface roughness is on the level of a micrometer which is far smaller than the characteristic dimension of the lip seal, a very high grid density is required to capture the local oil film variation caused by the surface roughness when solving a deterministic Reynolds equation. To reduce the time of computation, researchers in the previously mentioned studies established statistical models which focus on the macro-level (statistical) influence of the surface roughness, and modify the Reynolds equation through several flow factors, but not through the high resolution sampling of the surface roughness. Tønder and Salant [44] 1992 first proposed the statistical model for lip seal. Patir and Cheng [45-46] 1978, Salant and Rocke [47] contributed to the statistical model separately. Harp and Salant [48] incorporated the JFO cavitation condition into the flow factor version Reynolds equation. The disadvantage of this model is that it could not provide detailed information about the local flow and might cause a certain level of error.

Recently the fast development of the high performance computation counter-balances the drawbacks of the deterministic model and helps the deterministic model to find more applications. The deterministic model has some further developments as Shi and Salant [49-50] developed a two fields (full lubrication field and cavitation field) steady state Reynolds equation which contains the JFO cavitation condition; Shen and

Salant [51-53] developed a transient Reynolds equation which considers both JFO cavitation condition and the squeeze oil film effect of the surface roughness on the shaft. The details for the fluid dynamics of the lubricant are given in Chapter. 4.

2.3 Development of the Solid Mechanics Model and the Contact Model

The other two sub models for the soft-EHL and the Mixed-EHL analysis are the solid mechanics model and the contact model. Since these two models are closely related, they are introduced together. Finite element method (FEM) is commonly used for the solid mechanics. It determines the deformation of the elastomer under the fluid pressure or the solid contact pressure.

Non-linear FEM is advanced in dealing with large displacement and large strain problem. When non-linear FEM is used, the entire deforming process is subdivided into many small incremental steps. For each step, the possible contact boundary is examined. The penalty method or the Lagrange multiplier method is used to prevent the penetration of the two contact faces and to calculate the contact nodal force. The non-linear FEM is usually accompanied by a serious mesh distortion and requires the remeshing technique in order to remedy the issue. The non-linear FEM is widely used in the contact analysis and dry wear analysis for the seal. For example, Sui, Pohl and Schomburg [54] used the non-linear FEM to simulate the wearing process of the PTFE seals. Yang, Wen and Tseng [55] used non-linear FEM to determine the contact status as well as the clearance between the elastomer and the shaft.

For the convenience of the contact searching and the remeshing, the total element number must be restricted to a certain level in the non-linear FEM. Too small element size or too many elements leads to a prohibitive computational time. Unfortunately, in the soft-EHL analysis or the mixed-EHL analysis a large element density is required on the elastomer-shaft contact interface as shown in Figure 2.3.1 to capture the local contact details of the surface roughness and the micro-level deformation of the elastomer. This property of the problem seriously limits the usage of the non-linear FEM in the soft-EHL analysis or the mixed-EHL analysis.

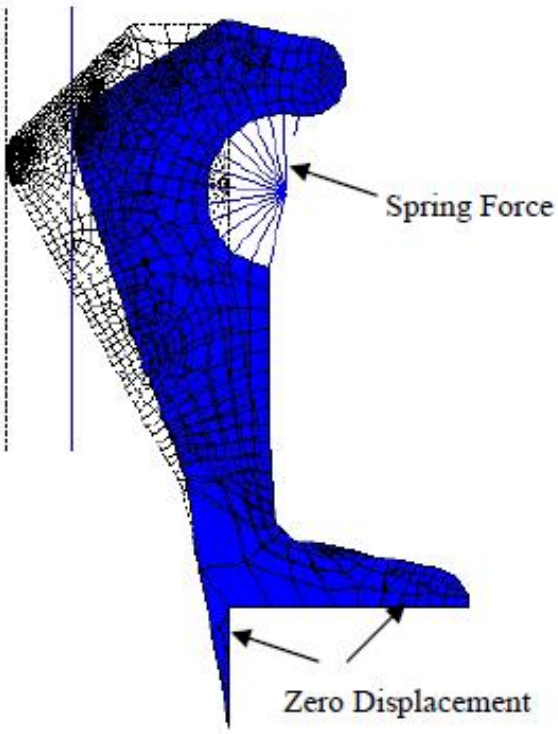

Figure 2.3.1 Finite element model for the lip seal (from Shen [1])

For the linear FEM, the response of the structure is linearly related to the external excitation through an influence coefficient matrix. The linear FEM does not require complicated supporting techniques like the incremental scheme or the remeshing since it assumes a linear relationship between the structural deformation and the external forces, which is valid for small displacement and small strain cases. Thus the linear FEM could allow for a higher node density.

Because of the above advantages, the linear FEM prevails in the soft-EHL analysis [42-43], [51], [77-80] or the mixed-EHL analysis [49-50], [52-53]. The linear FEM also has its drawbacks: as a linear method, it could generate considerable error when used to analyze a non-linear, large structural deformation. However, the error generated by the linear FEM is tolerated in the soft-EHL or the mixed-EHL analysis because the interaction between the structure and the lubricant flow is the primary research objective.

Combined with the linear FEM, there are many contact laws that can be applied. For the point contact theory which assumes two rough surfaces are in contact through micro spherical surface asperities, there are the Hertzian Contact model [56] and the Greenwood-Tripp contact model [57]. In the practice of the EHL or the mixed-EHL analysis with the linear FEM, it is found that a very large node number on the contact interface seriously slows down the computation. To solve this problem, some researchers apply the Fast Fourier Transform (FFT) to accelerate the computation. [58] Ju and Zheng first developed a linear elastic contact model depending on the linear convolution for solution. On that basis, Ju [59] proposed using Discrete Fourier Transform (DFT) and

Fast Fourier Transform (FFT), the fast algorithm of DFT, to reduce the arithmetic operations of the linear convolution. Stanley and Kato [60] did similar research on the FFT based rough surface contact algorithm. S. Liu, Wang and G. Liu [61] went further: they modified the arrangement of the computational domain and extended the application of the FFT algorithm from the infinite domain to the finite domian. In addition they proposed using FEM to generate the influence coefficients for the contact analysis when an analytical formula is not available. In collaboration with other researchers, they then apply their contact algorithm to a series of practical problems [62-63] the three dimensional thermal mechanical asperity contact problem, elasto-plastic contact problem [64] with Chen and a three dimensional deterministic rough surface line-contact problem [65] with Ren, Zhu and Chen. Shi and Salant [49-50] introduced the FFT algorithm into the lip seal model. They employed the FFT line contact algorithm in their mixed lubrication (mixed-EHL) model and use linear FEM to generate the influence coefficient matrix needed for the linear convolution.

2.4 Development of the lip seal model

In 1980's and 90's significant advances were made in the numerical modeling of lip seal which began to explain the friction reduction and reverse pumping of the conventional lip seal. Salant and Flaherty [42-43] built an EHL model. In their dimensionless study, the seal's geometry, interference and the garter spring are properly adjusted to create a suitable sealing pressure which is supportable by a thin oil film and

does not incur solid contact. Also the sealing pressure profile across the sealing zone is consistent with the previous experimental observation that the maximum sealing pressure occurred at the location closer to the oil side as shown in Figure 2.1.1. The sealing pressure is calculated using ANSYS with a non-linear FEM approach. Both the normal and the shear deformation of the lip surface under fluid pressure and viscous fluid shear stress are calculated using the linear influence coefficients matrix generated at the deformed state also using ANSYS. Both the non-linear and the linear FEM models in are axis-symmetric as shown in Figure 2.3.1. Regular micro-undulations and micro-asperities are used as the elastomer roughness patterns. The shaft roughness is ignored. Equilibrium between the sealing pressure and the fluid pressure is achieved at each axial computation node. Flooded boundary condition is prescribed on both the oil side and the air side to facilitate the calculation of the pumping rate. The flooded boundary conditions on both sides of the sealing zone are consistent with the conditions in the oil drop test. The simulation results show that after being sheared unevenly across the sealing zone, both micro-undulations and micro-asperities show the reverse pumping tendency. Salant and Flaherty's work is valuable because it verifies (to some extent) the reverse pumping theory proposed by Kammüller [30] and Müller [31] mentioned in section 2.1. However it should be noted that their sinusoidal surface topology is quite ideal and is some distance away from a genuine random surface roughness. Hajjam and Bonneau [66] also modeled a lip seal running against sinusoidal micro-undulations, using online FEA, and came to a similar conclusions.

Stakenborg [23] found that during normal operation, instead of the oil drop test, the air side of the lip seal is not flooded. Instead, an oil meniscus close to the oil side is present. Experiments also indicated that a lip seal with a steady reverse pumping rate will ingest the oil meniscus into the sealing zone, as demonstrated in Figure 2.4.1, and reach a new equilibrium position which provides a smaller reverse pumping rate. To reflect this fact, Salant [67] modified his EHL model for the lip seal running with an ingested oil meniscus. The flooded boundary condition is prescribed on the liquid side and on the position of the ingested oil meniscus. Salant found that even though the oil meniscus is ingested into the sealing zone, the axially shortened oil film shown in Figure 2.4.1 could still provide sufficient hydrodynamic lifting force to separate the elastomer from the shaft and maintain a small reverse pumping rate.

Mixed-EHL model is a more challenging issue. The first Mixed-EHL model for the lip seal was established by Gabelli and Poll [68]. A rectangular rubber material block with the upper boundary fixed is used to simulate the elastomer of the lip seal. In this simplified model, the micro-level deformation of the material block is considered while the macro-level deformation (structural deformation) of the lip seal is ignored. Asperity contact with the shaft is considered through the Greenwood-Tripp [57] model. Two dimensional sinusoids are used as the surface roughness. The influence of the viscoelasticity is also accounted through the finite element analysis (FEA). Shi and Salant [49-50] also established mixed-EHL models for the lip seal. Shi's models were able to deal with the contact for both the deterministic roughness and the random roughness.

However, in general, Shi's model is a linear model as both the interference fit and the contact are handled with a linear approach. Fast Fourier Transform (FFT) Technique is used to accelerate the linear convolution for the contact analysis. All the above EHL or Mixed-EHL lip seal models employ a steady state version of Reynolds equation and consider the elastomer roughness only.

Shen and Salant [51-53] began to consider the influence of the shaft roughness to the lip seal. They extended the fluid dynamics sub model from the steady state version to the transient version. Besides cavitation, their fluid model contains an additional squeezing term which is capable of handling the squeeze oil film effect caused by the shaft roughness. Their studies were conducted in a step by step manner. First a pure hydrodynamic lubrication study was performed. A uniform gap is assumed between the elastomer roughness and the shaft roughness in this model. Further an EHL model is established. The EHL model is exactly the same as the one developed by Salant and Flaherty [35-36] except that the oil film thickness is time variant due to the moving of the shaft surface roughness. Final, they built a mixed-EHL model which could handle the possible contact due to a high seal load or due to the low rotating speed during the start-up and shut-down process. Their work shows that though the shaft surface is polished and the magnitude of the shaft roughness is far smaller than the elastomer roughness, the influence of the shaft roughness is still significant due to the squeeze oil film effect.

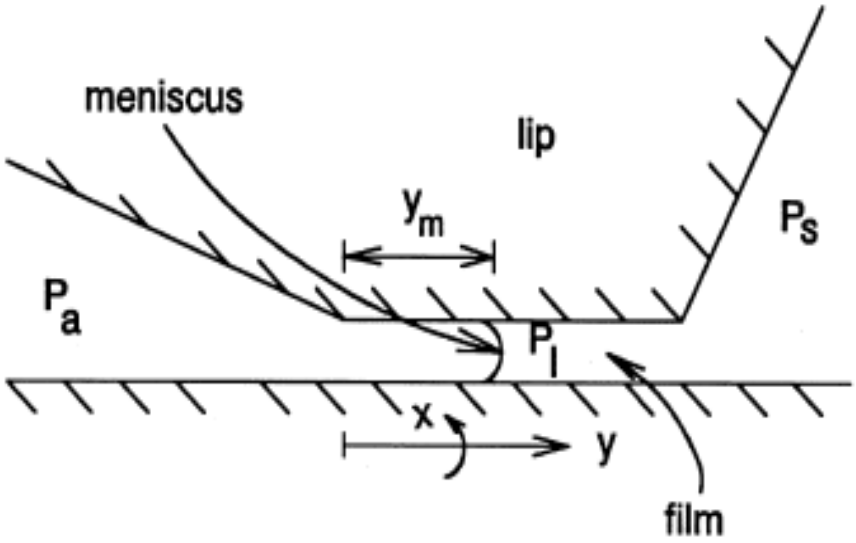

Figure 2.4.1 Ingested meniscus boundary condition for the lip seal (from [67])

2.5 Surface Texturing Techniques and Their Application to the Lip Seal

Inspired by the experimental work and the numerical models mentioned previously, significant research work has been done recently to enhance the hydrodynamic lubrication (friction reduction) effect as well as the reverse pumping effect by intentionally producing deterministic surface textures on the bearing or sealing component. Numerical modeling work for the surface textured bearing components has also been done. Etsion [4] summarized six existing surface texturing techniques respectively, Vibororolling, Undulated Surface, Reactive Ion Etching, Abrasive Jet Machining and Excimer Laser, LIGA and Lithography, and anisotropic etching. Then he primarily focused on introducing a new technique Laser Surface Texturing (LST) which could be used to produce surface textures reliably at a high efficiency (see Figure 1.3.1). He and his colleagues applied LST to various bearing parts and studied the impacts.

Etsion, Kligerman and Halperin [69] experimentally and analytically study the laser textured mechanical bearing faces. This study shows that when the hydrodynamic effect of the lubricant is suppressed by the hydrostatic effect, surface micro-structures have nearly no influence on the bearing performance; otherwise surface textures do improve the bearing performance. Ronen, Ryk, Etsion and Kligerman [70-71] laser textured the reciprocating automotive components and found a friction reduction effect during the operation. Brizmer, Kligerman, Halperin and Etsion [72-73] experimentally studied the laser textured thrust bearings and found that an extra load capacity is observed in the experiment. Ryk, Kligerman, Etsion and Shinkarenko [74-75] partially laser textured the piston rings and studied the friction reduction effect of the partial LST. They found that partial LST sometimes could achieve better hydrodynamic lubrication effect than full LST. Etsion and Sher [76] tested the performance of a partial LST piston ring in a real operating engine and found a 4% less fuel consumption without tractable change in the exhaust gas. Shinkarenko, Kligerman and Etsion [77-80] did a series of modeling work about their products processed by LST. Simulation results show that surface texturing significantly enhance the hydrodynamic lubrication as it lowered the threshold speed at which surface contact occurred.

Stephens et al. did similar surface texturing work using the modified LIGA [5] and the ultraviolet photolithography [6] techniques (see Figure 1.3.2). Surface textured thrust bearings were manufactured and tested. Siripuram and Stephens [81] numerically studied the influence of the deterministic surface asperities on the hydrodynamic lubrication.

Paige and Stephens [82] made micro surface structures on the rotating shaft and experimentally tested its impact on the performance of the radial lip seal. Warren and Stephens [83] ran a series of experiments to study the feasibility of controlling the pumping direction of the radial lip seal with different triangular surface texture patterns. Their experiments showed a satisfactory result both in the flow manipulation and the friction reduction. However, the surface texture on the shaft was so effective in pumping oil out of the sealing zone (Forward or Backward) that the sealing zone quickly became starved. Consequently both the surface texture on the shaft and the elastomer surface are subject to severe wear during the test which is discussed by Vetrivel and Warren [84] who thoroughly studied the wear condition and the geometry change of the elastomer after test. Impellizzeri [85] applied the JFO model to the study of the hydrodynamic lubrication with deterministic surface asperities. Hadinata and Stephens [86] apply the EHL model to the study of the lip seal running against surface textured shaft. The dimensionless studies of Impellizzeri and Hadinata initially show that it is possible to control the pumping direction of the lip seal through the design of the surface textures.

A similar surface texturing work for the lip seal was done by Jia, Jung, Haas and Salant [7]. In their work, the shaft surface texture pattern is a sinusoidal wave created by laser etching and the directional pumping ability of the shaft is mainly caused by the angle of the sinusoidal wave, which changes the direction of the wiping edge. They also applied the EHL model to analyze the experiment numerically. A good correspondence is found between the simulation and the experiment. The laser textured surface undulations can be

found in Figure 2.5.1

All the studies on the conventional lip seal running against smooth shafts introduced in Section 2.1-2.4 and on the surface texturing introduced in Section 2.5 reveal the feasibility of controlling the strong viscous flow by modifying the surface topology of the bearing or sealing components.

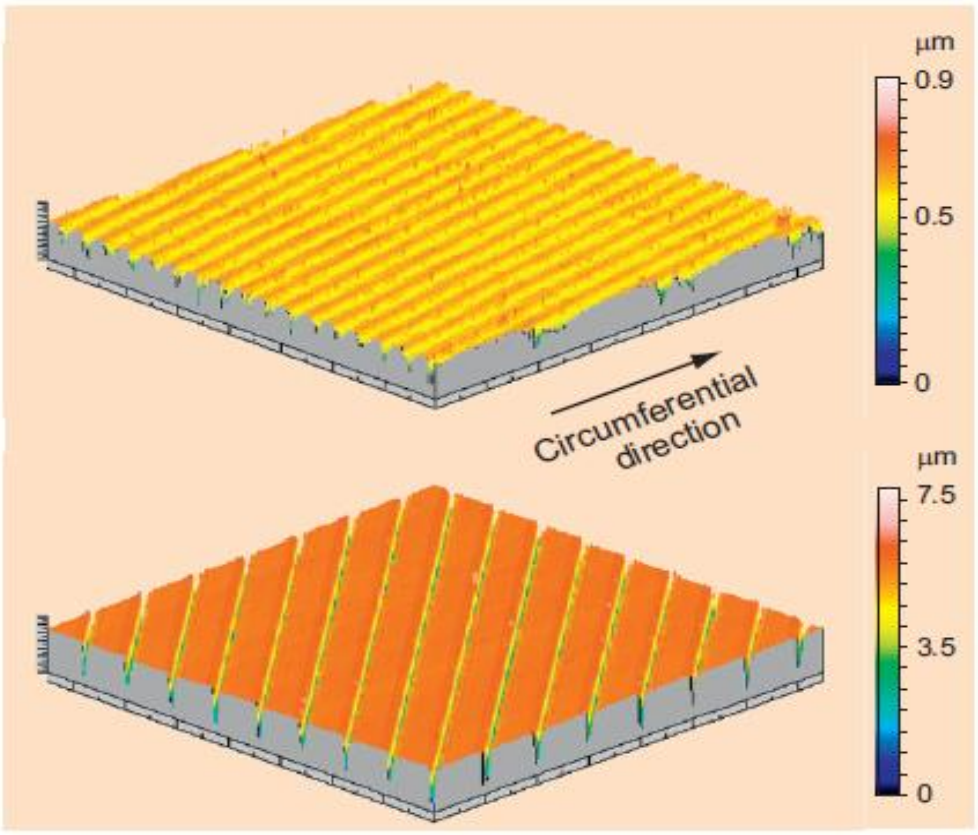

Figure 2.5.1 Laser textured surface with micro-undulation (from [7])

CHAPTER 3 — SOLID MECHANICS MODEL AND CONTACT

3.1 Fundamentals for the Finite Element Method

The finite element method (FEM) is used to determine the deformation of the elastomer as well as the shaft-elastomer contact in this study. There are many references discussing the details of FEM [87-88]. This chapter provides a brief introduction about the FEM which is used in this study. The solid mechanics problem is essentially pursuing the solution of a series of governing equations with certain boundary conditions. These governing equations are usually partial differential equations (PDEs). Classical PDEs do not always hold due to many reasons, for example the geometry of the solution domain is too complicated or the boundary conditions are complicated. Thus the weak form PDEs (integral form) are formulated for a weak solution. In the area of the solid mechanics, FEM is one kind of procedure which seeks the numerical weak solution of PDEs.

In FEM, Lagrangian mesh is commonly used. Lagrangian mesh means the nodes and the boundaries of the mesh follow the motion of the material body. This property is advantageous for the application of boundary conditions. The major disadvantage of Lagrangian mesh is that Lagrangian mesh might be seriously distorted during the solution process, which degrades the solution accuracy or even the numerical stability. The Lagrangian mesh is shown in the upper plot of Figure 3.1.1. The counterpart of the Lagrangian mesh is the Eulerian mesh whose nodes and elements are fixed in the spatial domain and do not follow the motion of the material body [87]. Since Eulerian mesh does

not trace the motion of the material particle, it does not distort during the solution procedure. Eulerian mesh is shown in the lower plot of Figure 3.1.1. Eulerian mesh is commonly used in the fluid dynamics analysis and the machining process analysis due to its mesh distortion free property.

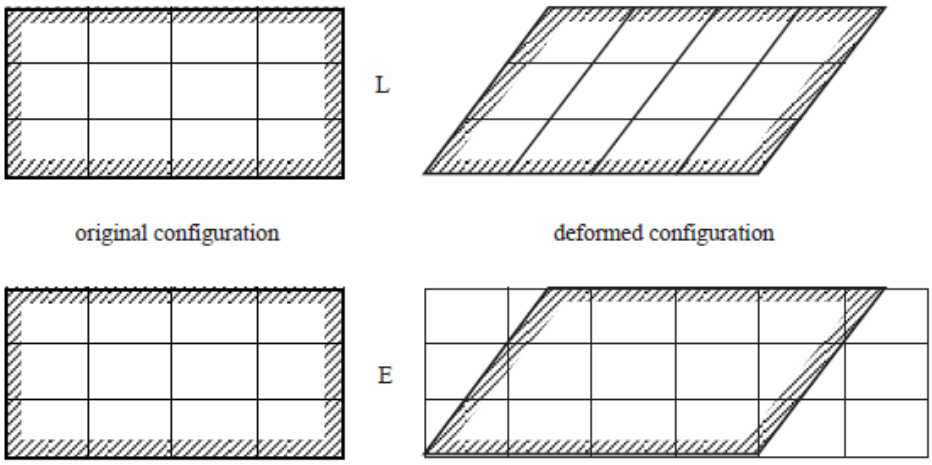

Figure 3.1.1 Lagrangian mesh and Eulerian mesh (from [87])

In FEM the geometry of the solid structure is described in two configurations the reference configuration $\mathbf{X}$ at the time t_0 and the current (deformed) configuration $\mathbf{x}$ at the time $t_0 + \Delta t$, respectively, as shown in Figure 3.1.2. (Bold letters represent the vector or second order tensor). The deformed configuration is a function of the reference configuration as shown in equation $(3.1.1)$. It should be noted that the reference configuration $\mathbf{X}$ is just the configuration of the structure at the analysis time t_0 and is not necessarily to be the un-deformed configuration. The displacement, velocity and acceleration of the structure are expressed in equation $(3.1.2) - (3.1.4)$

$$\mathbf{x} = \Phi(\mathbf{X}, t) \text{ and } \mathbf{X} = \Phi^{-1}(\mathbf{x}, t) \tag{3.1.1}$$

$$\mathbf{u}(\mathbf{X}, t) = \mathbf{x} - \mathbf{X} = \Phi(\mathbf{X}, t) - \mathbf{X} \tag{3.1.2}$$

$$\mathbf{v}(\mathbf{X}, t) = \frac{D\mathbf{u}}{Dt} = \frac{d\mathbf{u}}{dt} \tag{3.1.3}$$

$$\mathbf{a}(\mathbf{X}, t) = \frac{D\mathbf{v}}{Dt} = \frac{D^2\mathbf{u}}{Dt^2} = \frac{d^2\mathbf{u}}{dt^2} \tag{3.1.4}$$

$D()/Dt$ denotes the material time derivative [87]. Since in equation $(3.1.2) - (3.1.4)$ all the dependent variables are expressed in terms of the reference configuration $\mathbf{X}$, whose nodes coincide with the material nodes at time t_0, the material time derivative simply reduces to the ordinary derivative with respect to t as $d()/dt$, The arbitrary incremental variable doesn't necessarily need to be the physical time unless time dependent effects like the inertia (acceleration) or the visco-elasticity is considered. The strain of the material body as well as the stress inside the material body are regarded as dependent variables of $\mathbf{X}$ via the deformation gradient $\mathbf{F}$:

$$\mathbf{F} = \frac{\partial \mathbf{x}}{\partial \mathbf{X}} = \frac{\partial \mathbf{u}}{\partial \mathbf{X}} + \mathbf{I} \tag{3.1.5}$$

$\mathbf{F}$ is the Jacobian matrix linking the deformed configuration $\mathbf{x}$ at the time $t_0 + \Delta t$ and

the un-deformed configuration $\mathbf{X}$ at the time t_0. The Jacobian determinant is:

$$J = \det(\mathbf{F}) \tag{3.1.6}$$

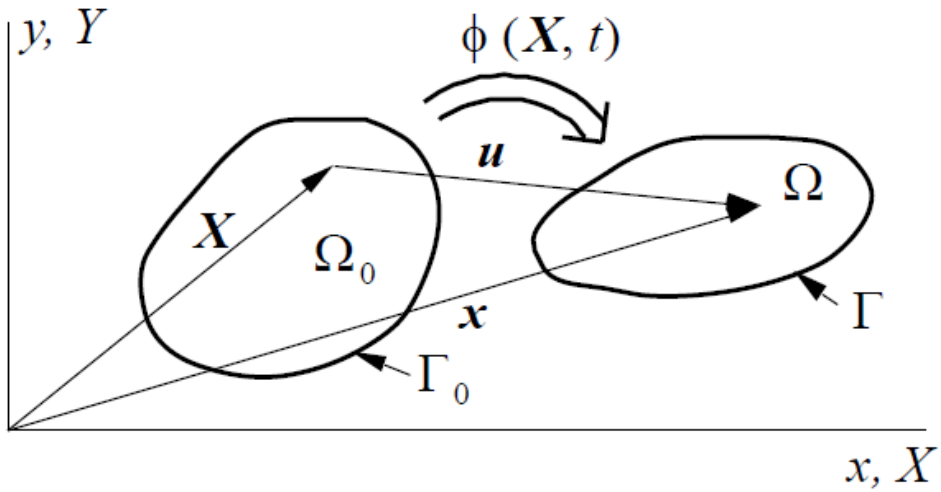

Figure 3.1.2 Spatial description of the FEM (from [87])

3.2 Governing Equations in Total Lagrangian Formulation

Though most FEMs employ a Lagrangian mesh, they can be further distinguished as the total Lagrangian formulation and the updated Lagrangian formulation. The total Lagrangian formulation expresses all the dependent variables in terms of the reference configuration $\mathbf{X}$ as described in section 3.1. While the updated Lagrangian formulation expresses all the dependent variables in terms of the current (deformed) configuration $\mathbf{x}$. The deformed configuration $\mathbf{x}$ does not coincide with the material nodes at time t_0 but coincides with the material nodes at time $t_0 + \Delta t$. Thus $\mathbf{x}$ is regarded as the function of t and the chain rule is needed when taking the material time derivative in the updated

Lagrangian formulation. It can be proved that there is only a formal difference between the total Lagrangian formulation and the updated Lagrangian formulation. These two formulations are essentially equivalent to each other. The detailed proof is out of the scope of this study and can be found in reference [87]. In this chapter the governing equations for the FEM are presented in the total Lagrangian form to briefly demonstrate the solid mechanics approach.

Mass conservation:

$$\int_{\Omega_0} \rho_0 d\Omega_0 = \int_{\Omega} \rho \, d\Omega \Rightarrow \int_{\Omega_0} (\rho_0 - \rho J) d\Omega_0 = 0 \qquad (3.2.1)$$

In equation (3.2.1) Ω_0 is the original material domain and Ω is the current material domain. ρ_0 is the material density in the reference configuration **X**. ρ is the material density at the current configuration **x**. Since equation (3.2.1) needs to be satisfied on any arbitrary small material domain, it is equivalent to:

$$\rho_0 - \rho J = 0 \Rightarrow \rho_0 = \rho J \qquad (3.2.2)$$

The algebraic form of the mass conservation equation (3.2.2) is only available for the Lagrangian mesh in which the mesh follows the deformation of the material body and the

Jacobian matrix between the reference configuration $\mathbf{X}$ at t_0 and the deformed configuration $\mathbf{x}$ at $t_0 + \Delta t$ can be well defined. If the Eulerian mesh is used as in the fluid dynamics, the mass conservation law will be in the form of the partial differential equation known as the continuity equation.

Conservation of linear momentum: (Newton's second law):

$$\frac{D}{Dt}\int_{\Omega_0} \rho_0 \, \mathbf{v}(\mathbf{X}, t) d\Omega_0 = \int_{\Omega_0} \rho_0 \, \mathbf{b}(\mathbf{X}, t) d\Omega_0 + \int_{\Gamma_0} \mathbf{T}_{\Gamma_0}(\mathbf{X}, t) \, d\Gamma_0 \qquad (3.2.3)$$

In equation (3.2.3) $\mathbf{b}(\mathbf{X}, t)$ is the body force vector. $\mathbf{T}_{\Gamma_0}(\mathbf{X}, t)$ is the surface traction vector on the boundary Γ_0 of the material body. LHS term in equation (3.2.3) represents the rate of change of momentum in the material body. The material time derivative can be moved into the integral since the reference configuration $\mathbf{X}$ coincides with the material body and is not time dependent. If Eulerian mesh is employed, Reynolds transport theorem [88] will be needed to move the material time derivative into the integral. The RHS terms represent the total force applied on the material body including the body force (first term) and the surface traction (second term). Applying Gauss's theorem [88] to the second RHS term yields equation (3.2.4)

$$\int_{\Omega_0} \rho_0 \frac{\partial \mathbf{v}}{\partial t} d\Omega_0 = \int_{\Omega_0} \rho_0 \mathbf{b} d\Omega_0 + \int_{\Gamma_0} \mathbf{n}_{\Gamma_0} \cdot \boldsymbol{\sigma}_{\Gamma_0} d\Gamma_0$$

$$\xrightarrow{\text{Gauss's theorem to the second term on the RHS}}$$

$$\int_{\Omega_0} \rho_0 \frac{\partial \mathbf{v}}{\partial t} d\Omega_0 = \int_{\Omega_0} \rho_0 \mathbf{b} d\Omega_0 + \int_{\Omega_0} \nabla_0 \cdot \boldsymbol{\sigma} \, d\Omega_0 \tag{3.2.4}$$

In equation (3.2.4) $\boldsymbol{\sigma}_{\Gamma_0}$ is the surface stress on the boundary surface Γ_0 of the material body while $\mathbf{n}_{\Gamma_0}$ is the surface normal vector of the boundary surface Γ_0. $\boldsymbol{\sigma}$ is the stress inside the body which is also regarded as a dependent variable of $\mathbf{X}$ via the constitutive law of equation (3.2.8). ∇_0 is the divergence operator with respect to the reference configuration $\mathbf{X}$. Equation (3.2.4) needs to be satisfied on any arbitrary material domain, thus it is equivalent to equation (3.2.5)

$$\rho_0 \frac{\partial \mathbf{v}}{\partial t} = \rho_0 \mathbf{b} + \nabla_0 \cdot \boldsymbol{\sigma} \tag{3.2.5}$$

The LHS term in equation (3.2.5) represents the momentum changing rate per unit material volume while the RHS terms represent the internal body force per unit volume and the divergence of the internal stress. In many finite element analyses static equilibriums of the structures are pursued and the external loads are applied slowly onto the structure thus the inertial effect can be neglected. Thus equation (3.2.5) can be modified to yield the equilibrium equation (3.2.6) simply by dropping the LHS term of equation (3.2.5)

$$\rho_0 \mathbf{b} + \nabla_0 \cdot \boldsymbol{\sigma} = \mathbf{0} \tag{3.2.6}$$

Conservation of angular momentum:

$$J^{-1}\mathbf{F} \cdot \boldsymbol{\sigma} = (J^{-1}\mathbf{F} \cdot \boldsymbol{\sigma})^{\mathbf{T}} \Rightarrow \mathbf{F} \cdot \boldsymbol{\sigma} = \boldsymbol{\sigma}^{\mathbf{T}} \cdot \mathbf{F}^{\mathbf{T}} \tag{3.2.7}$$

Constitutive law:

$$\boldsymbol{\sigma}(\mathbf{X}, t) = \boldsymbol{\sigma}\big(\mathbf{F}(\mathbf{X}, \bar{t}), \dot{\mathbf{F}}(\mathbf{X}, \bar{t}), \cdots, \cdots\big) \;\; t_0 \leq \bar{t} \leq t \tag{3.2.8}$$

Equation (3.2.8) shows the internal body stress is a function of the deformation gradient and the history of the deformation gradient. For elastic material the history dependent property is eliminated. Also note that since the deformation gradient $\mathbf{F}$ is a function of the first spatial derivative of the displacement $\mathbf{u}$ as shown in equation (3.1.5), $\boldsymbol{\sigma}(\mathbf{X}, t)$ is actually a function of the first spatial derivative of the displacement $\mathbf{u}$ via the constitutive law.

Boundary conditions:

$$\mathbf{u} = \bar{\mathbf{u}} \text{ on } \Gamma_{\bar{\mathbf{u}}} \tag{3.2.9}$$

$$\mathbf{n}_{\Gamma_{\bar{\mathbf{T}}}} \cdot \boldsymbol{\sigma}_{\Gamma_{\bar{\mathbf{T}}}} = \bar{\mathbf{T}} \text{ on } \Gamma_{\bar{\mathbf{T}}} \tag{3.2.10}$$

Equations $(3.2.9) - (3.2.10)$ represent the displacement boundary condition and the surface traction boundary condition respectively. $\Gamma_{\bar{\mathbf{u}}}$ is the boundary for the prescribed displacement while $\Gamma_{\bar{\mathbf{T}}}$ is the boundary for the prescribed surface traction. $\Gamma_{\bar{\mathbf{u}}} + \Gamma_{\bar{\mathbf{T}}} = \Gamma_0$

Initial conditions:

$$\boldsymbol{\sigma}(\mathbf{X}, 0) = \boldsymbol{\sigma}_{\mathbf{0}}(\mathbf{X}) \tag{3.2.11}$$

$$\dot{\mathbf{u}}(\mathbf{X}, 0) = \dot{\mathbf{u}}_{\mathbf{0}}(\mathbf{X}) \tag{3.2.12}$$

Smoothness requirement:

For the momentum equation $(3.2.5)$ or the equilibrium equation $(3.2.6)$ to hold in the classical sense, the dependent variable $\mathbf{u}(\mathbf{X}, \mathrm{t})$ should be C^2.(C^{n} means the nth order derivative of the variable is continuous) Note that $\boldsymbol{\sigma}(\mathbf{X}, \mathrm{t})$ is assumed to be a

smooth function of the first spatial derivative of $\mathbf{u}(\mathbf{X},t)$ via the constitutive law equation (3.2.8). Also note that the first spatial derivative of $\boldsymbol{\sigma}(\mathbf{X},t)$ presents in the equation (3.2.5) and equation (3.2.6). Thus for the first spatial derivative of $\boldsymbol{\sigma}(\mathbf{X},t)$ to be continuous in space, $\mathbf{u}(\mathbf{X},t)$ must be C^2 in space. The above requirement can be overly restrictive and sometimes can hardly be satisfied in the structural analysis, which motivates the developing of the weak form momentum equation or equilibrium equation.

Weak form momentum equation for the total Lagrangian formulation:

The weak form momentum equation for the total Lagrangian formulation is obtained by multiplying the momentum equation (3.2.5) by the test function $\delta\mathbf{u}$ and integrating over the material domain. The weak form momentum equation for the total Lagrangian formulation is also known as the principle of virtual work which is actually a variation principle.

$$\int_{\Omega_0} \delta\mathbf{u} \cdot \left(\nabla_0 \cdot \boldsymbol{\sigma} + \rho_0 \mathbf{b} - \rho_0 \ddot{\mathbf{u}}\right) d\Omega_0 = 0 \qquad (3.2.13)$$

In equation (3.2.13) the requirement for the smoothness of the displacement function $\mathbf{u}$ is relaxed to C^1 and limited bounded discontinuous points are permitted for $\nabla_0 \cdot \boldsymbol{\sigma}$ due to the integral. A C^1 requirement for the displacement field $\mathbf{u}$ is still somewhat restrictive for the FEM. Note that the first term on the LHS of equation (3.2.13) could

be further modified as shown in equation (3.2.14)

$$\int_{\Omega_0} \delta\mathbf{u} \cdot (\nabla_0 \cdot \boldsymbol{\sigma})\, d\Omega_0 = \int_{\Omega_0} \nabla_0 \cdot (\delta\mathbf{u} \cdot \boldsymbol{\sigma})\, d\Omega_0 - \int_{\Omega_0} \nabla_0(\delta\mathbf{u}) : \boldsymbol{\sigma} d\Omega_0 \qquad (3.2.14)$$

$:$ is the second order contraction operator for the second order tensor. Further note that in equation (3.2.14) the domain integral of the first term on the RHS can be expressed as a boundary integral by applying Gauss's theorem:

$$\int_{\Omega_0} \nabla_0 \cdot (\delta\mathbf{u} \cdot \boldsymbol{\sigma})\, d\Omega_0 = \int_{\Gamma_0} \delta\mathbf{u} \cdot \left(\mathbf{n}_{\Gamma_0} \cdot \boldsymbol{\sigma}_{\Gamma_0}\right) d\Gamma_0 + \int_{\Gamma_{c^{-1}}} \delta\mathbf{u} \cdot \left[\!\left[\mathbf{n}_{\Gamma_{c^{-1}}} \cdot \boldsymbol{\sigma}_{\Gamma_{c^{-1}}}\right]\!\right] d\Gamma_{c^{-1}} \qquad (3.2.15)$$

In equation (3.2.15) it is assumed that the displacement field is C^1. The expression $\nabla_0 \cdot (\delta\mathbf{u} \cdot \boldsymbol{\sigma})$ which is a function of the second spatial derivative of $\mathbf{u}$ has limited bounded discontinuous internal boundaries $\Gamma_{c^{-1}}$. The term $\left[\!\left[\mathbf{n}_{\Gamma_{c^{-1}}} \cdot \boldsymbol{\sigma}_{\Gamma_{c^{-1}}}\right]\!\right]$ is the jump of the traction on the internal discontinuous boundaries of $\nabla_0 \cdot (\delta\mathbf{u} \cdot \boldsymbol{\sigma})$. If the internal continuity equation (3.2.16) is satisfied, then the last term in equation (3.2.15) vanishes resulting in equation (3.2.17)

$$\left[\!\left[\mathbf{n}_{\Gamma_{c^{-1}}} \cdot \boldsymbol{\sigma}_{\Gamma_{c^{-1}}}\right]\!\right] = 0 \qquad (3.2.16)$$

$$\int_{\Omega_0} \nabla_0 \cdot (\delta\mathbf{u} \cdot \boldsymbol{\sigma})\, d\Omega_0 = \int_{\Gamma_0} \delta\mathbf{u} \cdot \left(\mathbf{n}_{\Gamma_0} \cdot \boldsymbol{\sigma}_{\Gamma_0}\right) d\Gamma_0 \qquad (3.2.17)$$

In equation (3.2.17) the boundary is defined as $\Gamma_0 = \Gamma_{\bar{\mathbf{u}}} + \Gamma_{\bar{\mathbf{T}}}$. Note that on the prescribed displacement boundary $\Gamma_{\bar{\mathbf{u}}}$: $\delta\mathbf{u} = 0$. Thus equation (3.2.17) further reduces to:

$$\int_{\Omega_0} \nabla_0 \cdot (\delta\mathbf{u} \cdot \boldsymbol{\sigma})\, d\Omega_0 = \int_{\Gamma_{\bar{\mathbf{T}}}} \delta\mathbf{u} \cdot \left(\mathbf{n}_{\Gamma_{\bar{\mathbf{T}}}} \cdot \boldsymbol{\sigma}_{\Gamma_{\bar{\mathbf{T}}}}\right) d\Gamma_{\bar{\mathbf{T}}} = \int_{\Gamma_{\bar{\mathbf{T}}}} \delta\mathbf{u} \cdot \bar{\mathbf{T}}\, d\Gamma_{\bar{\mathbf{T}}} \qquad (3.2.18)$$

Plugging equation (3.2.18) into equation (3.2.14) and then plugging equation (3.2.14) into equation (3.2.13) obtained:

$$\int_{\Omega_0} \left[\nabla_0(\delta\mathbf{u}) \dddot{:} \boldsymbol{\sigma} + \rho_0 \delta\mathbf{u} \cdot \ddot{\mathbf{u}} - \rho_0 \delta\mathbf{u} \cdot \mathbf{b}\right] d\Omega_0 - \int_{\Gamma_{\bar{\mathbf{T}}}} \delta\mathbf{u} \cdot \bar{\mathbf{T}}\, d\Gamma_{\bar{\mathbf{T}}} = 0 \qquad (3.2.19)$$

Equation (3.2.19) is the weak form momentum equation. It can be shown that the requirement for the dependent variable $\mathbf{u}$ in equation (3.2.19) is only C^0 and equation (3.2.19) is equivalent to the weak form equation (3.2.13) as long as the internal continuity equation (3.2.16) is satisfied. C^0 requirement for $\mathbf{u}$ simply means the displacement function in FEM must be continuous, which is also known as the compatibility requirement in FEM. Rearranging the order of equation (3.2.19) yields

equation (3.2.20).

$$\int_{\Omega_0} \left[\rho_0 \delta\mathbf{u} \cdot \ddot{\mathbf{u}} + \nabla_0(\delta\mathbf{u}) \dddot{:} \boldsymbol{\sigma}\right] d\Omega_0 = \int_{\Omega_0} \rho_0 \delta\mathbf{u} \cdot \mathbf{b} d\Omega_0 + \int_{\Gamma_{\bar{\mathbf{T}}}} \delta\mathbf{u} \cdot \bar{\mathbf{T}}\, d\Gamma_{\bar{\mathbf{T}}} \qquad (3.2.20)$$

In equation (3.2.20), the LHS terms represents the virtual energy of the material body due to the inertia force and the internal stress while the RHS terms are the forcing functions representing the virtual work done by the body force and the surface traction force respectively. If the inertia effect can be neglected, equation (3.2.20) can be further reduced to the weak form equilibrium equation:

$$\int_{\Omega_0} \nabla_0(\delta\mathbf{u}) \dddot{:} \boldsymbol{\sigma} d\Omega_0 = \int_{\Omega_0} \rho_0 \delta\mathbf{u} \cdot \mathbf{b} d\Omega_0 + \int_{\Gamma_{\bar{\mathbf{T}}}} \delta\mathbf{u} \cdot \bar{\mathbf{T}}\, d\Gamma_{\bar{\mathbf{T}}} \qquad (3.2.21)$$

After the spatial discretization and the assembly of the global matrices, equation (3.2.20) becomes the matrix equation (3.2.22) and equation (3.2.21) becomes the matrix equation (3.2.23). Most FEM solve for the displacement field **u**. Sometimes two fields or a multiple field formulation is used in FEM, but not introduced here.

$$[M][\ddot{u}(\mathbf{X}, t)] + [K][u(\mathbf{X}, t)] = [f_{ext}(\mathbf{X}, t)] \qquad (3.2.22)$$

$$[K][u(\mathbf{X}, t)] = [f_{ext}(\mathbf{X}, t)] \qquad (3.2.23)$$

3.3 Nonlinear FEM and Contact

Nonlinear FEM can be used to calculate the sealing pressure distribution and the sealing zone width of the lip seal**.** The nonlinearity of the FEM comes from 1) the geometric nonlinearity such as the large deformation of the structure; 2) the nonlinear material property like hyper-elasticity; and 3) the contact between two bodies which results in a time dependent contact interface and the corresponding normal contact force. In section 3.2, it has been shown that usually two types of boundary conditions are given in FEM: respectively the prescribed displacement and the prescribed surface traction. The contact problem poses some difficulty on the surface traction boundary condition because the surface traction on the contact interface will change as the contact boundary changes. At each time point t, the contact boundary (in touch or separation) must be identified and the normal surface traction due to the contact must be calculated.

In this study the penalty method is selected in the commercial software to deal with the possible solid contact between the two material bodies, for example between the lip seal and the shaft. The penalty method permits a small interpenetration between the two contact bodies but a tiny interpenetration will incur a very large penalty reaction force due to a large penalty stiffness prescribed in the algorithm. The penalty reaction force prevents the further interpenetration. The penalty normal surface traction is a function of the interpenetration and the rate of the interpenetration. Figure 3.3.1 shows the contact status for the contact analysis of the lip seal at an arbitrary time t. Note that the contact boundary shown in Figure 3.3.1 changes as the shaft moves upward. To deal with the

nonlinearity in FEM, the total analysis is subdivided into many small incremental steps for equation (3.2.21) (in this study a static equilibrium is pursued and the inertia effect is ignored). In each step, the governing equation is linearized. Newton-Raphson iteration is used to approach the equilibrium solution of the linearized governing equation at time (or increment) $t_0 + n \cdot \Delta t$ starting from the initial value at time (or increment) $t_0 + (n-1) \cdot \Delta t$. The result of the nonlinear analysis for the lip seal contact is shown in Figure 3.3.2. In the contact analysis, axis-symmetrical element is used and a 2-D analysis is employed to make the computation time affordable.

Figure 3.3.3 shows the local sealing pressure distribution over the sealing zone. The sealing pressure distribution obtained from the nonlinear FEM matches the conventional theory that the maximum sealing pressure occurs at the location closer to the oil side than to the air side. The surface roughness on both the elastomer and the shaft are ignored in the nonlinear FEM because a high resolution representation of the random or the deterministic surface roughness requires a 3-D model and a very large grid density which is computational prohibitive in the nonlinear FEM. The axis-symmetrical FE model can be coupled with the fluid calculation in an iterative process. The fluid pressure must first overcome the sealing pressure shown in Figure 3.3.3 to further displace the elastomer surface through the linear influence coefficient matrix generated at the deformed state.

$$\Delta \mathbf{u} = \mathbf{B}_{\text{infl}} \left(\mathbf{F}_{\text{fluid}} - \mathbf{F}_{\text{sealing}} \right) \tag{3.3.1}$$

In equation (3.3.1) $\Delta\mathbf{u}$ is the further deformation of the elastomer from the deformed equilibrium position obtained from the nonlinear FE analysis. $\mathbf{F}_{\text{fluid}}$ is the fluid supporting force vector and $\mathbf{F}_{\text{sealing}}$ is the sealing force vector. The pressure is converted into the nodal force with the Gaussian integration. $\mathbf{B}_{\text{infl}}$ is the influence coefficient matrix which is essentially the partial flexibility matrix described in equation (3.4.5) later**.** Note that in equation (3.3.1), the flexibility matrix $\mathbf{B}_{\text{infl}}$ is generated at the deformed state of the lip seal which is shown in Figure 3.3.3. While in equation (3.4.5) the flexibility matrix is generated at the un-deformed state of the lip seal as shown in Figure 3.4.1.

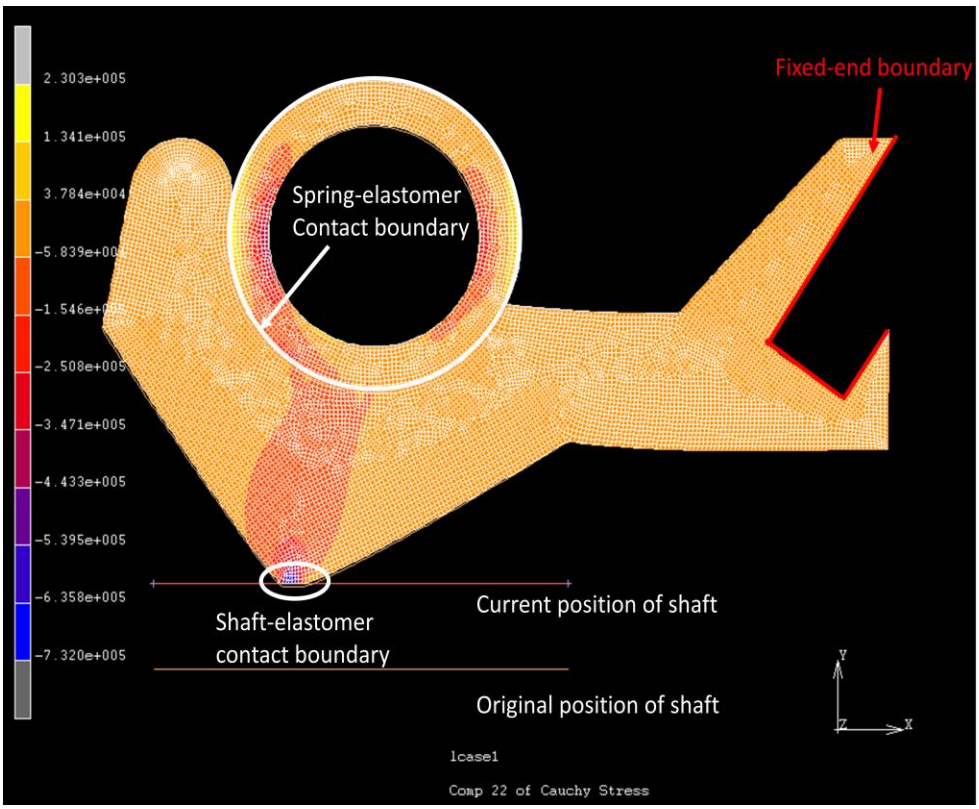

Figure 3.3.1 Contact boundaries for an arbitrary incremental step

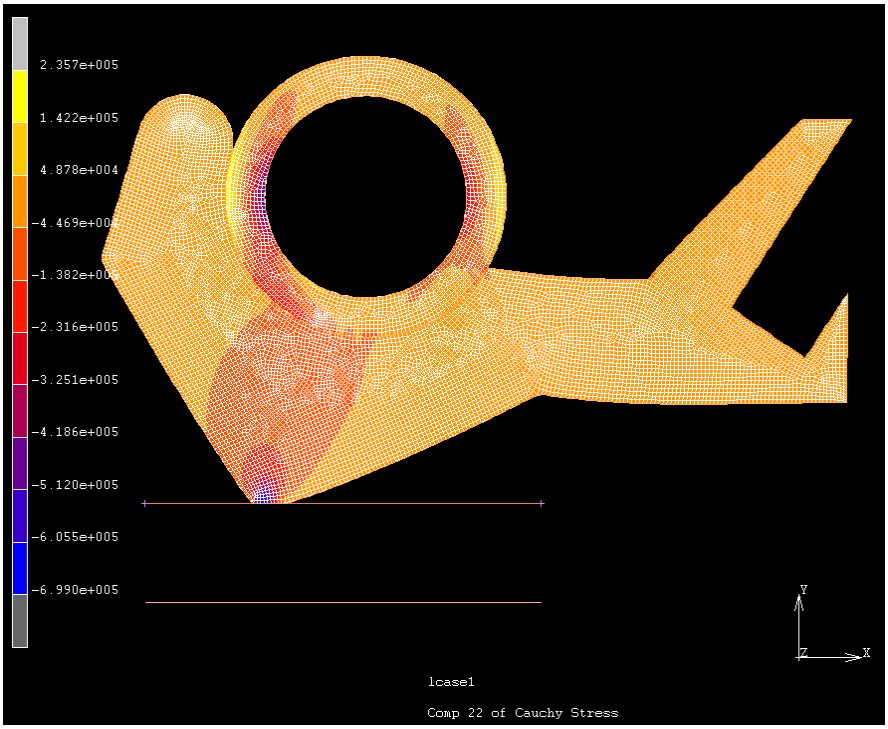

Figure 3.3.2 Nonlinear FEM result of the contact analysis for the lip seal

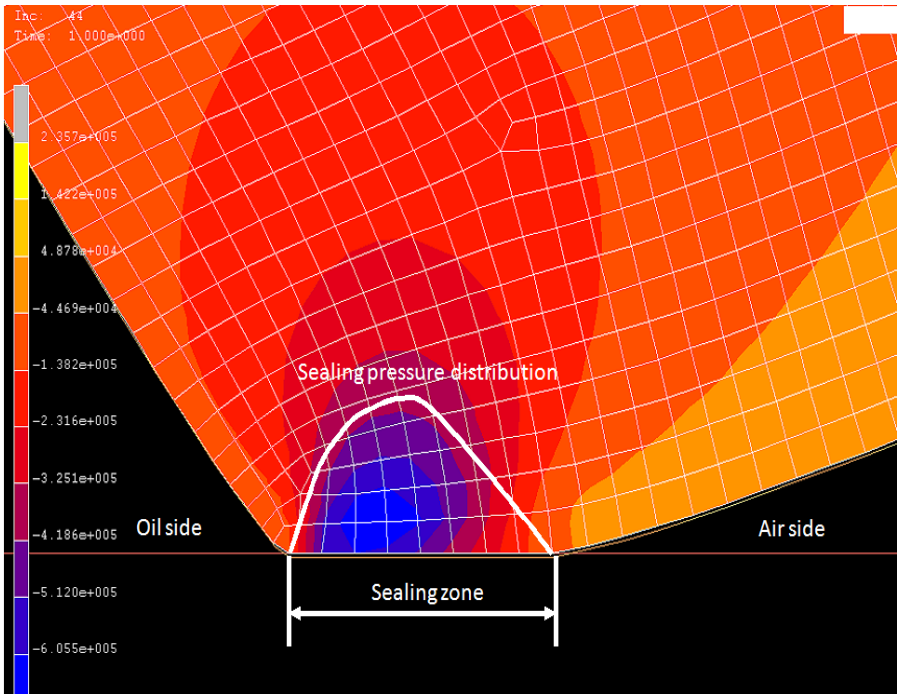

Figure 3.3.3 Sealing pressure distribution across the sealing zone

3.4 Linear FEM Considering the Surface Roughness

It is seen in section 3.3 that the surface roughness is ignored in the nonlinear FE analysis. It should be noted that though the surface roughness does not influence the general trend of the axial sealing pressure distribution as shown in Figure 3.3.3, it does influence the local sealing pressure distribution closely around the roughness. This is important in the lubrication problem since it will be shown in Chapter 4 and Chapter 5 that the Reynolds equation is quite sensitive to the local oil film variation which is directly related to the equilibrium between the local sealing pressure and the oil film pressure. In this study a linear FE analysis is used to recover the sealing pressure distribution perturbed by the surface roughness. Unlike the nonlinear FEM which has many small incremental steps and reforms the stiffness matrix at each incremental step to reflect a changing displacement-force relationship, linear FEM has only a single analysis step and the nodal displacement is linearly related to the applied nodal force through a non-modified stiffness matrix $[K]$ as described in equation $(3.2.23)$. Linear FEM is more straight forward to implement, however, it could generate more error when it is used to analyze large deformation of structures in which the displacement-force relationship changes as the structure deviates from the reference configuration X at which the stiffness matrix $[K]$ is generated. The possible error caused by the linear FEM is tolerated in this study to recover the contact details between the rough surfaces.

The first step to implement the linear FEM to the lip seal is to generate the influence coefficient matrices for the tip of the elastomer as shown in Figure 3.4.1. In the linear

FEM a stiffness matrix [K] for the entire elastomer is formed at the beginning of the analysis just after the boundary condition is applied. The stiffness matrix [K] contains all the nodes shown in Figure 3.4.1 except those nodes with zero displacement boundary conditions (Rigid frame boundary). Since the external nodal force is applied only to the nodes falling on the contact surface of the elastomer as shown in Figure 3.4.1 (mesh refined area), the stiffness matrix can be partitioned as:

$$\begin{bmatrix} K_{11} & K_{12} \\ K_{21} & K_{22} \end{bmatrix} \begin{bmatrix} u_s \\ u_{ns} \end{bmatrix} = \begin{bmatrix} F_s \\ F_{ns} \end{bmatrix} \tag{3.4.1}$$

Where the quantity with the subscript $'s'$ belongs to the nodes attached on the potential contact surface. The quantity with the subscript $'ns'$ belongs to the nodes that are not potentially involved in contact. Since the non-contact force vector F_{ns} equals to zero, equation (3.4.1) is equivalent to equation (3.4.2) and (3.4.3):

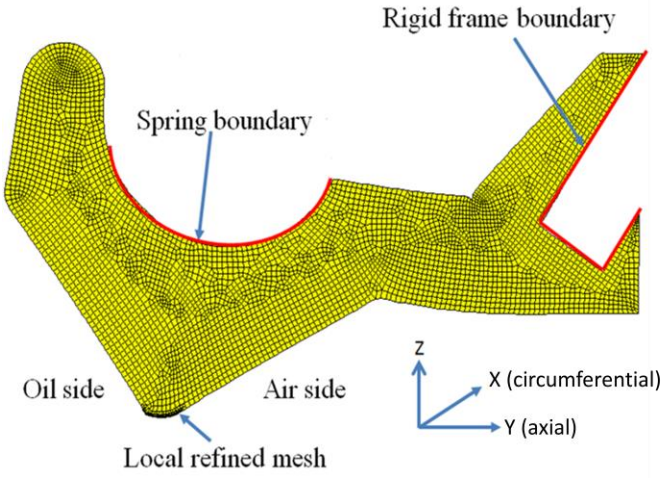

Figure 3.4.1 Linear FE model of the elastomer

$$[K_{11}][u_s] + [K_{12}][u_{ns}] = [F_s] \tag{3.4.2}$$

$$[u_{ns}] = -[K_{22}]^{-1}\,[K_{21}][u_s] \tag{3.4.3}$$

Where $[K_{11}]$ and $[K_{22}]$ are square and invertible according to the linear elastic FE theory. Plugging equation (3.4.2) into equation (3.4.3) results in:

$$\{[K_{11}] - [K_{12}][K_{22}]^{-1}\,[K_{21}]\}[u_s] = [F_s] \tag{3.4.4}$$

The solution for the linear elastic finite element problem is unique, thus $\{[K_{11}] - [K_{12}][K_{22}]^{-1}\,[K_{21}]\}$ is also invertible and its inverse $[B_{11}]$ in equation (3.4.5) is the reduced flexibility matrix in the FEM. In the literature, $[B_{11}]$ is usually called the influence coefficient matrix. It represents the influence the external nodal forces have on the nodal displacements of the nodes in the contact area. Sometimes the partial stiffness matrix $\{[K_{11}] - [K_{12}][K_{22}]^{-1}\,[K_{21}]\}$ is also called the influence coefficient matrix in the literature, which is a little confusing. One must be careful about the difference between the partial flexibility matrix and the partial stiffness matrix.

$$[B_{11}] = \{[K_{11}] - [K_{12}][K_{22}]^{-1}\,[K_{21}]\}^{-1} \tag{3.4.5}$$

$$[u_s] = [B_{11}][F_s] \tag{3.4.6}$$

Given either $[u_s]$ or $[F_s]$, the other counterpart can be determined either with equation (3.4.4) or with equation (3.4.6). The extraction of the partial flexibility matrix $[B_{11}]$ shown in equation (3.4.6) is generated by the excitation-response method. This is accomplished by applying a unit nodal force on each node in the sealing zone and recording the response of all the nodes within the sealing zone. The partial stiffness matrix $[K_{11}] - [K_{12}][K_{22}]^{-1}[K_{21}]$ is obtained by the mathematical inversion of the partial flexibility matrix $[B_{11}]$. After the above preparation, the contact analysis of the lip seal can be conducted.

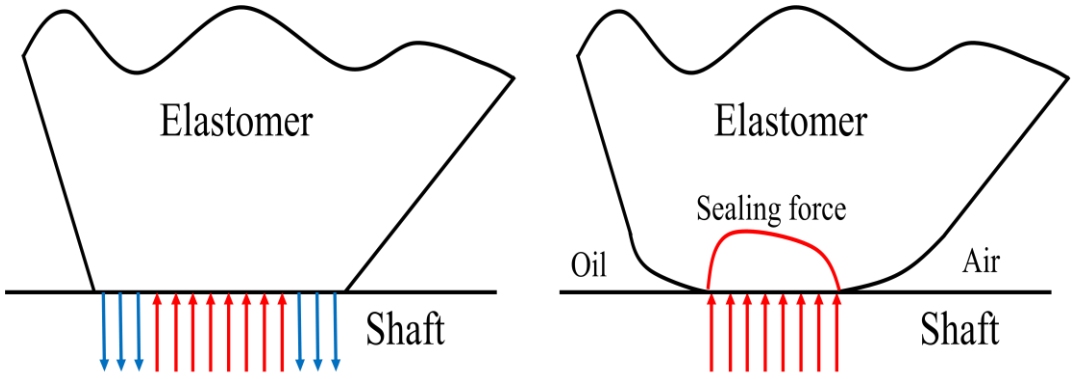

(a) (b)

Figure 3.4.2 Demonstration of the linear contact analysis for the lip seal

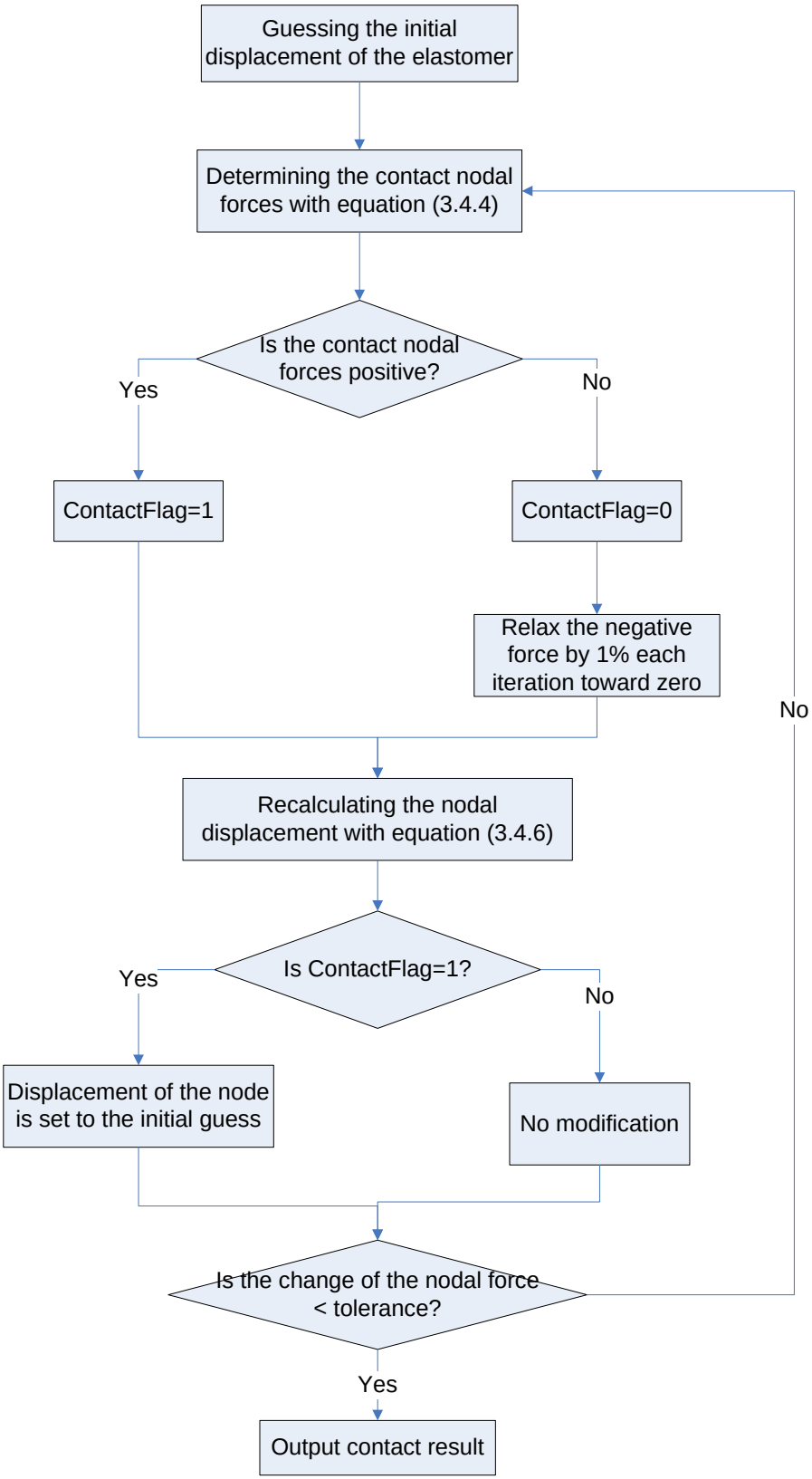

Figure 3.4.3 Algorithm flow chart for the linear contact analysis for the lip seal

It is assumed that the shaft is moving radially onto the seal and the seal is completely flattened by the shaft as shown in Figure 3.4.2 (a). The initial displacement of the elastomer $\left[u_s^{int}\right]$ is inserted into equation (3.4.4) to obtain the corresponding external nodal force needed. It is found that in some areas the nodal force is negative. Since the negative contact force does not exist physically, the negative contact force is gradually relaxed to zero as shown in Figure 3.4.2 (b). The details of the algorithm used in the contact analysis can be found in Figure 3.4.3. The contact force is essentially the external nodal force applied on the contact interface. Under the assumption that there is only solid contact force on the interface, the physically admissible external nodal force at any node should be larger than zero. But zero is not the only criterion for judging the physical admissibility of the external force when forces other than the solid contact force present on the contact interface.

The simulation for the lip seal fitted to the smooth shaft and to the shaft with staggered triangular surface structures is conducted. Figure 3.4.4 shows the final geometry of the elastomer in contact with the triangular surface cavity. Figure 3.4.5 shows the 2-D axial distribution of the sealing force for the contact between the lip seal and a smooth shaft. This sealing force distribution is similar to the results shown in Figure 3.3.3 as the maximum sealing force occurs at the spot closer to the oil side than to the air side due to the asymmetrical geometry of the elastomer apex. Figure 3.4.6 shows the 3-D sealing force distribution for the contact between the lip seal and the staggered triangular cavities. Figure 3.4.7 and Figure 3.4.8 show the different contact status for the

staggered triangular cavities and the staggered triangular asperities. The Young's modulus of the elastomer is 1.5 MPa and the Poisson's ratio is 0.49 in the simulation. The computational domain is 300 μm in the circumferential direction and 570 μm in the axial direction. There are 259 node in the axial direction and 128 nodes in the circumferential direction.

The above contact analysis result can be coupled with the fluid calculation simply by setting the oil film supporting force as the physically admissible external force. During the iteration shown in Figure 3.4.3, any external nodal force lower than the oil film supporting force on that node indicates a local separation of the contact and is relaxed to the oil film supporting force on the node. In the contrary, an external nodal force larger than the oil film supporting force means the oil film supporting force is inadequate to separate the two surfaces in contact on that node.

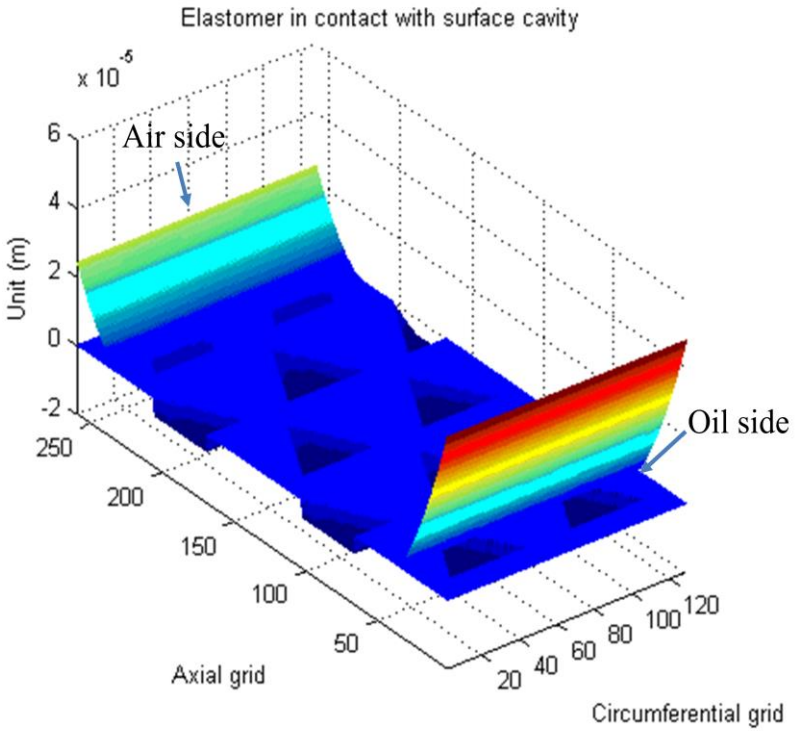

Figure 3.4.4 Elastomer in contact with the staggered triangular cavities

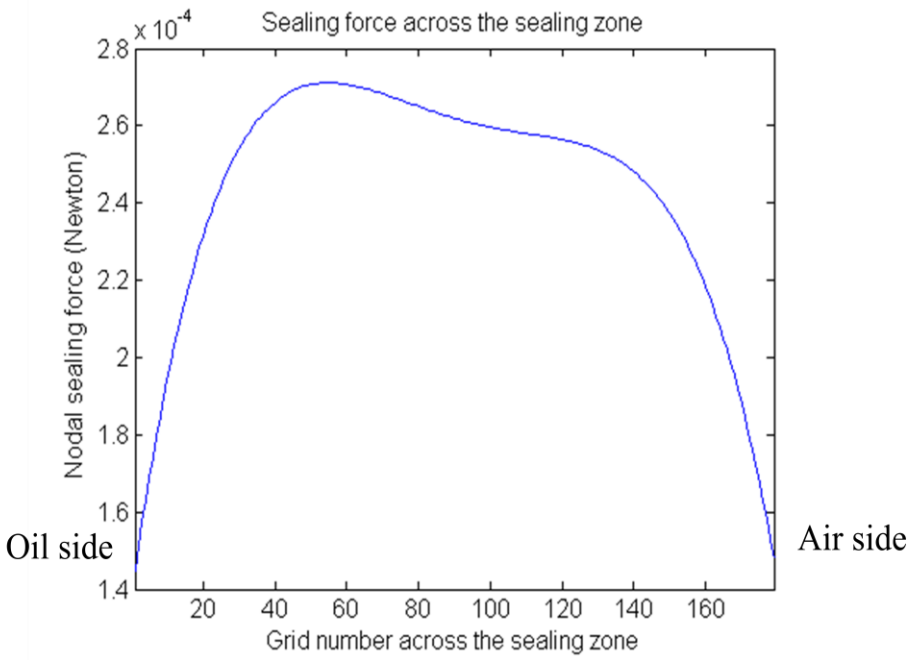

Figure 3.4.5 Axial sealing force for the lip seal in contact with a smooth shaft

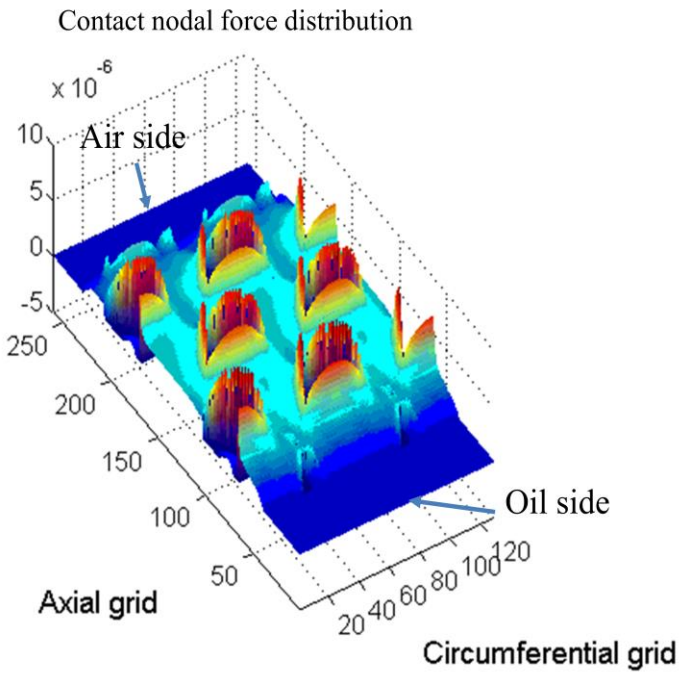

Figure 3.4.6 Sealing force distribution for lip seal in contact with a shaft having staggered triangular cavities on it

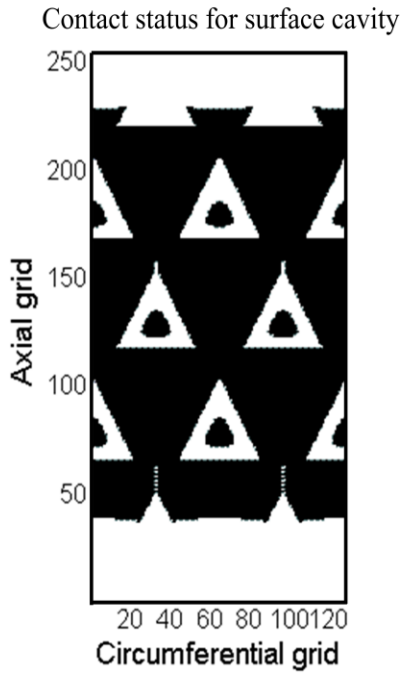

Figure 3.4.7 Contact status for the staggered triangular cavities

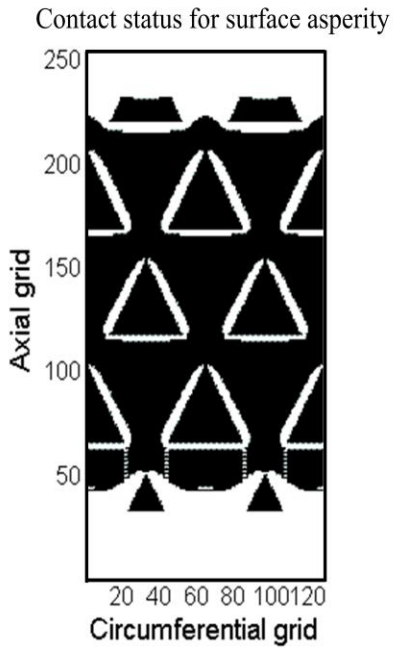

Figure 3.4.8 Contact status for the staggered triangular asperities

CHAPTER 4 FLUID DYNAMICS

4.1 Conventional Reynolds Equation

Similar to the solid mechanics in Chapter 3, fluid behavior complies with certain physical laws including the conservation of mass, the conservation of linear momentum and Newton's law of viscosity, which, in combination, results in the Navier-Stokes equations $(4.1.1 - 4.1.3)$ for incompressible fluids. The fluid dynamics analysis usually employs an Eulerian mesh as introduced in Section 3.1. A detailed derivation of the Navier-Stokes equation can be found in many references, including [89].

$$\rho\left(\frac{\partial u}{\partial t} + u\frac{\partial u}{\partial x} + v\frac{\partial u}{\partial y} + w\frac{\partial u}{\partial z}\right) = \rho g_x - \frac{\partial P}{\partial x} + \mu\left(\frac{\partial^2 u}{\partial x^2} + \frac{\partial^2 u}{\partial y^2} + \frac{\partial^2 u}{\partial z^2}\right) \qquad (4.1.1)$$

$$\rho\left(\frac{\partial v}{\partial t} + u\frac{\partial v}{\partial x} + v\frac{\partial v}{\partial y} + w\frac{\partial v}{\partial z}\right) = \rho g_y - \frac{\partial P}{\partial y} + \mu\left(\frac{\partial^2 v}{\partial x^2} + \frac{\partial^2 v}{\partial y^2} + \frac{\partial^2 v}{\partial z^2}\right) \qquad (4.1.2)$$

$$\rho\left(\frac{\partial w}{\partial t} + u\frac{\partial w}{\partial x} + v\frac{\partial w}{\partial y} + w\frac{\partial w}{\partial z}\right) = \rho g_z - \frac{\partial P}{\partial z} + \mu\left(\frac{\partial^2 w}{\partial x^2} + \frac{\partial^2 w}{\partial y^2} + \frac{\partial^2 w}{\partial z^2}\right) \qquad (4.1.3)$$

u, v, w are the velocity field variables in the x, y, z direction respectively, ρ is the fluid density, P is the fluid pressure, μ is the viscosity of the fluid, t is the time and g_x, g_y, g_z are the directional gravitational accelerations. In the lubrication problem, the

gravitational force is negligible compared to the viscous force since the "*Froude Number*" which represents the ratio of the viscous force to the gravitational force is very large as shown in, [90] page 49, and also shown in equation (4.1.4). In equation (4.1.4) h represents the lubricant (oil) film thickness, U is the relative speed between the two surfaces in relative sliding motion. Another reason for neglecting the gravitation term is that in the experiment (see Figure 5.1.1) the gravitational force of the oil stored in the oil collecting chamber (oil bath) is in equilibrium with the gravitational force of the oil stored in the graduate cylinder (oil head). The graduate cylinder is about 0.5 meter long and has a cross section diameter of 0.08 meter. Compared to the weight of the oil in the graduate cylinder the weight of the oil in the sealing zone is negligible as the sealing zone is only about 400 micrometer long and the oil film is only about 1-2 micrometer thick. If the lubricant flow is assumed to be a steady flow which is not time dependent equations $(4.1.1) - (4.1.3)$ become equations $(4.1.5) - (4.1.7)$

$$\frac{\mu U}{\rho g h^2} \approx O(1 \times 10^8) \tag{4.1.4}$$

$$\rho\left(u\frac{\partial u}{\partial x} + v\frac{\partial u}{\partial y} + w\frac{\partial u}{\partial z}\right) = -\frac{\partial P}{\partial x} + \mu\left(\frac{\partial^2 u}{\partial x^2} + \frac{\partial^2 u}{\partial y^2} + \frac{\partial^2 u}{\partial z^2}\right) \tag{4.1.5}$$

$$\rho\left(u\frac{\partial v}{\partial x} + v\frac{\partial v}{\partial y} + w\frac{\partial v}{\partial z}\right) = -\frac{\partial P}{\partial y} + \mu\left(\frac{\partial^2 v}{\partial x^2} + \frac{\partial^2 v}{\partial y^2} + \frac{\partial^2 v}{\partial z^2}\right) \tag{4.1.6}$$

$$\rho\left(u\frac{\partial w}{\partial x}+v\frac{\partial w}{\partial y}+w\frac{\partial w}{\partial z}\right)=-\frac{\partial P}{\partial z}+\mu\left(\frac{\partial^2 w}{\partial x^2}+\frac{\partial^2 w}{\partial y^2}+\frac{\partial^2 w}{\partial z^2}\right) \quad (4.1.7)$$

non-dimensionalizing equation (4.1.5) with

$$x=\bar{x}L_x \quad y=\bar{y}L_y \quad z=\bar{z}h \quad u=\bar{u}U \quad v=\bar{v}U \quad w=\bar{w}\frac{Uh}{L_x} \quad P=\bar{P}\frac{\mu UL_x}{h^2} \quad (4.1.8)$$

obtained:

$$\frac{U^2h^2}{L_x}\left(\bar{u}\frac{\partial \bar{u}}{\partial \bar{x}}+\frac{L_x}{L_y}\bar{v}\frac{\partial \bar{u}}{\partial \bar{y}}+\bar{w}\frac{\partial \bar{u}}{\partial \bar{z}}\right)=-\frac{\mu U}{\rho}\frac{\partial \bar{P}}{\partial \bar{x}}+\frac{\mu Uh^2}{\rho {L_x}^2}\left(\frac{\partial^2 \bar{u}}{\partial \bar{x}^2}+\frac{{L_x}^2}{{L_y}^2}\frac{\partial^2 \bar{u}}{\partial \bar{y}^2}\right)+\frac{\mu U}{\rho}\frac{\partial^2 \bar{u}}{\partial \bar{z}^2} \quad (4.1.9)$$

In the lubrication problem, the thickness of the thin oil film is much smaller than the other two characteristic dimensions: $h \ll L_x$ and $L_y \sim O(L_x)$ as shown in Figure 4.1.1. L_x represents the circumferential computational length while L_y represents the axial sealing zone width which is shown in Figure 3.3.3. Since h/L_x or $h/L_y \approx 0$ equation (4.1.9) simplifies to:

$$-\frac{\partial P}{\partial x}+\mu\frac{\partial^2 u}{\partial z^2}=0 \quad (4.1.10)$$

Similarly, the dimensionless version of equation (4.1.6) is :

$$\frac{U^2h^2}{L_x}\left(\bar{u}\frac{\partial\bar{v}}{\partial\bar{x}}+\frac{L_x}{L_y}\bar{v}\frac{\partial\bar{v}}{\partial\bar{y}}+\bar{w}\frac{\partial\bar{v}}{\partial\bar{z}}\right)=-\frac{\mu U}{\rho}\frac{L_x}{L_y}\frac{\partial\bar{P}}{\partial\bar{y}}+\frac{\mu Uh^2}{\rho{L_x}^2}\left(\frac{\partial^2\bar{v}}{\partial\bar{x}^2}+\frac{{L_x}^2}{{L_y}^2}\frac{\partial^2\bar{v}}{\partial\bar{y}^2}\right)+\frac{\mu U}{\rho}\frac{\partial^2\bar{v}}{\partial\bar{z}^2} \quad (4.1.11)$$

Since h/L_x or $h/L_y \approx 0$, equation (4.1.11) becomes:

$$-\frac{\partial P}{\partial y}+\mu\frac{\partial^2 v}{\partial z^2}=0 \quad (4.1.12)$$

The dimensionless version of equation (4.1.7) is:

$$\frac{U^2h^4}{{L_x}^3}\left(\bar{u}\frac{\partial\bar{w}}{\partial\bar{x}}+\frac{L_x}{L_y}\bar{v}\frac{\partial\bar{w}}{\partial\bar{y}}+\bar{w}\frac{\partial\bar{w}}{\partial\bar{z}}\right)=-\frac{\mu U}{\rho}\frac{\partial\bar{P}}{\partial\bar{z}}+\frac{\mu Uh^5}{\rho{L_x}^5}\left(\frac{\partial^2\bar{w}}{\partial\bar{x}^2}+\frac{{L_x}^2}{{L_y}^2}\frac{\partial^2\bar{w}}{\partial\bar{y}^2}\right)+\frac{\mu Uh^3}{\rho{L_x}^3}\frac{\partial^2\bar{w}}{\partial\bar{z}^2} \quad (4.1.13)$$

As h/L_x or $h/L_y \approx 0$ equation (4.1.13) becomes:

$$\frac{\partial P}{\partial z}=0 \quad (4.1.14)$$

Equation (4.1.14) simply means that there is no pressure gradient in the z direction inside the oil film layer.

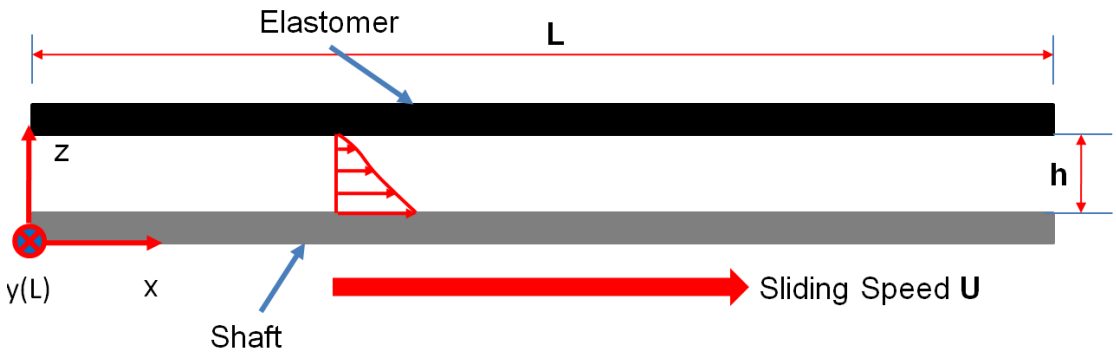

Figure 4.1.1 Dimension scale of the lubrication problem (axial view)

Integrating equation (4.1.10) and (4.1.12) with respect to z yields:

$$u = \frac{1}{\mu}\frac{\partial P}{\partial x}\frac{z^2}{2} + C_1 z + C_2 \tag{4.1.15}$$

$$v = \frac{1}{\mu}\frac{\partial P}{\partial y}\frac{z^2}{2} + C_3 z + C_4 \tag{4.1.16}$$

The no slip boundary conditions in the z direction $(4.1.17) - (4.1.20)$ are given as:

$$u(z = h) = 0 \tag{4.1.17}$$

$$u(z = 0) = U \tag{4.1.18}$$

$$v(z = h) = 0 \tag{4.1.19}$$

$$v(z = 0) = 0 \tag{4.1.20}$$

Plugging these conditions into equation (4.1.15) and (4.1.16) yields:

$$u = \frac{1}{2\mu}\frac{\partial P}{\partial x}(z^2 - zh) - \frac{U}{h}z + U \tag{4.1.21}$$

$$v = \frac{1}{2\mu}\frac{\partial P}{\partial y}(z^2 - zh) \tag{4.1.22}$$

The velocity fields with respect to x, y and z are given by equation (4.1.21) and (4.1.22). With the velocity fields the volumetric flow rate per unit length can be calculated as:

$$q_x \times 1 = 1\int_0^h u\,dz = 1\left(-\frac{h^3}{12\mu}\frac{\partial p}{\partial x} + U\frac{h}{2}\right) \quad \text{unit: } m^3/s \tag{4.1.23}$$

$$q_y \times 1 = 1\int_0^h v\,dz = 1\left(-\frac{h^3}{12\mu}\frac{\partial p}{\partial y}\right) \quad \text{unit: } m^3/s \tag{4.1.24}$$

The mass flow rate per unit length in x and y directions are:

$$\dot{m}_x = \rho_0 q_x \times 1 = \rho_0 1\left(-\frac{h^3}{12\mu}\frac{\partial P}{\partial x} + \frac{Uh}{2}\right) \quad \text{unit: Kg/s} \tag{4.1.25}$$

$$\dot{m}_y = \rho_0 q_y \times 1 = \rho_0 1\left(-\frac{h^3}{12\mu}\frac{\partial P}{\partial y}\right) \qquad \text{unit: Kg/s} \tag{4.1.26}$$

In equation $(4.1.25) - (4.1.26)$, ρ_0 represents the fluid density of the incompressible lubricant. The number "1" in equation $(4.1.23) - (4.1.26)$ means the flow flux or the mass flux refers to a unit length in x or y direction. The units following these equations will not be consistent without referring to a unit length. Assuming linear variation inside the control volume cell, a mass flux balance for a single control volume (shown in Figure 4.1.2) can be established as:

$$\rho_0\left(\frac{\partial q_x}{\partial x}\Delta x\right)\Delta y + \rho_0\left(\frac{\partial q_y}{\partial y}\Delta y\right)\Delta x = 0 \tag{4.1.27}$$

$\rho_0\left(\frac{\partial q_x}{\partial x}\Delta x\right)\Delta y$ represents the difference of the mass flux between the income flow and the outgoing flow in the x direction. $\rho_0\left(\frac{\partial q_y}{\partial y}\Delta y\right)\Delta x$ represents the difference of the mass flux between the income flow and the outgoing flow in the y direction. For a steady flow, the total mass flux for any control volume cell is zero.

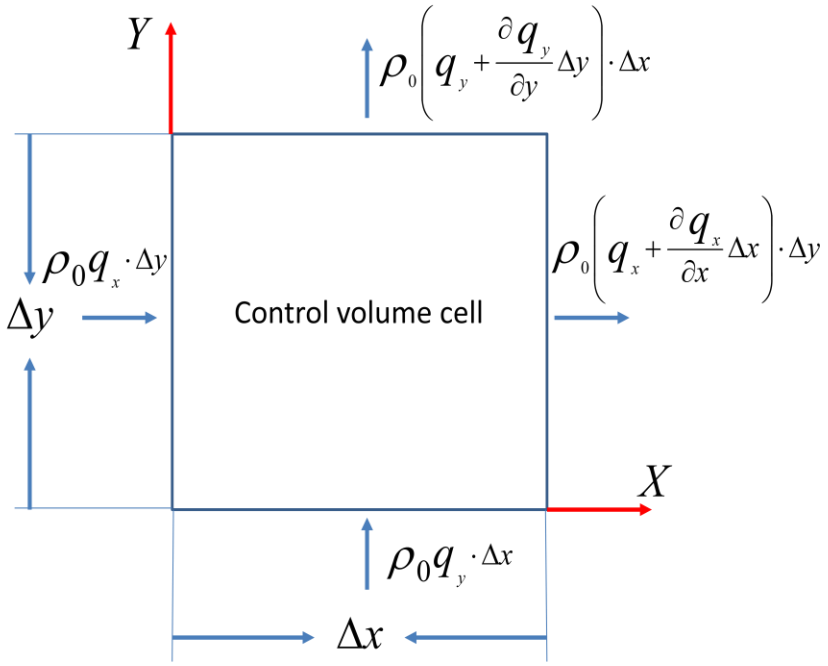

Figure 4.1.2 Mass flux balance for a single control volume

$$\rho_0 \frac{\partial q_x}{\partial x} + \rho_0 \frac{\partial q_y}{\partial y} = 0 \tag{4.1.28}$$

Plugging equations (4.1.23) and (4.1.24) into equation (4.1.28) obtained:

$$\rho_0 \frac{\partial}{\partial x}\left(\frac{h^3}{12\mu}\frac{\partial P}{\partial x}\right) + \rho_0 \frac{\partial}{\partial y}\left(\frac{h^3}{12\mu}\frac{\partial P}{\partial y}\right) = \rho_0 \frac{U}{2}\frac{\partial h}{\partial x} \tag{4.1.29}$$

Equation (4.1.29) is the conventional steady state Reynolds equation. The terms $\rho_0 \frac{\partial}{\partial x}\left(\frac{h^3}{12\mu}\frac{\partial P}{\partial x}\right)$ and $\rho_0 \frac{\partial}{\partial y}\left(\frac{h^3}{12\mu}\frac{\partial P}{\partial y}\right)$ represent the pressure driven flow (known as the Poiseuille flow in literature). The term $\rho_0 \frac{U}{2}\frac{\partial h}{\partial x}$ represents the shear driven flow due to the rotation of the shaft (known as the Couette flow in literature).

When equation (4.1.29) is applied to the conventional lip seal model, one key assumption is that the surface roughness on the shaft is negligible and the shaft surface is assumed to be perfectly smooth as shown in Figure 4.1.3. Based on this assumption, the local oil film thickness like h_1 and h_2 are not time variant even if the shaft rotates, thus a steady state flow field can be expected. This assumption is believed to be valid for the conventional lip seal since the shaft surface is polished such as it is much smoother than the elastomer surface during the "break in" process which is introduced in details in Chapter 2.

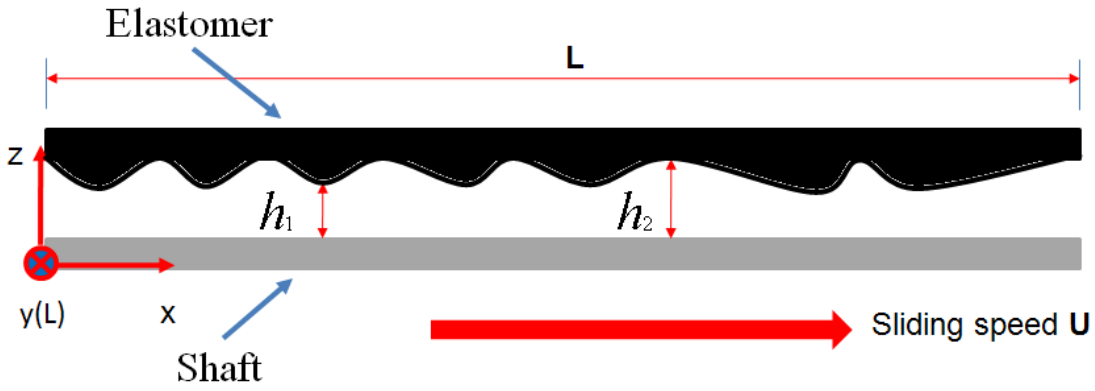

Figure 4.1.3 Surface roughness on the elastomer

In recent years, the use of artificial deterministic surface roughness on the shaft has become increasingly popular. The steady state Reynolds equation (4.1.29) is not sufficient for simulating the flow field disrupted by the shaft surface roughness. Because as shown in Figure 4.1.4 the surface roughness on the shaft moves together with the shaft as the shaft rotates. Consequently, the local oil film thickness h_1 and h_2 does change

over time. A transient version of Reynolds equation is needed to deal with the moving surface roughness on the shaft.

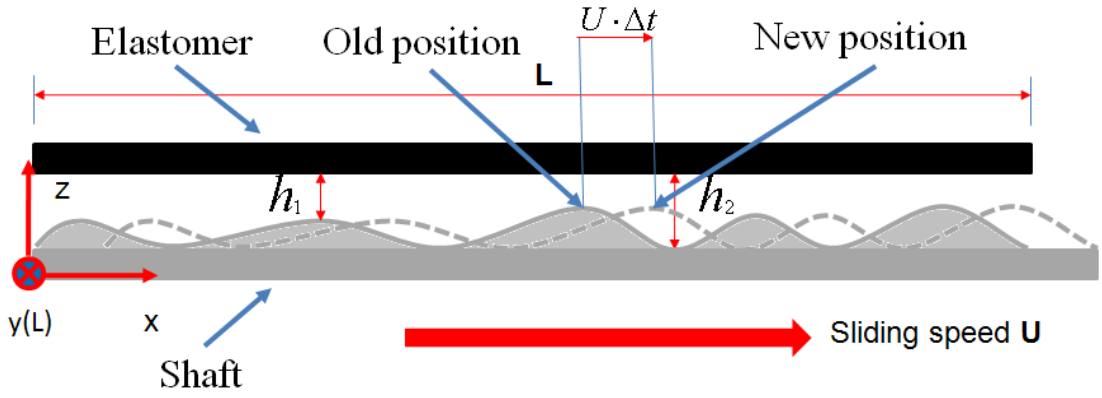

Figure 4.1.4 Surface roughness on the shaft

By inserting a squeezing term on the right hand side of equation (4.1.29), equation (4.1.30) is obtained.

$$\rho_0\left(\frac{\partial q_x}{\partial x}\Delta x\right)\Delta y+\rho_0\left(\frac{\partial q_y}{\partial y}\Delta y\right)\Delta x=-\rho_0\frac{\partial Vol}{\partial t} \tag{4.1.30}$$

In equation (4.1.30), the term $-\rho_0\frac{\partial Vol}{\partial t}$ represents the mass changing rate due to the thickness change of the local oil film. (Vol is the total volume of a single control volume) Since equation (4.1.30) needs to be satisfied over the entire domain, it is rewritten as equation (4.1.31).

$$\rho_0 \frac{\partial q_x}{\partial x} + \rho_0 \frac{\partial q_y}{\partial y} = -\rho_0 \frac{\partial h}{\partial t} \tag{4.1.31}$$

Inserting equation (4.1.23) and (4.1.24) into equation (4.1.31) gives:

$$\rho_0 \frac{\partial}{\partial x}\left(\frac{h^3}{12\mu}\frac{\partial P}{\partial x}\right) + \rho_0 \frac{\partial}{\partial y}\left(\frac{h^3}{12\mu}\frac{\partial P}{\partial y}\right) = \rho_0 \frac{U}{2}\frac{\partial h}{\partial x} + \rho_0 \frac{\partial h}{\partial t} \tag{4.1.32}$$

Equation (4.1.32) is the transient Reynolds equation. Theoretically, equation (4.1.32) should be used to analyze the surface roughness on the shaft to account for the squeeze oil film effect. However, equation (4.1.29) is still employed in most studies to conduct such an analysis neglecting the squeeze oil film effect (assuming the shaft roughness is stationary and not moving with the shaft) [7] [81] [79-80]. The main reason is because of the prohibitive computational cost. Equation (4.1.32) is a transient equation while equation (4.1.29) is a steady state equation. The cost for achieving a high accuracy transient analysis is very high especially when the fluid calculation is coupled with the solid deformation of the elastomer. Another reason is that the conventional Reynolds equation (4.1.29) and (4.1.32) needs to be modified to incorporate the JFO cavitation conditions. The cavitation (vapor bubble) crashes and reforms over time as the shaft roughness is displaced. This time dependent cavitation condition leads to a time dependent pumping rate which poses additional difficulty to the evaluation of the directional pumping ability of the surface textures.

4.2 JFO Theory and Modified Steady State Reynolds Equation

As introduced in section 4.1, the Reynolds equation, both in steady state version (4.1.29) and transient version (4.1.32), deal with the mass flux balance of a very thin oil film layer. The lubricant flow is assumed to be laminar and continuous dominated by a strong viscous effect. Known as the JFO cavitation theory, Jakobsson-Floberg [33] and Olsson [34] pointed out that the lubricant vaporizes and the cavitation (vapor bubble) forms in the oil film when the fluid pressure drops below a threshold value (cavitation threshold pressure) P_c. The flow in the cavitation area is a mixture of the fluid and the fluid vapors. Within the cavitation area there is no pressure gradient (the pressure everywhere within the cavitation area is the constant value P_c). Thus there is no pressure driven flow (Poiseuille flow). The oil in the cavitation area is transferred from the upstream to the downstream in x direction as striations by the viscous shear force (Couette flow due to the sliding of the shaft) (illustrated in Figure 4.2.1). Since cavitation is an important physical phenomenon which is believed to influence the load carrying ability and the pumping ability of the bearing and sealing components (see section 1.1), it is necessary to incorporate the cavitation into the conventional Reynolds equation. The steady state Reynolds equation (4.1.29) is first modified. Equation (4.1.29) is rewritten here as Equation (4.2.1) to facilitate the derivation.

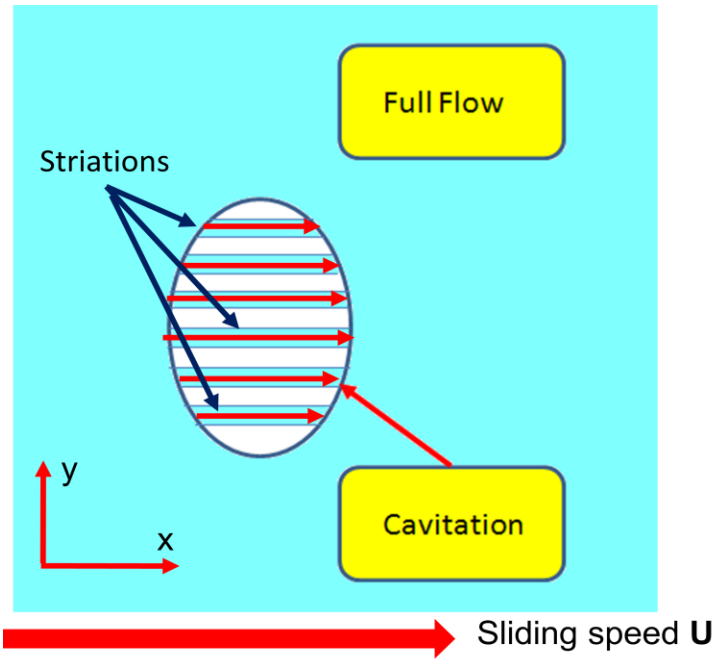

Figure 4.2.1 Cavitation area in the lubricant flow

Equation (4.2.1) dominates the behavior of the fluid in the non-cavitated area while equation (4.2.2) which is the continuity equation dominates in the cavitated area.

Governing equation in non-cavitated area:

$$\rho_0 \frac{\partial}{\partial x}\left(\frac{h^3}{12\mu}\frac{\partial P}{\partial x}\right) + \rho_0 \frac{\partial}{\partial y}\left(\frac{h^3}{12\mu}\frac{\partial P}{\partial y}\right) = \rho_0 \frac{U}{2}\frac{\partial h}{\partial x} \tag{4.2.1}$$

Governing equation in the cavitated area:

$$\frac{U}{2}\frac{\partial(h\rho)}{\partial x} = 0 \tag{4.2.2}$$

Note that equation (4.2.2) directly comes from the right hand side term $\rho_0 \frac{U}{2}\frac{\partial h}{\partial x}$ of equation (4.2.1). Because according to the JFO cavitation theory, there is only Couette flow inside the cavitation area conveyed by the rotation of the shaft. In equation (4.2.2) the lubricant density ρ is a function of x. This modification is made first because in the cavitation area the fluid is mixed with the fluid vapor and the density in equation (4.2.2) represents the density of the fluid-vapor mixture. Second because equation (4.2.2) must comply with the mass conservation within the cavitation area. The mass conservation requires that for a single control volume, the income mass flux must equal the outgoing mass flux. As shown in Figure 4.2.2, the local oil film thickness is a function of x (see h_1 and h_2) thus the density of the mixture must also be varied accordingly in the x direction to guarantee the income mass flux equals the outgoing mass flux.

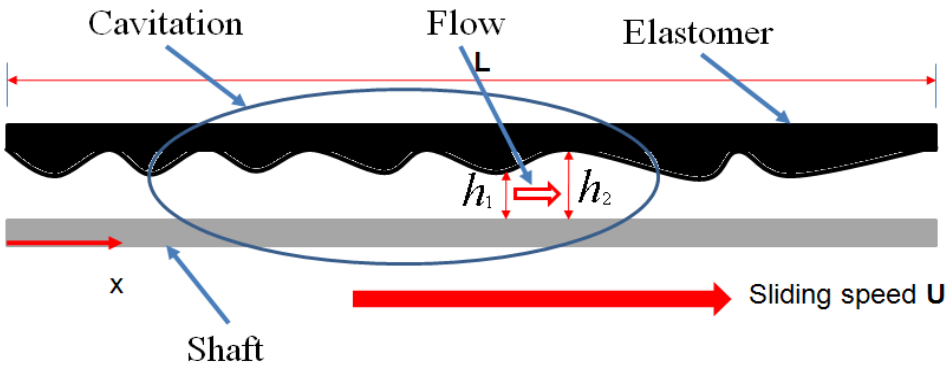

Figure 4.2.2 Mass conservation in the cavitation area

For different surface roughness pattern, the cavitation area is of different shape. A lot of work has been done to derive a generalized Reynolds equation which could

automatically identify the boundary of the non-cavitation area and the cavitation area as introduced in section 2.2. In this study the solution procedure used by Shen and Salant [51-53] is employed. Equation (4.2.1) and (4.2.2) can be non-dimensionalized using (4.2.3)

$$\bar{x} = \frac{x}{L_x}; \quad \bar{y} = \frac{y}{L_y}; \quad \bar{h} = \frac{h}{h_{max}}; \quad \bar{P} = \frac{P - P_c}{P_s - P_c}; \tag{4.2.3}$$

h_{max} is the maximum oil film thickness, P_c is the cavitation threshold pressure and P_s is the sealed fluid pressure. They are all constants.

Equation (4.2.1) becomes:

$$\frac{\partial}{\partial \bar{x}}\left(\bar{h}^3 \frac{\partial \bar{P}}{\partial \bar{x}}\right)\rho_0 + \lambda^2 \frac{\partial}{\partial \bar{y}}\left(\bar{h}^3 \frac{\partial \bar{P}}{\partial \bar{y}}\right)\rho_0 = \gamma \frac{\partial}{\partial \bar{x}}(\bar{h})\rho_0 \tag{4.2.4}$$

$$\lambda = \frac{L_x}{L_y}; \quad \gamma = \frac{6\mu U L_x}{h_{max}^2 (P_s - P_c)} \tag{4.2.5}$$

Equation (4.2.2) becomes

$$\gamma \frac{\partial}{\partial \bar{x}}(\rho \bar{h}) = 0 \tag{4.2.6}$$

Note that the coefficient γ for the nonzero term in equation (4.2.6) is the same as the coefficient for the right hand side term in equation (4.2.4). This is to insure the consistency of these two equations on the cavitation boundary where these two equations are combined.

Divide equation (4.2.4) and (4.2.6) by ρ_0 get

$$\frac{\partial}{\partial \bar{x}}\left(\bar{h}^3 \frac{\partial \bar{P}}{\partial \bar{x}}\right)1 + \lambda^2 \frac{\partial}{\partial \bar{y}}\left(\bar{h}^3 \frac{\partial \bar{P}}{\partial \bar{y}}\right)1 = \gamma \frac{\partial}{\partial \bar{x}}(\bar{h})1 \tag{4.2.7}$$

$$\gamma \frac{\partial}{\partial \bar{x}}(\bar{\rho}\bar{h}) = 0 \tag{4.2.8}$$

$$\bar{\rho} = \frac{\rho}{\rho_0} \tag{4.2.9}$$

The number 1 in equation (4.2.7) represents a unit density ratio $\frac{\rho_0}{\rho_0}$ of the lubricant flow in the non-cavitation area. Those terms in equation (4.2.7) and equation (4.2.8) represent the dimensionless mass flux. A universal variable and a switch function is defined to combine equation (4.2.7) and (4.2.8). The generalized Reynolds equation is:

$$\frac{\partial}{\partial \bar{x}}\left(\bar{h}^3 \frac{\partial(g\emptyset)}{\partial \bar{x}}\right)1 + \lambda^2 \frac{\partial}{\partial \bar{y}}\left(\bar{h}^3 \frac{\partial(g\emptyset)}{\partial \bar{y}}\right)1 = \gamma \frac{\partial\{[1 + (1-g)\emptyset]\bar{h}\}}{\partial \bar{x}} \tag{4.2.10}$$

In equation (4.2.10), $\emptyset$ is the universal variable and g is the switch function. The switch function is dependent on $\emptyset$ as

$$g = \begin{cases} 1 \text{ when } \emptyset > 0 \\ 0 \text{ when } \emptyset \leq 0 \end{cases} \tag{4.2.11}$$

If $\emptyset > 0$ in an area

$g = 1$

$$\frac{\partial}{\partial \bar{x}}\left(\bar{h}^3 \frac{\partial(g\emptyset)}{\partial \bar{x}}\right)1 = \frac{\partial}{\partial \bar{x}}\left(\bar{h}^3 \frac{\partial \emptyset}{\partial \bar{x}}\right)1$$

and

$$\lambda^2 \frac{\partial}{\partial \bar{y}}\left(\bar{h}^3 \frac{\partial(g\emptyset)}{\partial \bar{y}}\right)1 = \lambda^2 \frac{\partial}{\partial \bar{y}}\left(\bar{h}^3 \frac{\partial \emptyset}{\partial \bar{y}}\right)1$$

represents the mass flux due to the Poiseuille flow

While

$$\gamma \frac{\partial\{[1 + (1 - g)\emptyset]\bar{h}\}}{\partial \bar{x}}1 = \gamma \frac{\partial \bar{h}}{\partial \bar{x}}1$$

represents the mass flux due to the Couette flow

Equation (4.2.10) becomes:

$$\frac{\partial}{\partial \bar{x}}\left(\bar{h}^3 \frac{\partial \emptyset}{\partial \bar{x}}\right)1 + \lambda^2 \frac{\partial}{\partial \bar{y}}\left(\bar{h}^3 \frac{\partial \emptyset}{\partial \bar{y}}\right)1 = \gamma \frac{\partial \bar{h}}{\partial \bar{x}}1 \tag{4.2.12}$$

Equation (4.2.12) is exactly the same as equation (4.2.7) except that the dimensionless pressure term $\bar{P}$ is replaced by the universal variable $\emptyset > 0$.

If $0 > \emptyset > -1$ in another area, which means the fluid pressure P is smaller than the cavitation threshold pressure P_c causing the area to be cavitated, then

$g = 0$

$$\frac{\partial}{\partial \bar{x}}\left(\bar{h}^3 \frac{\partial(g\emptyset)}{\partial \bar{x}}\right) 1 = 0$$

and

$$\lambda^2 \frac{\partial}{\partial \bar{y}}\left(\bar{h}^3 \frac{\partial(g\emptyset)}{\partial \bar{y}}\right) 1 = 0$$

the mass flux due to the Poiseuille flow is switched off

While

$$\gamma \frac{\partial\{[1 + (1 - g)\emptyset]\bar{h}\}}{\partial \bar{x}} 1 = \gamma \frac{\partial\{[1 + \emptyset]\bar{h}\}}{\partial \bar{x}}$$

represents the mass flux due to the Couette flow and the oil density ratio is smaller than 1 in the cavitated area.

Equation (4.2.10) becomes:

$$\gamma \frac{\partial\{[1 + \emptyset]\bar{h}\}}{\partial \bar{x}} = 0 \qquad (4.2.13)$$

Equation (4.2.13) is exactly the same as equation (4.2.8) except that the

dimensionless mixture density $\bar{\rho}$ is replaced by the universal variable $-1 < 1 + \emptyset < 0$

It will be shown further that the difference equation of the generalized differential equation (4.2.10) could handle more complicated situations on cavitation boundary.

An analytical solution for the equation (4.2.10) is not possible and a numerical method is needed. Control volume method is used to discretize the generalized differential equation (4.2.10). As shown in Figure 4.2.3 the solution domain can be subdivided into many small control volume cells. As the number of the control volume increases, the resolution of the solution increases. A grid study shows a converging trend of the solution as the grid spacing decreases. 1 μm grid spacing is proper for this study.

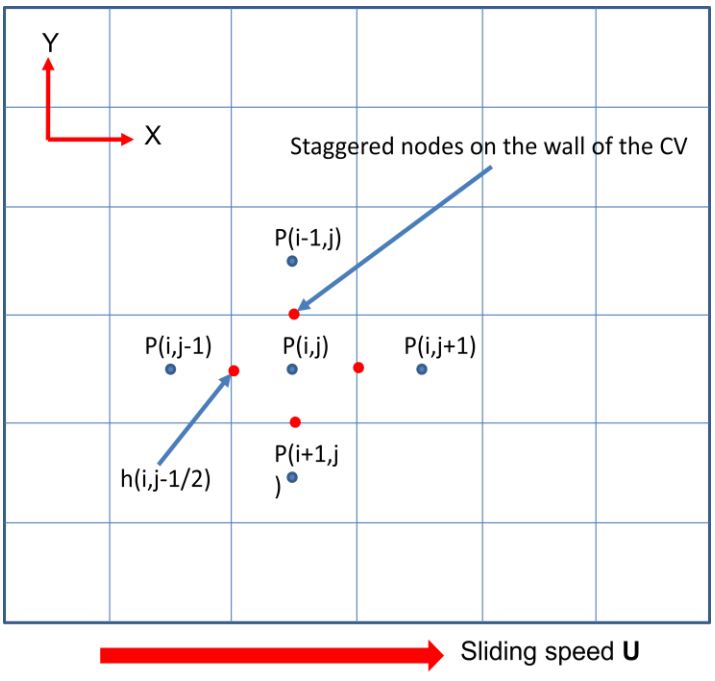

Figure 4.2.3 Discretization of the solution domain

Discretization of the space terms:

The three terms in the generalized differential equation (4.2.10) can be discretized from the left to the right as:

$$\frac{\partial}{\partial \bar{x}}\left(\bar{h}^3 \frac{\partial g\emptyset}{\partial \bar{x}}\right)$$

$$= \frac{1}{\Delta \bar{x}}\left\{\frac{\bar{h}^3(i, j+1/2)}{\Delta \bar{x}}[g(i, j+1)\emptyset(i, j+1) - g(i, j)\emptyset(i, j)]\right.$$

$$\left. - \frac{\bar{h}^3(i, j-1/2)}{\Delta \bar{x}}[g(i, j)\emptyset(i, j) - g(i, j-1)\emptyset(i, j-1)]\right\}$$

$$= \frac{1}{(\Delta \bar{x})^2}\{\bar{h}^3(i, j-1/2)[g(i, j-1)\emptyset(i, j-1) - g(i, j)\emptyset(i, j)]$$

$$+ \bar{h}^3(i, j+1/2)[g(i, j+1)\emptyset(i, j+1) - g(i, j)\emptyset(i, j)]\} \qquad (4.2.14)$$

$$\lambda^2 \frac{\partial}{\partial \bar{y}}\left(\bar{h}^3 \frac{\partial g\emptyset}{\partial \bar{y}}\right)$$

$$= \frac{\lambda^2}{\Delta \bar{y}}\left\{\frac{\bar{h}^3(i+1/2, j)}{\Delta \bar{y}}[g(i+1, j)\emptyset(i+1, j) - g(i, j)\emptyset(i, j)]\right.$$

$$\left. - \frac{\bar{h}^3(i-1/2, j)}{\Delta \bar{y}}[g(i, j)\emptyset(i, j) - g(i-1, j)\emptyset(i-1, j)]\right\}$$

$$= \frac{\lambda^2}{(\Delta \bar{y})^2}\{\bar{h}^3(i-1/2, j)[g(i-1, j)\emptyset(i-1, j) - g(i, j)\emptyset(i, j)]$$

$$+ \bar{h}^3(i+1/2, j)[g(i+1, j)\emptyset(i+1, j) - g(i, j)\emptyset(i, j)]\} \qquad (4.2.15)$$

$$\gamma \frac{\partial\{[1 + (1-g)\emptyset]\bar{h}\}}{\partial \bar{x}}$$

$$= \frac{1}{\Delta\bar{x}}\gamma\{\left[1 + \left(1 - g(i,j)\right)\emptyset(i,j)\right]\bar{h}(i,j+1) - \left[1 + \left(1 - g(i,j-1)\right)\emptyset(i,j-1)\right]\bar{h}(i,j-1)\} \quad (4.2.16)$$

Harmonic average is used for the coefficients on the wall of the control volume (staggered grid shown in Figure 4.2.3) because harmonic average could yield a smoother grid function for $\bar{h}^3$ as oil film thickness distribution $\bar{h}$ experiences large fluctuation.

$$\bar{h}^3(i,j-1/2) = \frac{\bar{h}^3(i,j-1)\cdot\bar{h}^3(i,j)}{2\cdot\left(\bar{h}^3(i,j-1)+\bar{h}^3(i,j)\right)} \quad (4.2.17)$$

$$\bar{h}^3(i,j+1/2) = \frac{\bar{h}^3(i,j)\cdot\bar{h}^3(i,j+1)}{2\cdot\left(\bar{h}^3(i,j)+\bar{h}^3(i,j+1)\right)} \quad (4.2.18)$$

$$\bar{h}^3(i-1/2,j) = \frac{\bar{h}^3(i-1,j)\cdot\bar{h}^3(i,j)}{2\cdot\left(\bar{h}^3(i-1,j)+\bar{h}^3(i,j)\right)} \quad (4.2.19)$$

$$\bar{h}^3(i+1/2,j) = \frac{\bar{h}^3(i,j)\cdot\bar{h}^3(i+1,j)}{2\cdot\left(\bar{h}^3(i,j)+\bar{h}^3(i+1,j)\right)} \quad (4.2.20)$$

$$\bar{h}\left(i,j-\frac{1}{2}\right) = \frac{\bar{h}(i,j-1)+\bar{h}(i,j)}{2} \quad (4.2.21)$$

$$\bar{h}\left(i,j+\frac{1}{2}\right) = \frac{\bar{h}(i,j)+\bar{h}(i,j+1)}{2} \quad (4.2.22)$$

$$\bar{h}\left(i-\frac{1}{2},j\right)=\frac{\bar{h}(i-1,j)+\bar{h}(i,j)}{2} \tag{4.2.23}$$

$$\bar{h}\left(i+\frac{1}{2},j\right)=\frac{\bar{h}(i,j)+\bar{h}(i+1,j)}{2} \tag{4.2.24}$$

Putting those terms in equations $(4.2.14)-(4.2.16)$ together one can get the difference equation $(4.2.25)$ of the generalized differential equation $(4.2.10)$

$$\begin{aligned}&\frac{1}{(\Delta\bar{x})^2}\{\bar{h}^3(i,j-1/2)[g(i,j-1)\emptyset(i,j-1)-g(i,j)\emptyset(i,j)]\\&\qquad+\bar{h}^3(i,j+1/2)[g(i,j+1)\emptyset(i,j+1)-g(i,j)\emptyset(i,j)]\}\\&+\frac{\lambda^2}{(\Delta\bar{y})^2}\{\bar{h}^3(i-1/2,j)[g(i-1,j)\emptyset(i-1,j)-g(i,j)\emptyset(i,j)]\\&\qquad+\bar{h}^3(i+1/2,j)[g(i+1,j)\emptyset(i+1,j)-g(i,j)\emptyset(i,j)]\}\\&-\frac{1}{\Delta\bar{x}}\gamma\{[1+(1-g(i,j))\emptyset(i,j)]\bar{h}(i,j+1)-[1+(1-g(i,j-1))\emptyset(i,j-1)]\bar{h}(i,j-1)\}\\&=0\end{aligned} \tag{4.2.25}$$

In the difference equation $(4.2.25)$, the switch function g determines the status of each control volume cell, where $g=0$ means the cell is cavitated and it can't drive the fluid into the neighboring cells by pressure gradient, while the fluid could still be driven into the cavitated cell from the neighboring non-cavitated cells by the pressure gradient. Figure 4.2.4 shows one possible situation on the boundary of the cavitation.

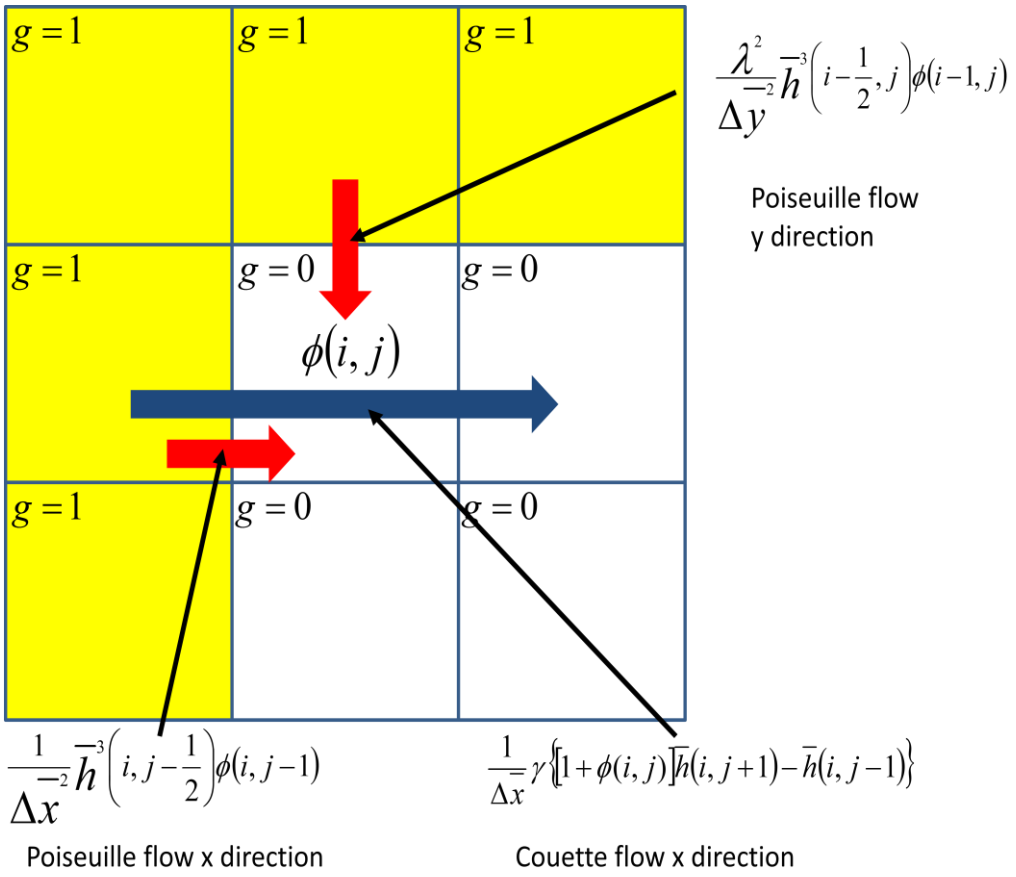

Figure 4.2.4 Lubricant flow across the cavitation boundary

In Figure 4.2.4, since the switch function on the non-cavitated side is unit, the Poiseuille term in the non-cavitated area is not switched off. For the central control volume shown in Figure 4.2.4, the difference equation (4.2.25) becomes:

$$\frac{1}{(\Delta\bar{x})^2}\bar{h}^3\left(i,j-\frac{1}{2}\right)\emptyset(i,j-1)+\frac{\lambda^2}{(\Delta\bar{y})^2}\bar{h}^3\left(i-\frac{1}{2},j\right)\emptyset(i-1,j)$$

$$=\frac{1}{\Delta\bar{x}}\gamma\{[1+\emptyset(i,j)]\bar{h}(i,j+1)-\bar{h}(i,j-1)\} \qquad (4.2.26)$$

There are only three terms in equation (4.2.26) since other terms are switched off as a

consequence of $g = 0$. These three terms are expressed separately in equations $(4.2.27) - (4.2.29)$ and their physical meaning is shown in Figure 4.2.4.

$$\frac{1}{(\Delta\bar{x})^2}\bar{h}^3\left(i, j-\frac{1}{2}\right)\emptyset(i, j-1)$$
$$= \frac{1}{(\Delta\bar{x})^2}\bar{h}^3\left(i, j-\frac{1}{2}\right)[1\times\emptyset(i, j-1) - 0\times\emptyset(i, j)] \quad (4.2.27)$$

$$\frac{\lambda^2}{(\Delta\bar{y})^2}\bar{h}^3\left(i-\frac{1}{2}, j\right)\emptyset(i-1, j)$$
$$= \frac{\lambda^2}{(\Delta\bar{y})^2}\bar{h}^3\left(i-\frac{1}{2}, j\right)[1\times\emptyset(i-1, j) - 0\times\emptyset(i, j)] \quad (4.2.28)$$

$$\frac{1}{\Delta\bar{x}}\gamma\{[1+\emptyset(i, j)]\bar{h}(i, j+1) - \bar{h}(i, j-1)\}$$
$$= \frac{1}{\Delta\bar{x}}\gamma\{[1+(1-0)\times\emptyset(i, j)]\bar{h}(i, j+1) - [1+(1-1)\times\emptyset(i, j-1)]\bar{h}(i, j-1)\} \quad (4.2.29)$$

Note that in equation $(4.2.27)$ and $(4.2.28)$ $\emptyset(i, j) > 0$ defining the dimensionless fluid pressure. While in equation $(4.2.29)$ $0 > \emptyset(i, j) > -1$ and $1 + \emptyset(i, j)$ defines the cavitation flow density ratio.

Equation $(4.2.26)$ shows only one possible situation on the boundary between the cavitated and the non-cavitated area. The rest of the situations are analogous to this situation. The mass flux balance is preserved across the boundary of the vapor bubbles.

Boundary conditions:

For the lip seal model, a Dirichlet boundary condition is prescribed in the y direction and cyclic boundary condition is given in the x direction as shown in Figure 4.2.5. Dirichlet boundary condition is actually a given value for the unknowns on the boundary. The cyclic boundary condition means the nodes on colum 1 are equivalent in value to the nodes on column m.

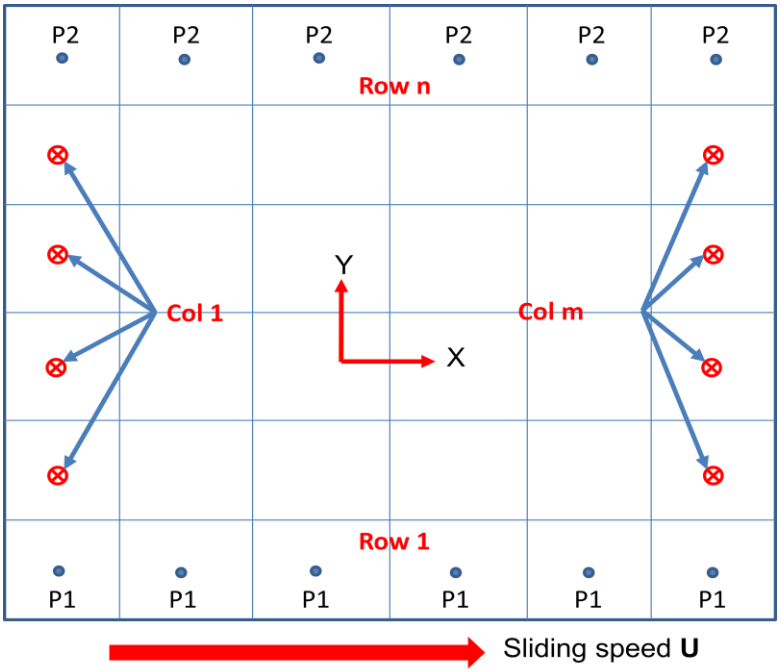

Figure 4.2.5 Boundary conditions for the solution domain

$$\emptyset_{y=0} = P_1 \tag{4.2.30}$$

$$\emptyset_{y=Ly} = P_2 \tag{4.2.31}$$

$$\emptyset_{x=0} = \emptyset_{x=Lx} \tag{4.2.32}$$

$$\frac{\partial \emptyset}{\partial x}_{x=0} = \frac{\partial \emptyset}{\partial x}_{x=Lx} \tag{4.2.33}$$

Solutions:

After the domain is discretized and the boundary conditions are prescribed, Black and Red Successive Line Over-relaxation (SLOR) [91-92] is used to solve the difference equation row by row (or column by column) iteratively. For the fix point iteration to function properly, an initial guess is needed. As Dirichlet boundary condition is prescribed in the y direction (axial direction), a linear average of the boundary values are prescribed row by row over the entire domain. For each row (or column) of the nodes a matrix equation $(4.2.34)$ can be formed

$$[A]\{\emptyset\} = \{b\} \tag{4.2.34}$$

For different boundary conditions matrix $[A]$ can have different structures. If SLOR is used to swipe the solution domain column by column, Dirichlet boundary conditions at the two ends of each column will make the matrix $[A]$ in the three banded compact form and LU decomposition for compact three banded matrix [91-93] (also known as Thomas algorithm) can be directly used to solve the equation $(4.2.34)$. If SLOR swipes the solution domain row by row, cyclic boundary conditions at the two ends of each row will

make the matrix [A] in the form as shown in Figure 4.2.6. The two off-diagonal nonzero elements b and c are caused by the cyclic boundary condition. In this case, Sherman-Morrison Formula [93] can be used to modify the matrix [A] getting rid of b and c. Then the Thomas algorithm could again come into use. The switch function is updated after the calculation for each row (or column) is completed. Both the unknown $\emptyset$ and the switch function g should be under-relaxed to maintain the numerical stability and also to guarantee the converged solution falls in the desired solution domain for the nonlinear difference equation (4.2.25).

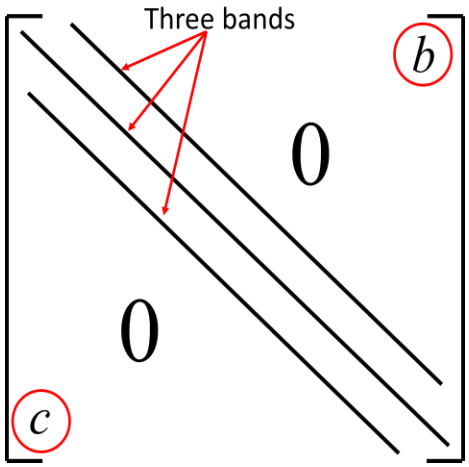

Figure 4.2.6 Matrix [A] for the cyclic boundary condition

Also note that in equation (4.2.25), the discretization for the Couette flow term employs central differencing for the oil film thickness $\bar{h}$, while backward differencing (up-wind differencing) is employed for the universal variable $\emptyset$. This treatment is to guarantee the diagonal dominance [91-92] of the matrix [A] in the cavitation area. This

requirement is imposed by the fixed-point iterative algorithm like SLOR or Successive point over-relaxation (SOR) [91-92].

Convergence:

In the physical system, the x direction flow is much greater than the y direction flow because of the rotating of the shaft. Thus the requirement for the accuracy of the solution is very high. A very small tolerance is needed for the Cauchy convergence criteria [91]. In this study the difference for the universal variable $\emptyset$ between two iterations in the SLOR should at least be smaller than 1×10^{-6}. The value of 1×10^{-10} would be the best if the computational resource permits.

Benchmark of the computational code:

To validate the algorithm and to avoid unexpected coding error, the numerical solution is benchmarked to a known analytical solution. The analytical case used in this study is a step slider which is also used in reference [85]. As shown in Figure 4.2.7, the step slider is assumed to be infinite long in the y direction which is perpendicular to the sliding direction (x direction). At the entrance and the exit of the step slider, the boundary pressure is the ambient pressure.

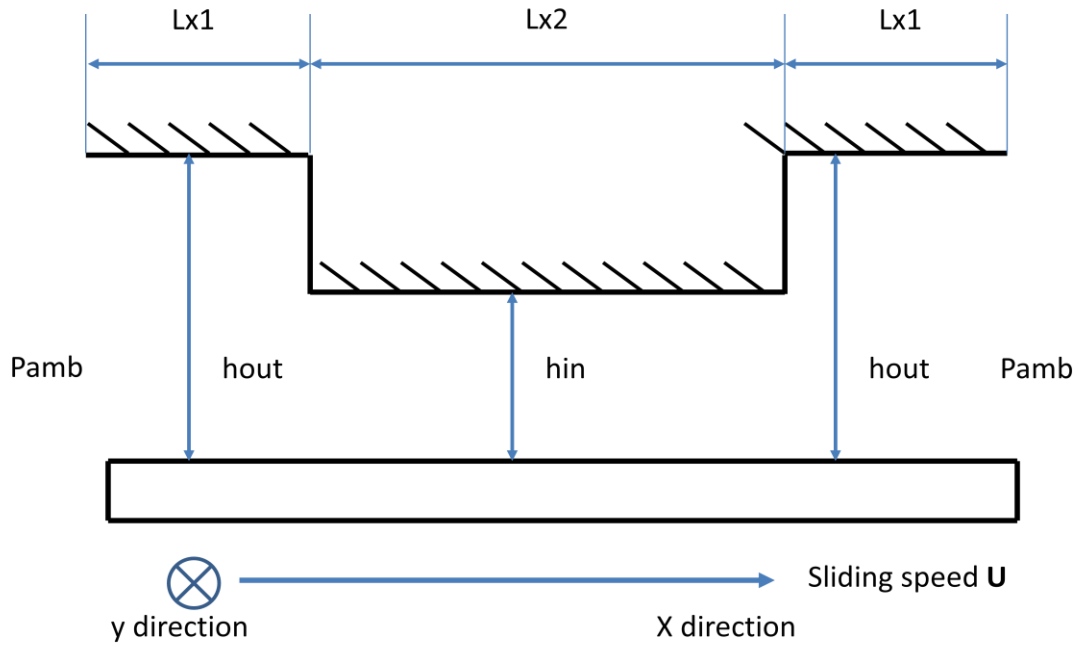

Figure 4.2.7 Infinite long step slider

The differential equation governing the infinite long step slider is given as:

$$\frac{d}{dx}\left(h^3\frac{dP}{dx}\right) = 6\mu U\frac{dh}{dx} \tag{4.2.35}$$

The analytical solution of equation (4.2.35) has been derived in detail in Chapter 5 of reference [85] and is given below as:

$$P_1(x) = \beta_1 x + \beta_2 \ \ (0 \le x \le L_{x1}) \tag{4.2.36}$$

$$P_2(x) = \beta_3 x + \beta_4 \ \ (L_{x1} \le x \le L_{x1} + L_{x2}) \tag{4.2.37}$$

$$P_3(x) = \beta_5 x + \beta_6 \ \ (L_{x1} + L_{x2} \le x \le 2L_{x1} + L_{x2}) \qquad (4.2.38)$$

$$\beta_1 = \frac{6\mu U L_{x2}(h_{out} - h_{in})}{2L_{x1}{h_{in}}^3 + L_{x2}{h_{out}}^3} \qquad (4.2.39)$$

$$\beta_2 = P_{amb} \qquad (4.2.40)$$

$$\beta_3 = \frac{12\mu U L_{x1}(h_{in} - h_{out})}{2L_{x1}{h_{in}}^3 + L_{x2}{h_{out}}^3} \qquad (4.2.41)$$

$$\beta_4 = \frac{6\mu U L_{x1}(h_{out} - h_{in})(2L_{x1} + L_{x2})}{2L_{x1}{h_{in}}^3 + L_{x2}{h_{out}}^3} + P_{amb} \qquad (4.2.42)$$

$$\beta_5 = \frac{6\mu U L_{x2}(h_{out} - h_{in})}{2L_{x1}{h_{in}}^3 + L_{x2}{h_{out}}^3} \qquad (4.2.43)$$

$$\beta_6 = \frac{6\mu U L_{x2}(h_{in} - h_{out})(2L_{x1} + L_{x2})}{2L_{x1}{h_{in}}^3 + L_{x2}{h_{out}}^3} + P_{amb} \qquad (4.2.44)$$

The following numeric values from reference [85] are used for the benchmark study

$L_{x1} = 25 \times 10^{-6}\text{m}; \quad L_{x2} = 50 \times 10^{-6}\text{m};$

$h_{out} = 5.08 \times 10^{-6}\text{m}; \quad h_{in} = 2.54 \times 10^{-6}\text{m};$

$P_{amb} = 101325\ \text{Pa}; \quad \mu = 0.0549\ \text{Pa.s}; \quad U = 5.486\text{m/s} \qquad (4.2.45)$

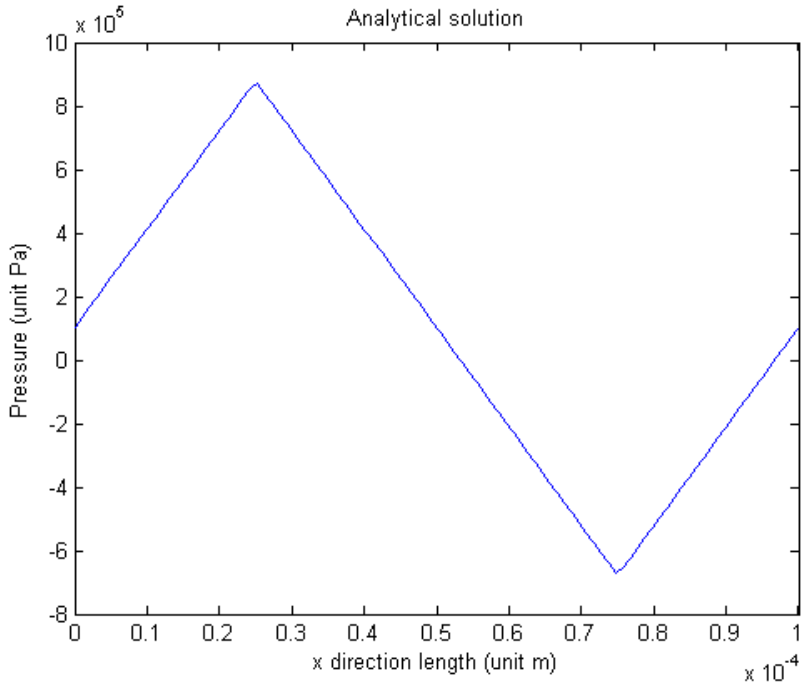

Figure 4.2.8 Analytical solution for the 2-D step slider

Figure 4.2.8 shows the analytical solution. Equation (4.2.35) is a 2-D model for an infinitely long step slider. However the generalized Reynolds equation (4.2.10) is a 3-D model which can't be compared to the 2-D model directly. To solve this problem, for the 3-D model the computational length in the direction perpendicular to the sliding direction is assigned 5 times longer than the computational length in the sliding direction to approximate an infinite long step slider. As shown in Figure 4.2.9, ambient pressure is assigned on the four boundaries for the 3-D step slider.

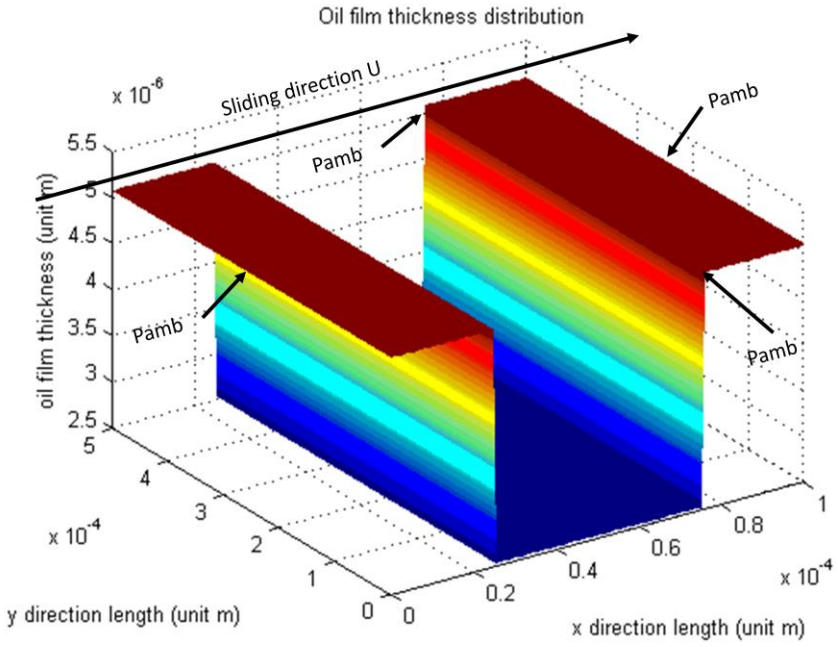

Figure 4.2.9 Oil film distribution for a 3-D step slider

Numeric values for the 3-D step slider is given as:

$L_x = 100 \times 10^{-6}\text{m}; \quad L_y = 500 \times 10^{-6}\text{m}$

$h_{out} = 5.08 \times 10^{-6}\text{m}; \quad h_{in} = 2.54 \times 10^{-6}\text{m}$

$P_{amb} = 101325\ \text{Pa}; \quad \mu = 0.0549\ \text{Pa.s}; \quad U = 5.486\ \text{m/s}$

$n = 1000; \quad m = 200$ (4.2.46)

L_x and L_y are the computational length in x and y direction respectively.

m and n are the computational node number in the x and y direction respectively. Initial benchmark does not contain cavitation, which is achieved simply by setting the switch function in equation (4.2.25) always to be 1. Figure 4.2.10 shows the pressure distribution for the 3-D step slider without cavitation. Though the 3-D step slider is not

infinitely long, its length in y direction is much larger than the length in x direction and the 3-D slider's geometry is symmetrical about the middle plane along the y direction. One can expect that the pressure distribution on the middle plane along the y direction should be close to the analytical pressure distribution for the 2-D infinite long slider.

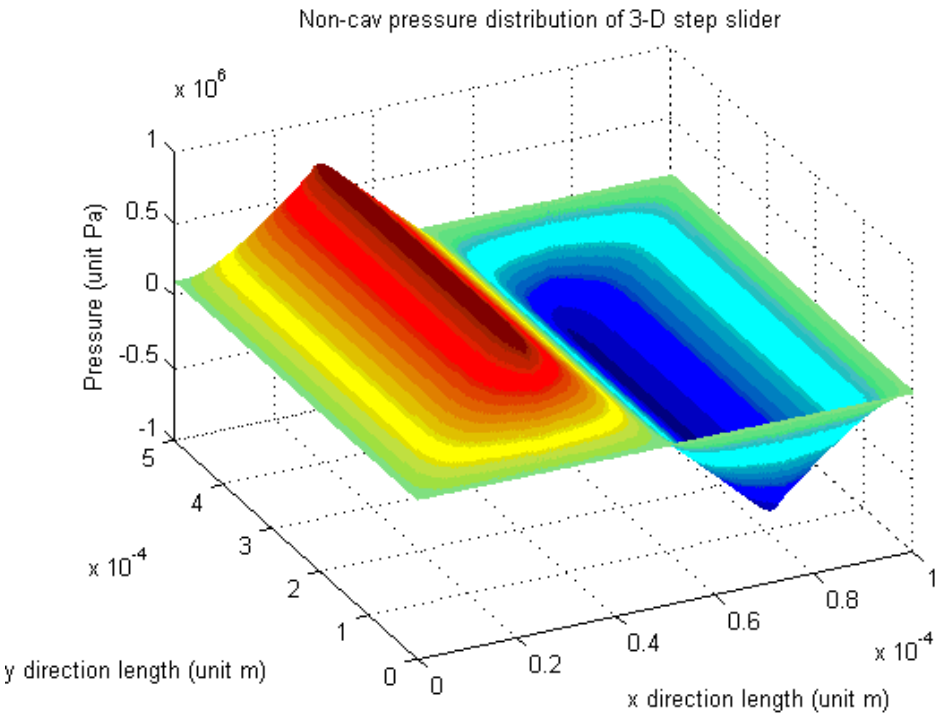

Figure 4.2.10 Pressure distribution for the 3-D step slider (without cavitation)

Figure 4.2.11 shows the middle plane pressure distribution of the 3-D step slider compared to the analytical solution of the 2-D step slider. The numerical solution matches the analytical solution very well which demonstrates the accuracy of the numerical solving procedure. Again note that cavitation is not included in the initial comparison. Also note that this benchmark only verify that the numerical method can be used to solve

equation (4.2.10). The ability of equation (4.2.10) to approximate the real physical system could only be validated through a comparison to the Navier-Stokes equation solution or to the experiment results, which is not discussed here.

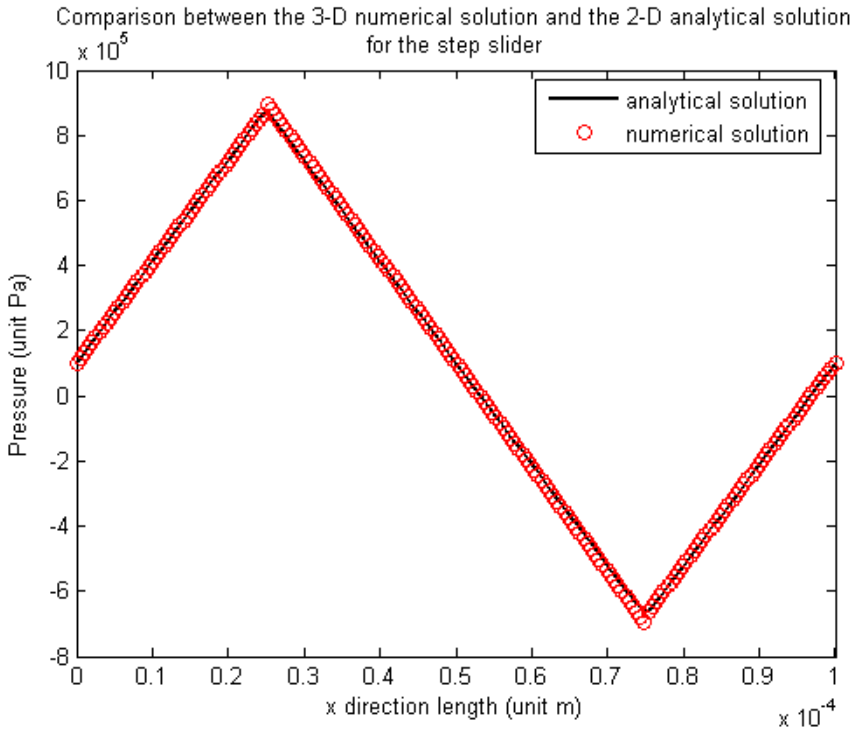

Figure 4.2.11 Comparison between the analytical solution and the numerical solution (middle plane without cavitation)

Figure 4.2.12 shows the pressure distribution for the step slider considering the JFO cavitation. All the numeric values in this case are the same as in (4.2.46) expect that one more parameter, the "cavitation pressure", is added. The "cavitation pressure" in use is zero. One can see in Figure 4.2.12 and Figure 4.2.13 that the fluid pressure below zero is truncated by the cavitation and the cavitation also elevates the up-stream fluid pressure.

Because, in the cavitation area, the x direction pressure driven flow is switched off,

the shear driven flow which is motivated by the motion of the slider is unchanged. In this case, the presence of cavitation actually decreases the total amount of fluid that is transferred from the up-stream to the down-stream across the cavitation area. Consequently the fluid pressure rises on the up-stream boundary of the vapor bubble where the fluid is subject to more impedance compared to the non-cavitation situation as shown in Figure 4.2.13.

The comparison between the solution which does not consider cavitation and the solution which does, again proves the previous research conclusions of Salant et.al [1] [42-43] [49-53] that vapor bubbles (cavitation) within the lubricant flow could provide an extra load carrying capacity. Figure 4.2.13 shows the similar idea as Figure 1.1.2 does.

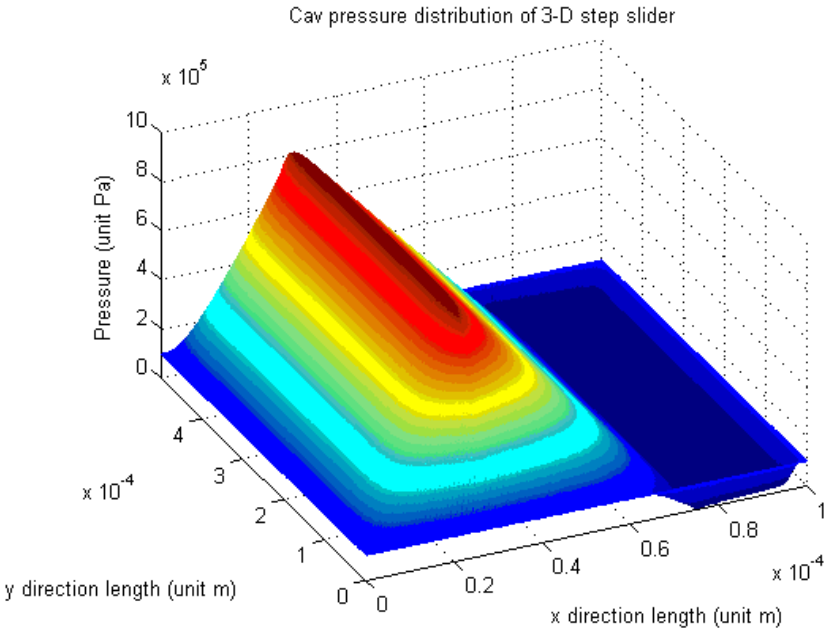

Figure 4.2.12 Pressure distribution for the 3-D step slider (with cavitation)

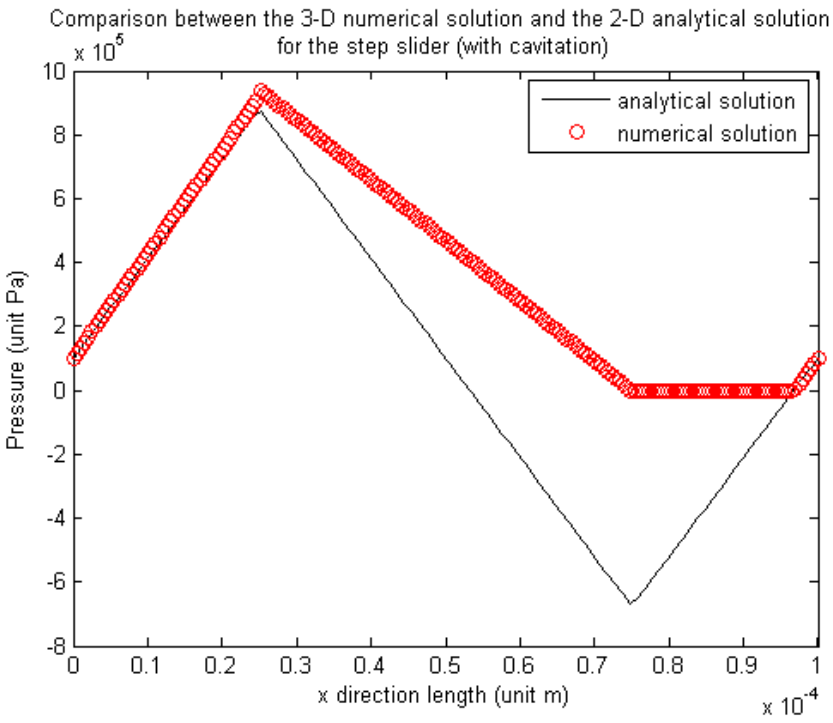

Figure 4.2.13 Comparison between the analytical solution and the numerical solution (middle plane with cavitation)

Application of the steady state Reynolds equation to the lip seal:

In the above benchmark study, Dirichlet boundary conditions are applied on all of the boundaries. The boundary condition for the lip seal model is slight different. Since the circumferential computational length of the lip seal model is only a small fraction of the whole circumference and it is assumed that the surface roughness pattern repeats itself along the circumferential direction, cyclic boundary conditions are applied in the circumferential x direction as shown in Figure 4.2.5.

Figure 4.2.14 shows an example oil film distribution for the lip seal. In Figure 4.2.14 the local oil film between the elastomer and the shaft varies in both the circumferential x direction and the axial y direction due to the surface roughness on the elastomer which

assumes a 2-D sinusoidal pattern as given in equation (4.2.47). The other numeric values are given in equation (4.2.48). Figure 4.2.15 shows the oil film pressure distribution corresponding to the oil film distribution shown in Figure 4.2.14. Apparently the inter-asperity cavitation (cavitation area formed in the diverging area the sinusoidal oil film thickness) which is indicated by the cavitation index in Figure 4.2.16 has a great influence on the pressure distribution as the cavitation truncates the negative fluid pressure. It can also be seen in Figure 4.2.16 that the cavitation region extends across the circumferential boundaries due the cyclic boundary conditions.

$$h = 0.5 \times 10^{-6} \times \sin(2\pi x \times 7/L_x) \times \sin\left(2\pi x \times 10/L_y\right) + 1 \times 10^{-6} \ \text{(m)} \quad (4.2.27)$$

$$L_x = 300 \times 10^{-6}\text{m}; \quad L_y = 400 \times 10^{-6}\text{m}$$

$$P_{amb} = 101325 \text{ Pa}; \quad P_c = 0 \text{ Pa}; \quad \mu = 0.035 \text{ Pa. s}; \quad U = 5.486 \text{ m/s}$$

$$n = 400; \quad m = 300 \quad (4.2.48)$$

Figures 4.2.17-4.2.19 shows another example oil film distribution corresponding to a single triangular surface cavity. It is seen that the negative fluid pressure on the diverging side of the oil film is truncated by the cavitation. The cavitation index is shown in Figure 4.2.19. (4.2.49) provides the numeric values for the simulation.

$L_x = 100 \times 10^{-6}\text{m};\quad L_y = 100 \times 10^{-6}\text{m}$

$L_{tri} = 95 \times 10^{-6}\ \text{m};\quad Z_x = 50 \times 10^{-6}\ \text{m};\quad Z_y = 50 \times 10^{-6}\ \text{m}$

$P_{amb} = 101325\ \text{Pa};\ P_c = 0\ \text{Pa};\quad \mu = 0.035\ \text{Pa.s};\quad U = 5.486\ \text{m/s}$

$n = 100;\quad m = 100$ (4.2.49)

In (4.2.49), L_{tri} is the side length of the equilateral triangle that causes the oil film distribution shown in Figure 4.2.17. Z_x is the x direction distance between the center of the equilateral triangle and the side of the square cell. Z_y is the y direction distance.

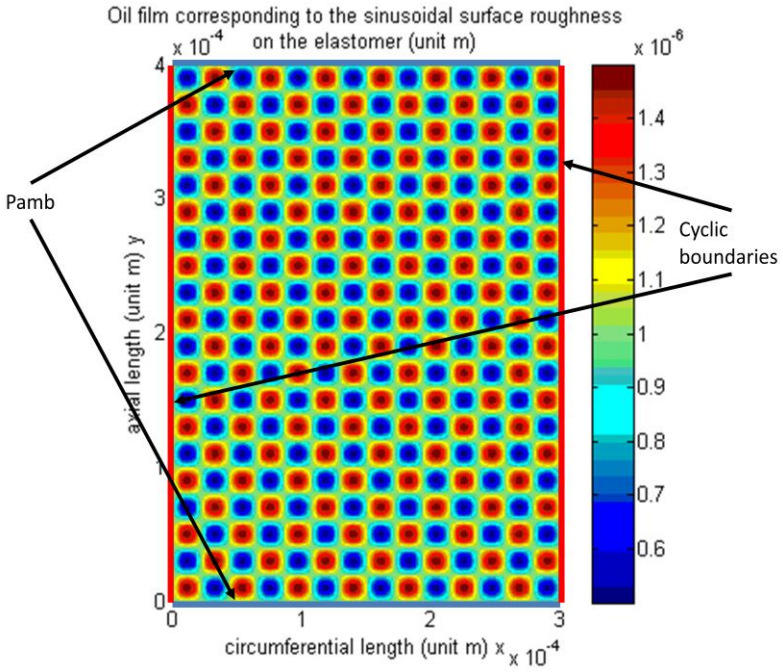

Figure 4.2.14 Oil film thickness distribution due to the sinusoidal surface roughness on the elastomer (unit m)

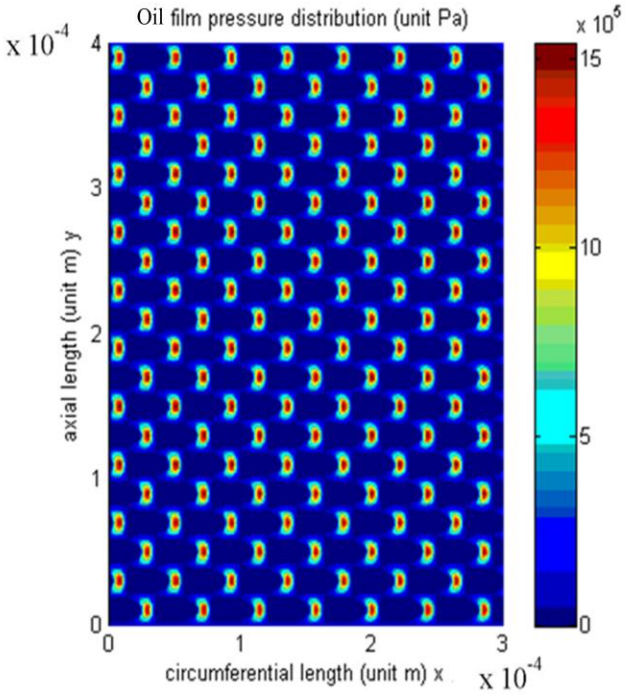

Figure 4.2.15 Oil film pressure distribution corresponding to the oil film in Figure 4.2.14 (unit Pa)

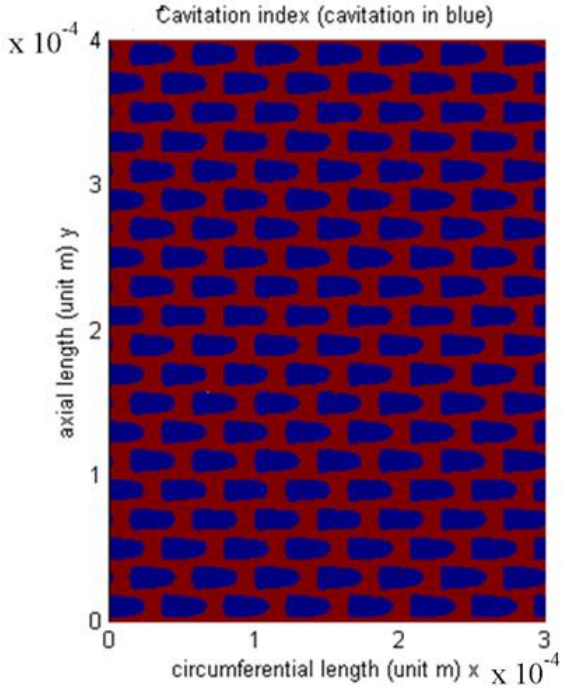

Figure 4.2.16 Inter-asperity cavitation index corresponding to the oil film pressure distribution in Figure 4.2.15

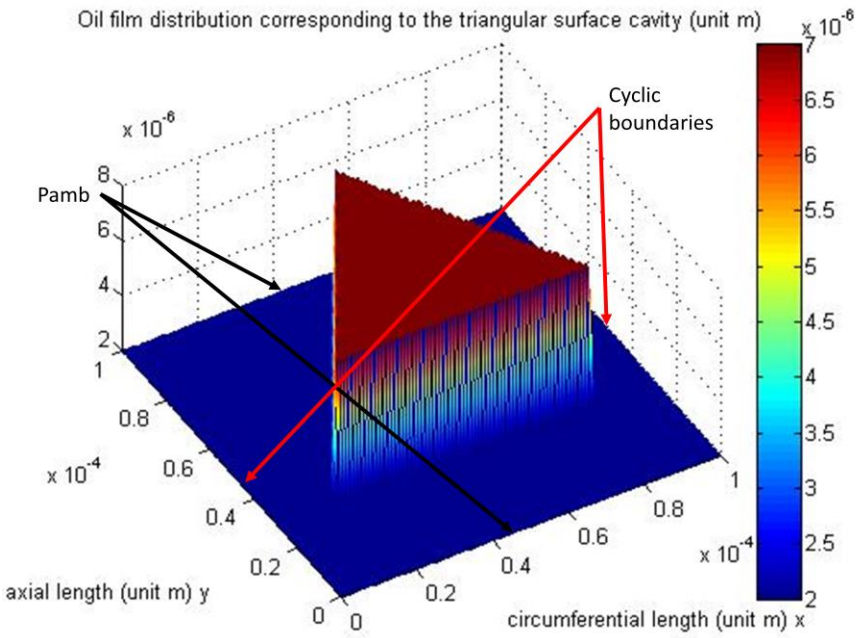

Figure 4.2.17 Oil film thickness distribution over a triangular surface cavity (unit m)

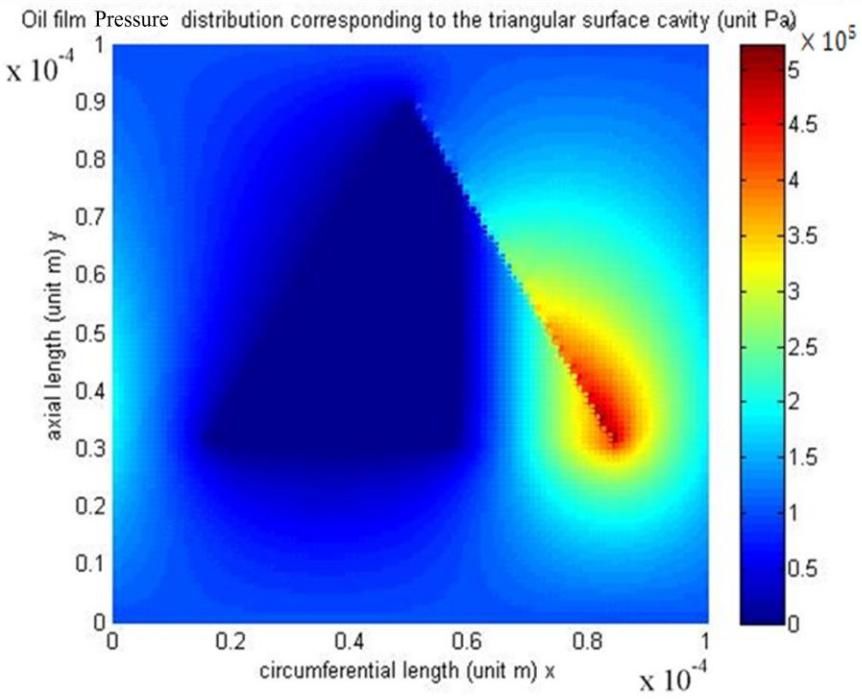

Figure 4.2.18 Oil Pressure distribution corresponding to the oil film thickness distribution shown in Figure 4.2.17 (unit pa)

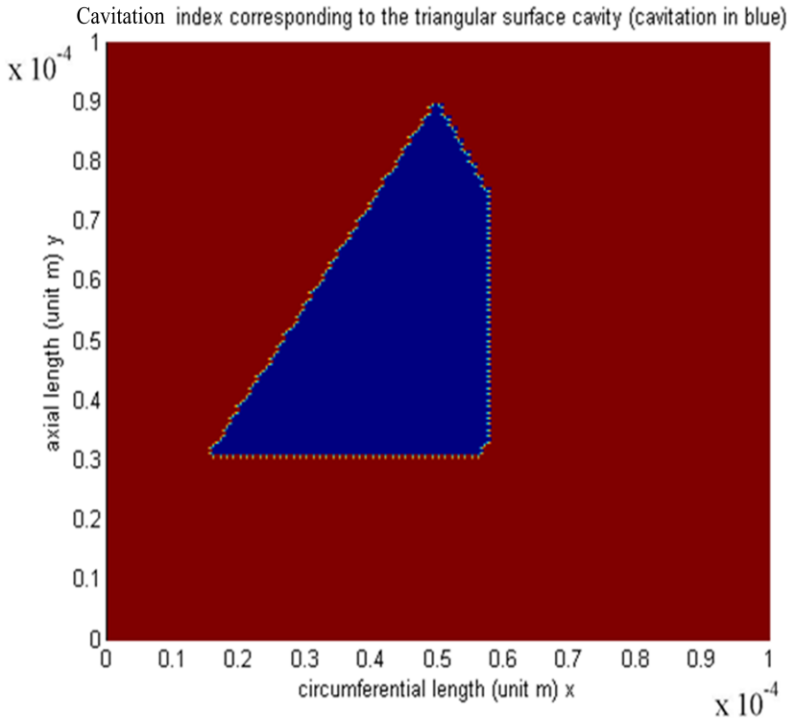

Figure 4.2.19 Cavitation index corresponding to the oil pressure distribution shown in Figure 4.2.18

After the oil film pressure distribution is determined, some important quantities of interest can be calculated. The viscous shear force of the fluid flow at any oil layer in the z direction (see Figure 4.1.1) can be calculated as:

$$\tau = \mu \frac{\partial u}{\partial z} \tag{4.2.49}$$

substituting (4.1.21) into (4.2.49) obtained:

$$\tau = \mu \left[\frac{1}{2\mu} \frac{\partial P}{\partial x} (2z - h) - \frac{U}{h} \right] \tag{4.2.50}$$

At the shaft boundary where $z = 0$

$$\tau_{shaft} = -\frac{1}{2}\frac{\partial P}{\partial x}h - \mu\frac{U}{h} \tag{4.2.51}$$

In equation (4.2.51) the viscous shear force is negative and tends to impede the rotating of the shaft. At the fluid elastomer boundary where $z = h$

$$\tau = \frac{1}{2}\frac{\partial P}{\partial x}h - \mu\frac{U}{h} \tag{4.2.52}$$

The viscous shear force tends to deform the elastomer, which means the shear force is the motivating force. The sign of the shear force should be inversed as:

$$\tau_{elastomer} = -\frac{1}{2}\frac{\partial P}{\partial x}h + \mu\frac{U}{h} \tag{4.2.53}$$

The pumping rate across the sealing zone can be calculated with equation

$$Q_y = \int_0^{L_x} q_y \, dx \tag{4.2.54}$$

Plugging equation (4.1.24) into equation (4.2.54) yields:

$$Q_y = \int_0^{L_x} -\frac{h^3}{12\mu}\frac{\partial p}{\partial y}dx \qquad \text{unit: } m^3/s \tag{4.2.55}$$

Q_y is the axial y direction pumping rate over the computational domain. Since periodicity is assumed in the circumferential x direction. The pumping rate over the entire circumference can be calculated as:

$$Q_y^{total} = \frac{Q_y \pi D}{L_y} \tag{4.2.56}$$

Where D is the outer diameter of the shaft.

The load carrying capacity over the computational domain can be calculated

$$W_c = \iint_0^{L_x \times L_y} P_g dxdy \tag{4.2.57}$$

Where P_g is the gauged fluid pressure over the computational domain. The load carrying capacity over the entire circumference can be calculated as:

$$W_{total} = \frac{W_c \pi D}{L_y} \tag{4.2.58}$$

4.3 Comparison to Navier-Stokes equation

It has been shown in section 4.2 that Reynolds equation considering JFO cavitation condition is used in this study to calculate the oil film pressure because it is believed that: for the thin oil film lubrication problem, the viscous shearing force dominates the system and the inertia force is negligible. However, a lot of research work, like [94] and [95], points out that the convective inertia has a considerable influence to the fluid pressure especially when the mating surfaces have surface textures on them.

If we check equation (4.1.11), we will find that the ratio of the fluid inertia term $\left(\bar{u}\frac{\partial\bar{v}}{\partial\bar{x}}+\frac{L_x}{L_y}\bar{v}\frac{\partial\bar{v}}{\partial\bar{y}}+\bar{w}\frac{\partial\bar{v}}{\partial\bar{z}}\right)$ on the left hand side to the dominating viscous term $\frac{\partial^2\bar{v}}{\partial\bar{z}^2}$ on the right hand side is defined as the reduced Reynolds number:

$$Re^* = \frac{\rho U h^2}{\mu L_x} \tag{4.3.1}$$

Usually the reduced Reynolds number Re^* is very small because the nominal oil film thickness h is far smaller than the characteristic length L_x in the sliding direction. As the reduced Reynolds number Re^* increases, the dominance of the viscous force term is weakened. Under three extreme cases the dominance of the viscous force might be seriously weakened or replaced: 1) The system has an extreme high sliding speed U; 2) The viscosity μ of the lubricant is extreme small; 3) the ratio between h and L_x become very large. In these three scenarios, the laminar lubricant flow might become turbulent flow and the Reynolds equation will be invalid.

The first two scenarios are easy to understand because they are caused by the independent parameters of the system. The third scenario is related to two parameters and is not straight forward. The surface texturing is one of the possible reasons for the third scenario. As shown in figure 4.3.1 the local nominal oil film thickness increases from h_1 to h_2 because of the triangular surface cavity with the step height of d. In such case the inertia effect of the fluid might have a big influence on the fluid pressure distribution around the surface cavity. And considerable error might be caused if Reynolds equation is used to predict the fluid pressure.

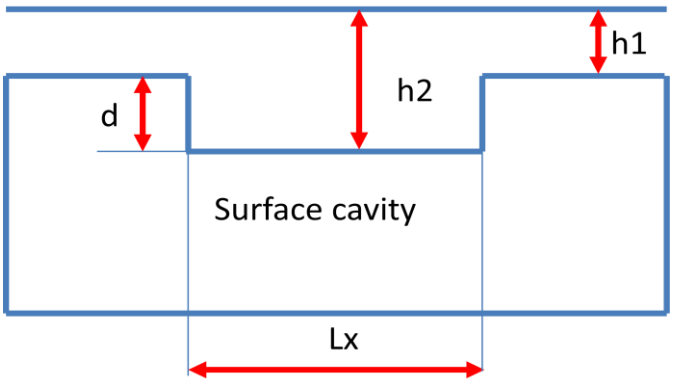

Figure 4.3.1 Increase of the nominal oil film thickness due to the surface cavity

Alex de Kraker et al. [96] used both the Reynolds equation and the Navier-Stokes equations to study the lubricant flow over a single surface dimple as shown in figure 4.3.2 and made a comparison between the two results. h_0 is the nominal oil film thickness in the non-textured area, d_p is the maximum depth of the surface dimple. They found that as the ratio $\frac{h_0}{d_p}$ decreases from 10 to 0.01, the pressure distribution predicted by the Reynolds equation becomes closer and closer to the solution from the

Navier-Stokes equations. It is also found that the Reynolds equation tends to under-estimate the fluid pressure when compared to the Navier-Stokes equations.

In this study the ratio $\frac{h_1}{d}$ (see figure 4.3.1) for the triangular cavity is around 0.2 which is quite close to the upper right case drawn in figure 4.3.3 ($\frac{h_0}{d_p} = 0.1$). One can see the error caused by the Reynolds equation is minor.

A similar validation work for using the Reynolds equation was also done by [97] and [98]. Etsion et al. [97] concluded that the error of the Reynolds equation is negligible for a single surface dimple as shown in figure 4.3.2, if the clearance is 3% or less of the dimple diameter. Even if the 3% limit is exceeded, the Reynolds equation is still safe to use because the Reynolds equation tends to under-estimate the load capacity which is consistent with the conclusion of [96].

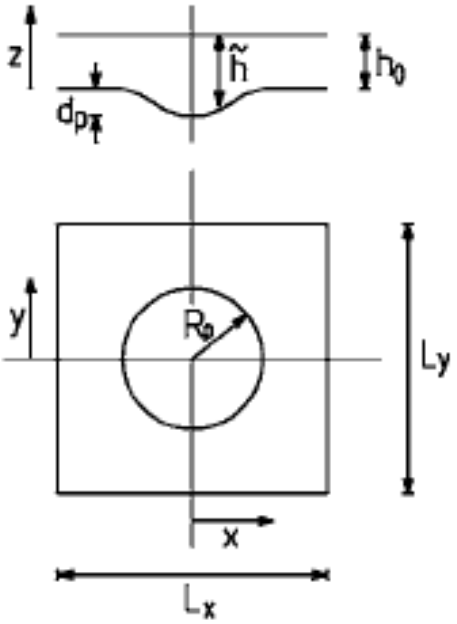

Figure 4.3.2 A single surface dimple (from [96] Kraker)

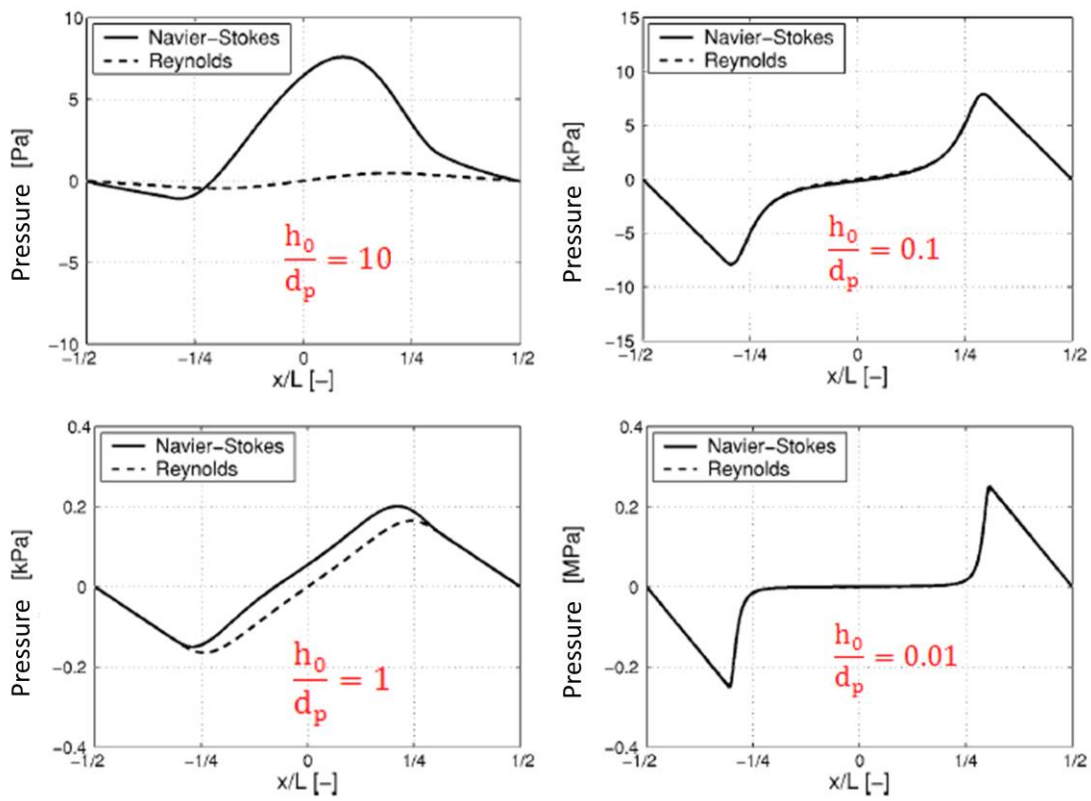

Figure 4.3.3 Fluid pressure distribution over the surface dimple shown in figure 4.3.2 (pure shear flow $U = 1m/s$) (from [96])

Dobrica and Fillon [98] studied a two dimensional square dimple as shown in Fig 4.3.4. In the conclusion of [98] they emphasized that special attention should be paid to the aspect ratio $\lambda = \frac{l_D}{h_D}$ (see figure 4.3.4), and the Reynolds number Re defined in equation (4.3.2). A too small λ indicates the basic assumption for the Reynolds equation, small variation in oil film thickness compared to the feature length, is violated. A too large Re indicates the dominance of the viscous force is no longer valid. In both cases, Reynolds equation becomes inaccurate. Actually if we note the relationship between Re and Re^* as shown in equation (4.3.3), we can find that the two validation criterion given by [98] can be generalized as Re^* criteria. Because either a very large

Re or a vary small λ (an equivalent reciprocal of $\frac{h}{L_x}$) will lead to a very large Re^*.

In this study the cavity or asperity depth $d = 5\ \mu m$ and the feature length (side length of the surface triangle) is $L_x = 95\ \mu m$, resulting in a aspect ratio of $\lambda = \frac{L_x}{d} = 19$. The Reynolds number is calculated using equation (4.3.2) as about $0.825 \sim 0.9625$

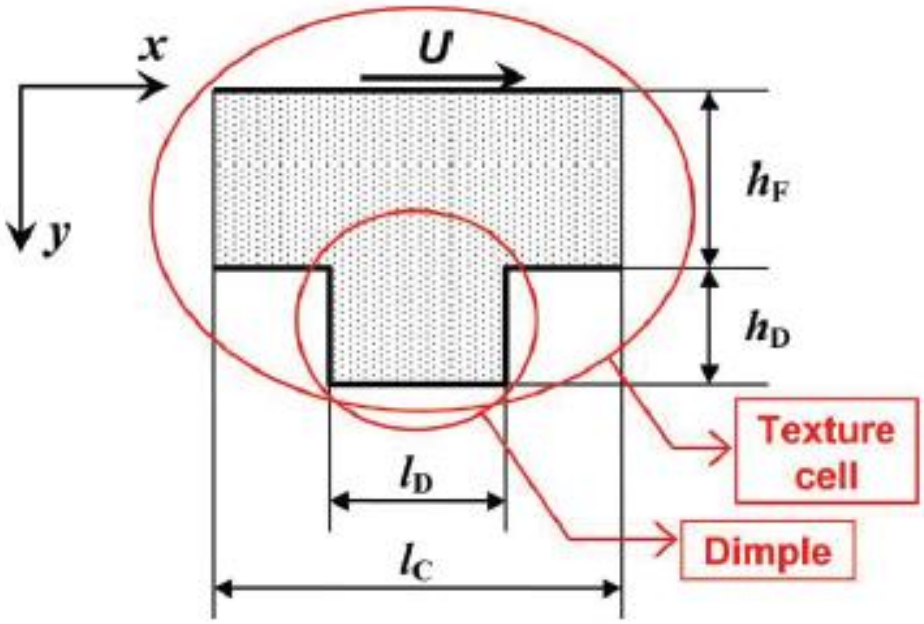

Figure 4.3.4 Elementary texture cell (from [98])

$$Re = \frac{\rho U h}{\mu} \tag{4.3.2}$$

$$Re^* = Re\frac{h}{L_x} \tag{4.3.3}$$

By checking the non-dimensional pressure distribution comparison between the Reynolds solution and the Navier-Stokes solution (see figure 4.3.5), one can find that the error

generated by the Reynolds equation with the aspect ratio 16 and the Reynolds number 4 is still minor. So the Reynolds equation is acceptable for this study, with the aspect ratio of 19 and the Reynolds number of $0.825 \sim 0.9625$. Note that no cavitation is included in these validation works.

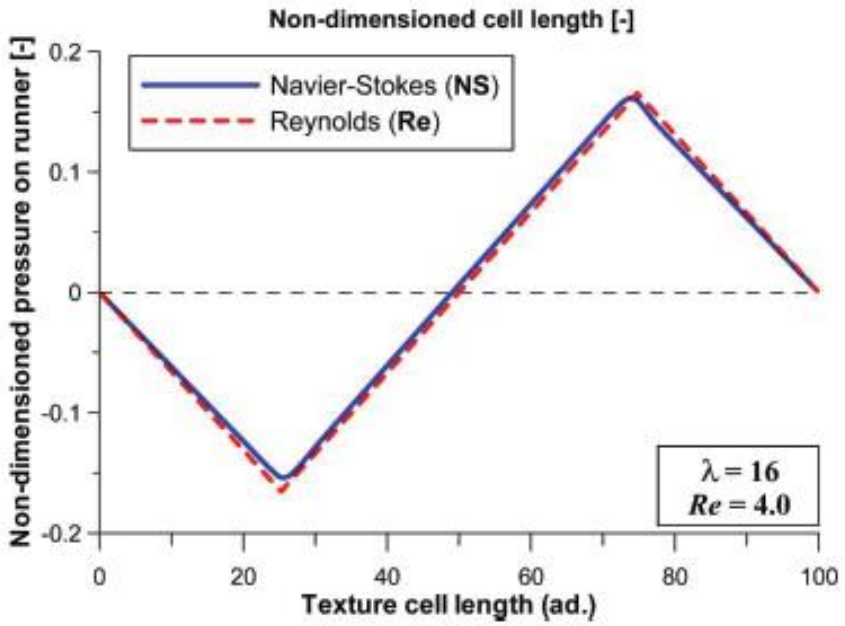

Figure 4.3.5 Pressure comparison between the Reynolds solution and the Navier-Stokes solution ($\lambda = 16$ and $\mathrm{Re} = 4.0$) (from [98])

Though the validation studies generally demonstrates that Reynolds equation is valid for the shallow surface textures (with a large aspect ratio λ), the inertia force of the fluid in the lubrication problem still draws more and more attention nowadays. This is because the high performance computer becomes more easily reachable than before, allowing the application of more complicated numerical models. This is also because under some extreme cases the influence of the inertia effect is significant. The inertia effect is

included into the fluid calculation through two major different ways.

The first way is to use a modified Reynolds equation like reference [96] and [99]. A. de Kraker et al. [96] proposed using a multi-scale algorithm to correct the theoretical error of the Reynolds equation. Since the fluid inertia has a great influence around the tiny surface dimple, a full CFD analysis is conducted around the surface dimple area (small scale) to get an accurate fluid pressure distribution considering the fluid inertia. A large scale analysis employing the Reynolds equation is conducted for the entire bearing area. The influence of the small scale calculation is incorporated into the large scale calculation by matching the flow rate of the two calculations (modifying the flow factor of the Reynolds equation). This method is similar to the statistical model of Patir and Cheng [45-46]. The difference is: in [45-46] Reynolds equation is used for both the small scale calculation and the large scale calculation and the flow factor of the large scale Reynolds calculation is modified to account for the influence of the quasi-random surface roughness but not for the inertia of the fluid. A. de Kraker et al. [96] also considered the cavitation. The half-Sommerfeld and the Reynolds cavitation conditions are employed for the large scale Reynolds equation. A mass conservative cavitation condition proposed by Brajdic et al. [100] is used for the small scale CFD calculation. This cavitation condition is a simplified one which assumes the fluid density is a dependent variable of the fluid pressure. Cavitation condition mentioned in [100] originates from references [101] and [102]. Gao and Hewson [99] developed a similar 2-D Multi-scale algorithm for the EHL analysis.

The second way of considering the inertia effect is the full CFD analysis. Navier-Stokes equations are used for the calculation over the entire solution domain. Full CFD calculation is more accurate than the multi-scale method, but is also more expensive. Yoshimoto et al. applied the CFD calculation to a thrust bearing [103]. Khonsari et al. [104] used the CFD to simulate the flow field around the rings of mechanical seals. Billy et al. [105] used CFD to analyze the flow over a 2-D rectangular dimple with a very large Reynolds number (Turbulent flow regime). The above CFD analyses have not considered the cavitation.

Brajdic et al. [100] studied a low friction pocketed pad bearing with CFD and considered about the cavitation which has been introduced previously. Hartinger et al. [106] and Almqvist et al. [107] did thermal CFD modeling works for the elastohydrodynamic line contact problem. These studies employed a cavitation model which originates from the Weller cavitation model and is modified to incorporate the nonlinear density-pressure relationship of Dowson and Higginson [108].

The CFD model with cavitation for the lubrication problem is still under development stage. This section only gives a brief introduction about the directions worth further study. Also by comparing the Reynolds solution to the CFD solution, the validation for using the Reynolds equation in this study is enhance

CHAPTER 5 NUMERICAL RESULT AND ITS BENCHMARKING TO THE EXPERIMENTAL RESULT

5.1 Experiment

The experiment is intended for verifying the idea that the deterministic surface roughness made on the shaft could manipulate the pumping direction of the lip seal.

Experiment setup：

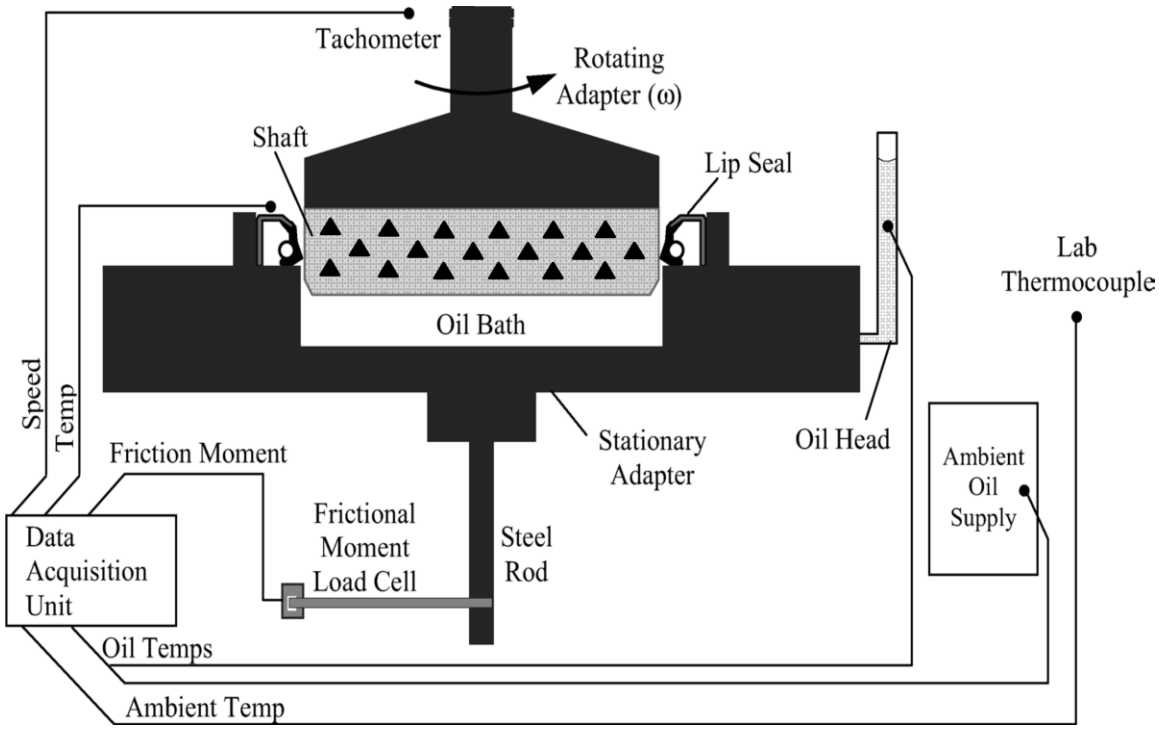

Figure 5.1.1 Experiment system setup (from Warren [83])

The experimental testing of the shafts with staggered surface triangles is conducted with a tribo-meter as shown in Figure 5.1.1. The surface triangles on the shaft drawn in Figure 5.1.1 are much larger than their actual size for the clarity of the demonstration. Photos of the shaft surface with staggered surface triangles oriented at different directions are given in Figure 5.1.2. The actual geometry and the staggered arrangement of the surface triangles are given in Figure 5.1.3. The surface triangles are made of nickel by a modified LIGA process (lithography, molding and electroplating) and have isosceles geometry. The outer diameter of the shaft shown in Figure 5.1.1 is $D = 139.7\ \text{mm}$ not including the nickel layer. The lip seal used in the experiment is a conventional lip seal with a total radial sealing load of $70\ \text{N}$ $(13.5\ \text{oz/circumferential inch})$. According to the experiment measurement, the total sealing load decreases to about $60\ \text{N}$ $(11.5\ \text{oz/}$ $\text{circumferential inch})$ after the "break in" stage when the lip seal runs against smooth shaft.

The oil drop test, suggested by Horve [2] is used to figure out the directional pumping ability of these surface triangles on the shaft. Figure 5.1.4 demonstrates the process for the oil drop test. A certain amount of oil is injected into the sealing zone, and the time spent for the oil to be pumped out of the sealing zone is measured. The pumping rate is obtained by dividing the quantity of the oil injected by the length of the pumping time. The pumping direction can be distinguished through the oil head. The oil head is connected to the oil collecting chamber (oil bath). A rising oil level in the oil head means the oil is reversely pumped into the oil reservoir (oil bath) while a dropping oil level

means the oil is spilt out of the oil reservoir and leakage is happening. The experiment is a real life test of the lip seal, and lasts several days for each surface triangle pattern. The measurement of the pumping rate started after the temperature of the testing system becomes stable which means equilibrium is reached and the “break in” stage ends.

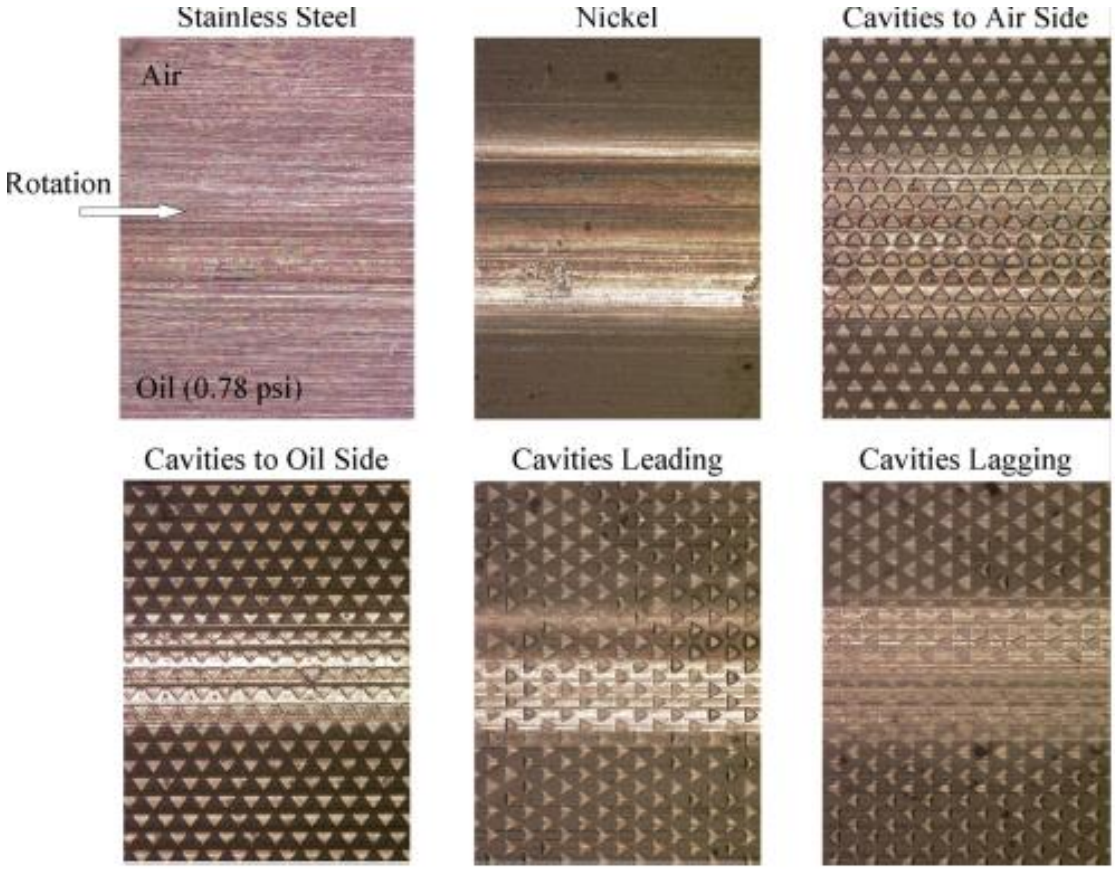

Figure 5.1.2 Triangular surface cavities made on the shaft (from Warren [83])

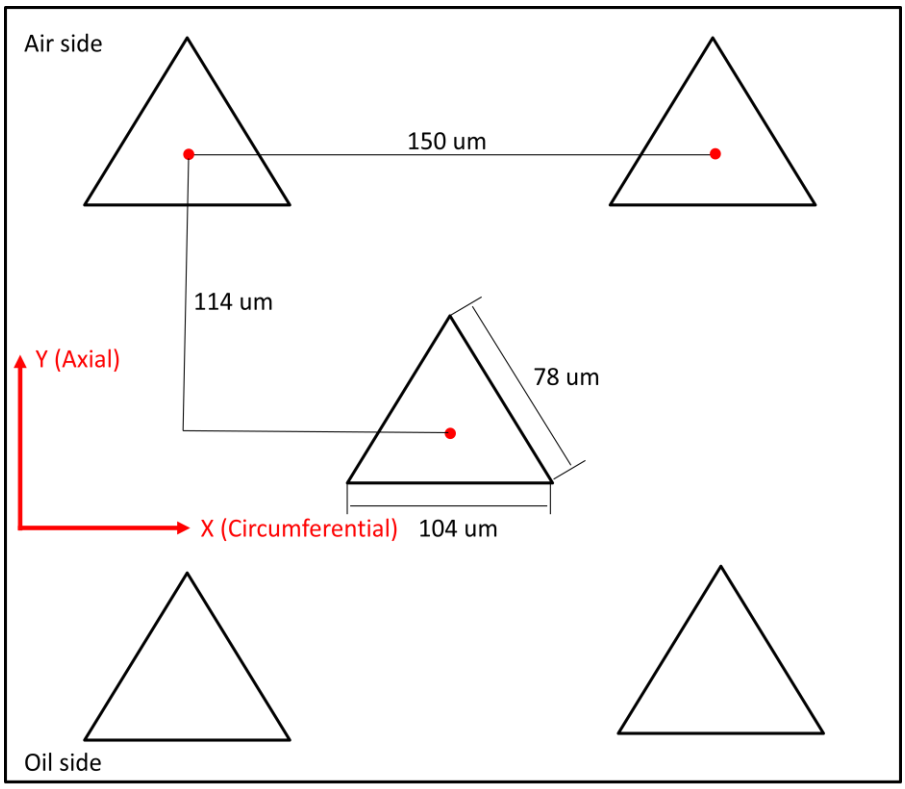

Figure 5.1.3 Size and the staggered arrangement of the surface triangles

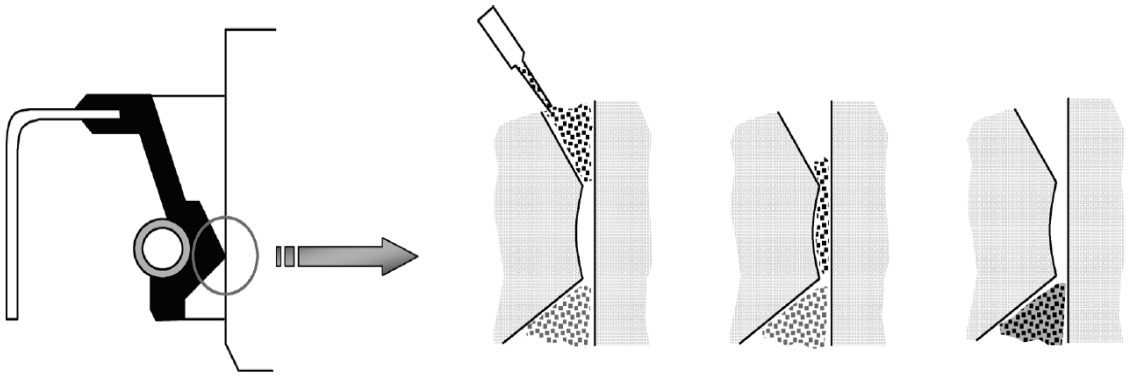

Figure 5.1.4 Demonstration of oil drop test from [109]

Lubricant:

Oil Type: New SAE20W50

Density: $867.54 - 875.00\ \mathrm{Kg/m^3}$ $(7.24 - 7.33\ \mathrm{lbs/gal})$

Cavitation threshold pressure P_c: 0 Pa from reference [7]

Viscosity versus temperature: (Shown in Figure 5.1.5)

$75\ ^{\circ}\mathrm{C}$ is observed to be the temperature at which the system reaches the equilibrium after 20-40 hours of "break in". As shown in Figure 5.1.5 the viscosity at $75\ ^{\circ}\mathrm{C}$ is $0.035\ \mathrm{Pa \cdot s}$. Thus $0.035\ \mathrm{Pa \cdot s}$ is used as the primary input for the numerical study.

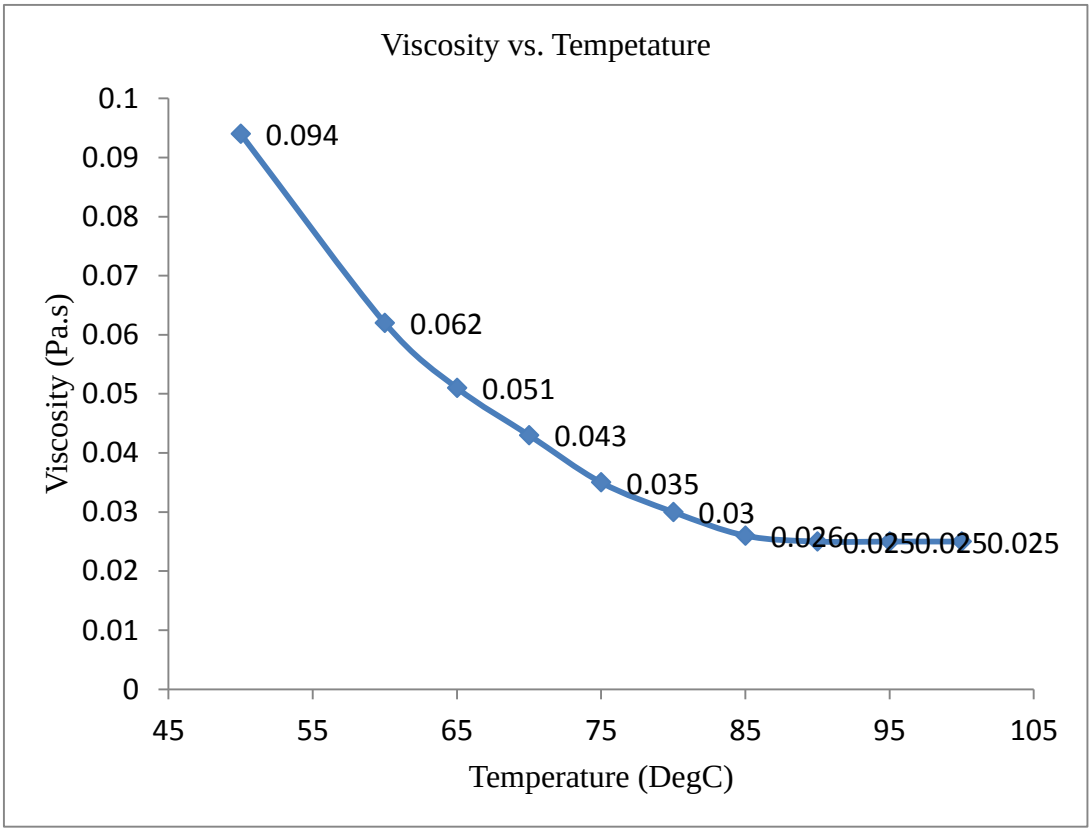

Figure 5.1.5 Viscosity of the lubricant vs. temperature

Experiment result:

In the experiment, the surface triangles are distinguished as the triangular cavity and the triangular asperity as shown in Figure 5.1.6 (a) and (b), respectively. The orientations of the surface triangles are distinguished by the rotation angle θ as shown in Figure 5.1.7. Four orientations, to the air side, to the oil side, leading and lagging, are tested in the experiment as shown in Figure 5.1.2. These four orientations are of the rotation angle $90^{\circ}, 30^{\circ}, 0^{\circ}$ and 60° as shown in Figure 5.1.7.

The pumping rate for the staggered triangular surface cavities and the staggered triangular surface asperities are shown in Figure 5.1.8 and Figure 5.1.9, respectively. The sign convention is that the positive pumping rate means forward pumping (leakage) and the negative pumping rate means reverse pumping. The testing for the same surface texture pattern is repeated for several times. The pumping rate reported in this study is an average value. The experimental results show that the directional pumping ability of the surface triangles are quite obvious as compared to the pumping ability of the smooth shaft and the nickel plated smooth shaft as shown in Figure 5.1.8. In Figure 5.1.8 the small reverse pumping rate for the lip seal running against the smooth shaft or the nickel plated smooth shaft could be explained by the theory of Kammüller [30] and Müller [31] which has been introduced in detail in section 2.1. The pumping rate for the smooth shaft also minimizes the possibility of the misalignment. Because if there is serious misalignment due to the incorrect installation of the lip seal, a larger reverse pumping rate should be observed, which is also introduced in details in section 2.1. For all the reverse

pumping cases, the oil injected into the sealing zone is quickly pumped out resulting in the starvation of the sealing zone. For this reason, the tip of the elastomer is worn off and the sealing zone width (see Figure 3.3.3) increases over time. The starvation of the sealing zone also leads to the abrasion (wear track) of the shaft triangles after days of testing as shown in Figure 5.1.2.

The general conclusion from Figure 5.1.8 and Figure 5.1.9 is that the staggered triangular cavities tend to pump oil toward their base while the staggered triangular asperities tend to pump oil toward their apex. That is to say when the triangular cavities point to the oil side, they will pump the oil to the air side creating leakage; when the triangular cavities point to the air side, they will reversely pump the oil back into the oil bath tank. The situations for the staggered triangular asperities are just opposite. Also it is observed that the triangular asperities pump much more oil than the triangular cavities.

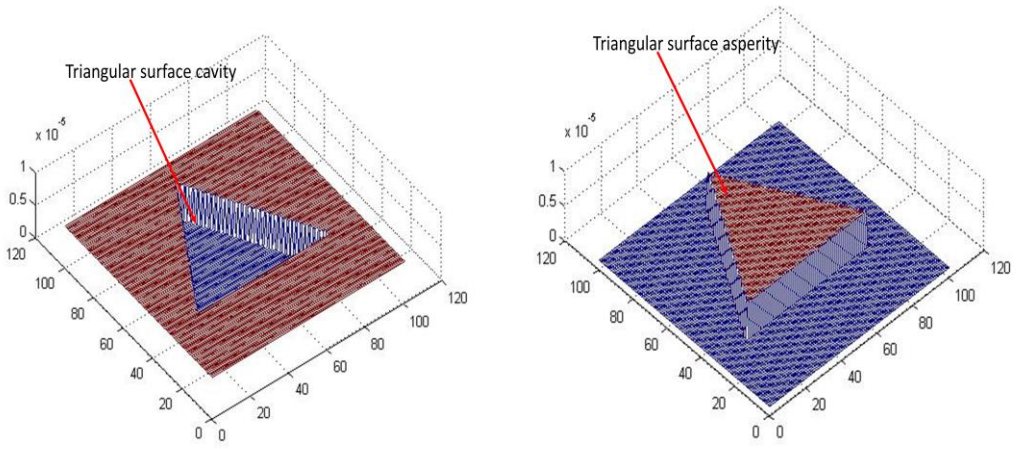

(a) (b)

Figure 5.1.6 Triangular surface cavity (a) and asperity (b)

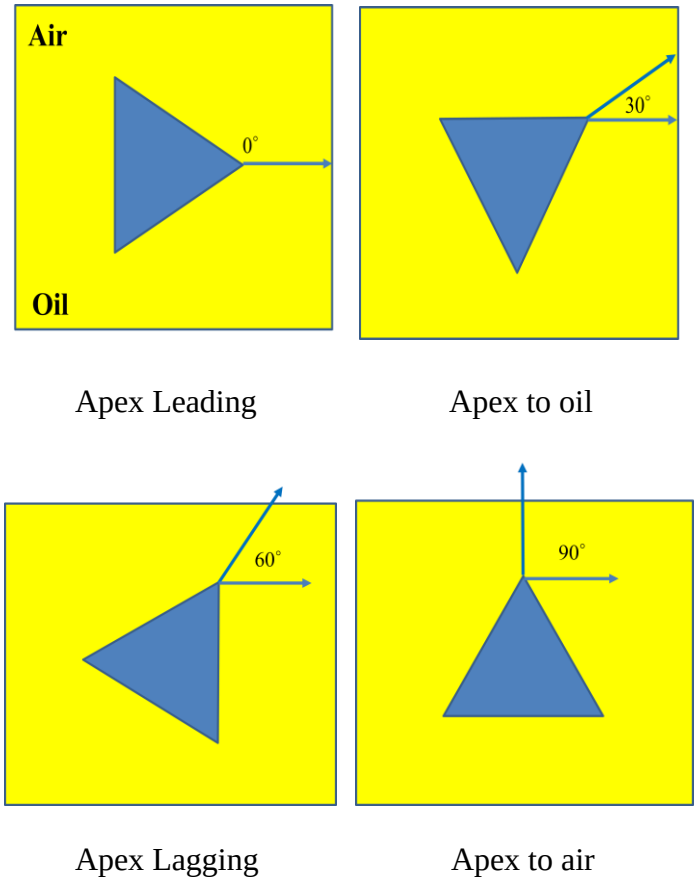

Apex Leading Apex to oil

Apex Lagging Apex to air

Figure 5.1.7 Rotation angle of the equilateral surface triangle

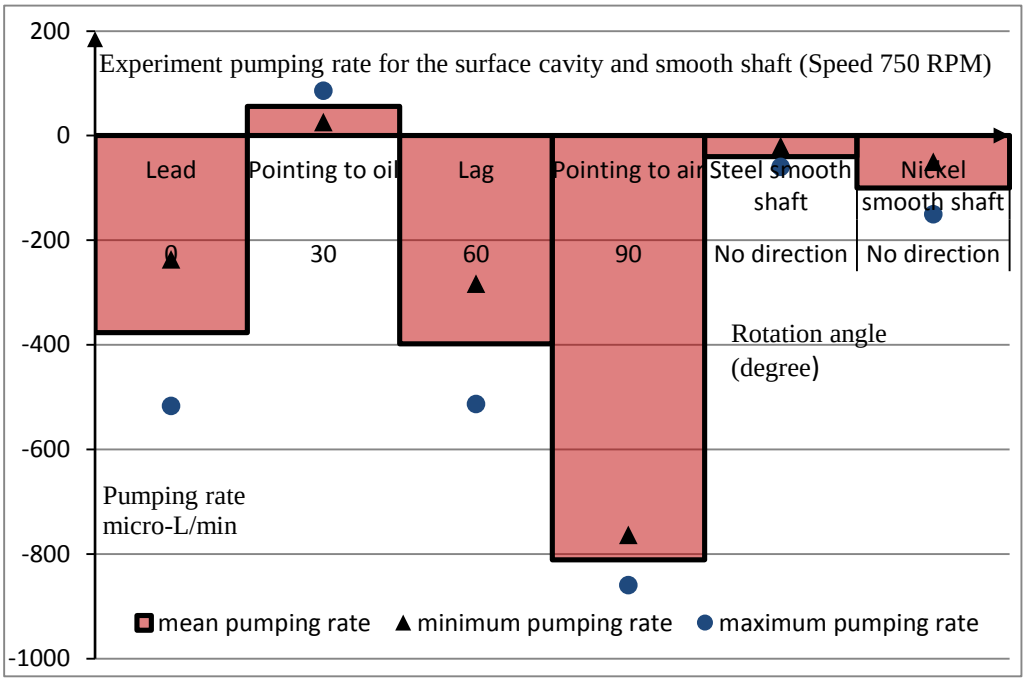

Figure 5.1.8 Pumping rate for the staggered triangular cavities and the smooth shaft (Experiment)

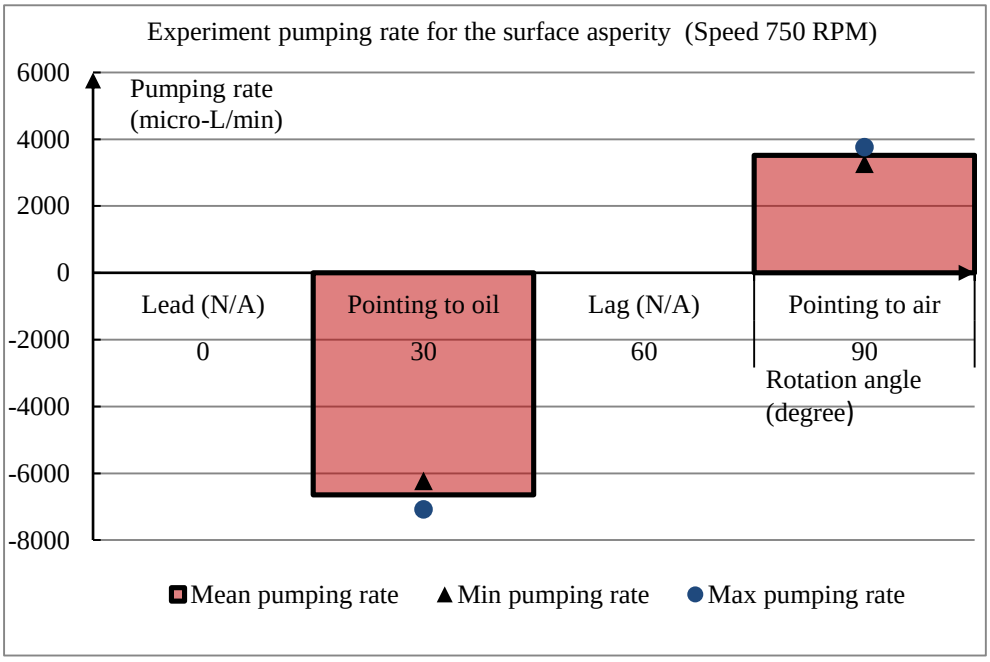

Figure 5.1.9 Pumping rate for the staggered triangular asperities (Experiment)

5.2 Numerical Study on a Single Surface Triangle

The numerical study is conducted step by step starting from a single surface triangle cell. The difference between the triangular cavity and the triangular asperity as well as the orientation of the surface triangles are defined in section 5.1. (see 5.1.6 and 5.1.7). To benefit the angle rotation test in the numerical study, equilateral triangles with a side length of $L_{tri} = 96.5\ \mu m$ are used to replace the isosceles triangles since the equilateral triangle has only twelve variations as the triangle rotates 10° each time as shown in Figure 5.1.7. The geometry difference between the equilateral triangle and the isosceles triangle is minor.

Ideally both the cavity and the asperity are stepping variation of the surface topology and have sharp (vertical) edges on the triangle's boundaries, neglecting the manufacturing tolerance. Numerically, infinite grid density is needed to approximate the step function, which is not possible. In this study, a minimum grid spacing of $1\ \mu m$ and a maximum grid spacing of $4\ \mu m$ are used to approximate the stepping surface triangles. A clear converging trend is observed for the pumping rate and the load carrying capacity as the grid density increases. The convergence test shows that the higher the pumping rate is, the smaller the grid effect is. This means a strong hydrodynamic effect of the lubricant can be well captured by the grid function.

In this study, all the fluid dynamics calculations employ the steady state Reynolds equation (4.2.10) neglecting the squeeze oil film effect of the shaft triangles. The reason for this treatment has been discussed in section 4.1. Both the pumping rate and the load

carrying capacity are evaluated over the entire circumference using equation (4.2.56) and (4.2.58). The sign convention in the numerical study is consistent with the experiment that a positive pumping rate means leakage while a negative pumping rate means a reverse pumping.

Numerical parameters for the system:

L_x computational length in the circumferental (x) direction (unit m)

L_y computational length in the axial (y) direction (unit m)

m grid number in the circumferential (x) direction

n grid number in the axial (y) direction

U sliding speed of the shaft (unit m/s)

μ dynamic viscosity of the lubricant (unit $Pa \cdot s$)

P_c threshold pressure for the cavitation to form (unit Pa)

P_{b1} Axial boudary pressure at $y = 0$ oil side (unit Pa)

P_{b2} Axial boudary pressure at $y = L_y$ air side (unit Pa)

dcav step hieght of the surface cavity (unit m)

dasp step hieght of the surface asperity (unit m)

θ Pointing angle of the surface triangles defined in Figure 5.1.7 (unit degree)

h_{ntri} Assumed oil film thickness over the area without surface triangles (unit m)

L_{tri} Side length of the equilateral surface triangle

See Figure 5.2.1 for more information

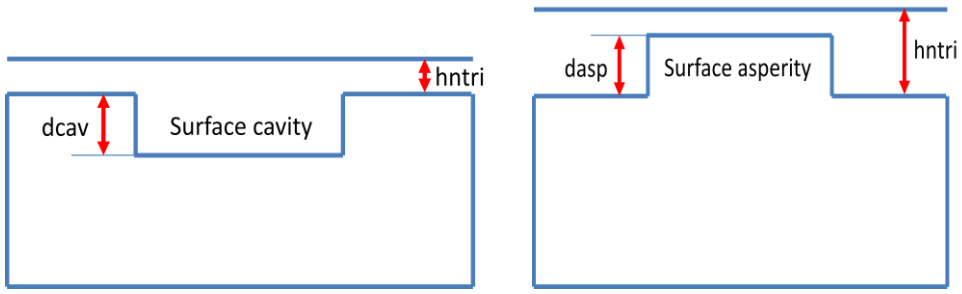

(a) (b)

Figure 5.2.1 Assumed gap between the elastomer and the shaft cavity (a) and the shaft asperity (b)

Case 1: (Angle rotation test for a single triangular cavity with hntri=1um)

Pattern: single equilateral triangular cavity (see Figure 5.1.6 (a));

$h_{ntri} = 1\ \mu m;\ dcav = 5\ \mu m;\ U = 5.486\ m/s$ (750 RPM); $\mu = 0.035\ Pa \cdot s;\ P_c = 0\ Pa;$ $P_{b1} = P_{b2} = 101325\ Pa;\quad \theta = 0^{\circ} \sim 110^{\circ},\ 10^{\circ}$ each rotation; $L_x = 100\ \mu m;\ L_y = 100\ \mu m;\ L_{tri} = 96.5\ \mu m;\ m = 101\ ;\ n = 101$ (5.2.1)

Results and interpretation:

The pumping rate and the load carrying capacity for the entire circumference are given in Figure 5.2.2. Recall that the periodic boundary condition is prescribed in the circumferential x direction. Thus a single surface triangle actually represents a line of equally spaced triangle over the entire circumference. An assumed value h_{ntri} is used as the gap between the elastomer and the top surface of the triangular cavity as shown in Figure 5.2.1 (a). According to the previous experimental and numerical studies, for the conventional lip seal, it is observed that there exists a thin oil film of approximately

1 μm between the elastomer and the shaft face after the "break in" stage, caused by the hydrodynamic lifting force. Thus in this section, it is assumed that the elastomer is 1~2 μm above the surface cavity or asperity.

It is shown that a single triangular cavity tends to pump oil toward its base. As shown in Figure 5.2.4, the negative fluid pressure on the diverging side of the oil film is truncated by the vapor bubble predicted by the JFO theory, while the positive pressure peak on the converging side of the oil film drives fluid to both the base and the apex of the triangle. Because the oil film thickness over the triangular cavity area (6 μm) is much larger than the oil film thickness outside the triangular cavity area (1 μm), more oil is driven to toward the base of the triangle. The pumping rate vs. rotation angle plot shows that when the triangular cavity is pointing to the air side ($\theta = 90^{\circ}$ see Figure 5.1.7), the oil is reversely pumped toward the oil side. On the contrary, when the triangular cavity is pointing to the oil side ($\theta = 30^{\circ}$ see Figure 5.1.7), the oil is pumped to the air side.

The axial pumping rate in this study is quite small because of the excessive presence of the vapor bubble (cavitation). As introduced in Chapter 4, any pressure driven flow is cancelled inside the vapor bubble (cavitation area) while the axial pumping flow is purely a pressure driven flow. Consequently, the axial pumping flow is inhabited by the cavitation. The maximum equivalent load carrying capacity over the entire circumference of the lip seal is only 0.6 N which is far smaller than the sealing load of about 60 N. Thus, a single line of triangular cavities over the circumference cannot hold up an oil film of 1 μm between the elastomer and the shaft.

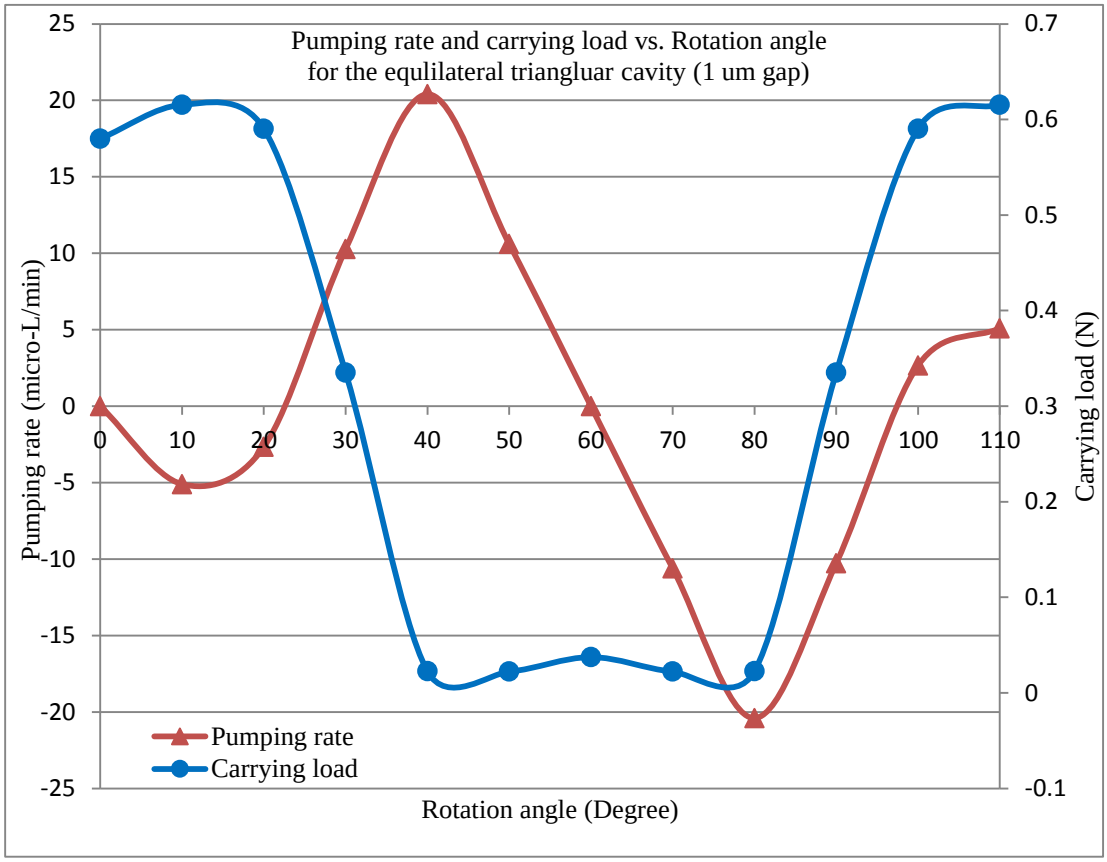

Figure 5.2.2 Angle rotation test for a single triangular surface cavity ($h_{ntri} = 1$ μm)

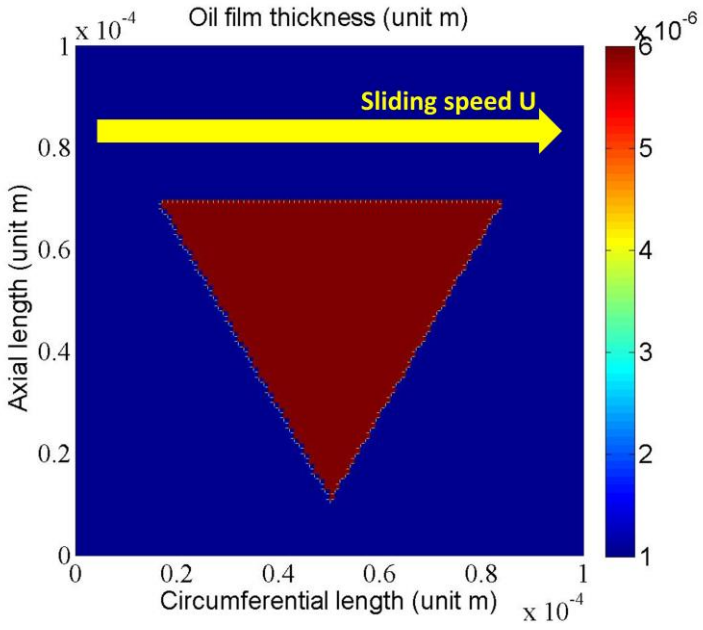

Figure 5.2.3 Oil film thickness over a single triangular cavity ($h_{ntri} = 1$ μm)

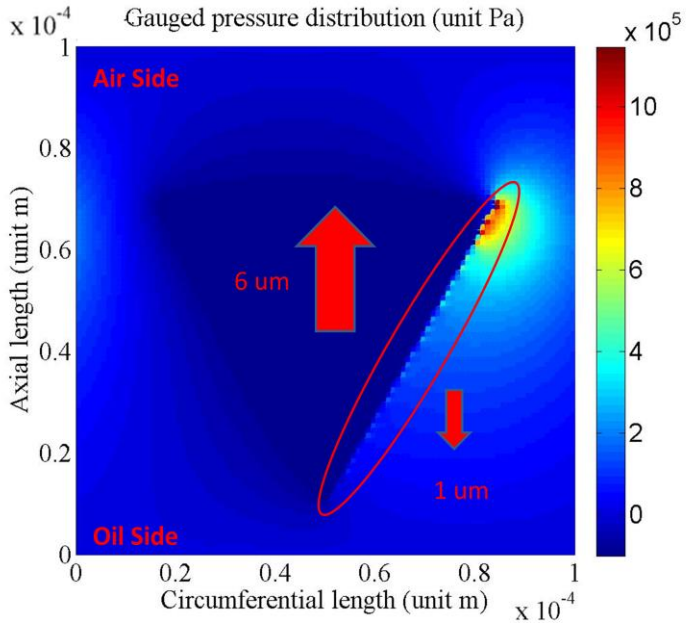

Figure 5.2.4 Gauged pressure distribution over a single triangular cavity ($h_{ntri} = 1$ μm)

Case 2: (Angle rotation test for a single triangular cavity with hntri=2um)

Pattern: single equilateral triangular cavity (see Figure 5.1.6 (a))

$h_{ntri} = 2$ μm; dcav $= 5$ μm; $U = 5.486$ m/s (750 RPM); $\mu = 0.035$ Pa · s; $P_c = 0$ Pa; $P_{b1} = P_{b2} = 101325$ Pa ; $\theta = 0^{\circ}\sim110^{\circ}$, 10° each rotation; $L_x = 100$ μm ; $L_y = 100$ μm; $L_{tri} = 96.5$ μm; $m = 101$; $n = 101$; (5.2.2)

Results and interpretation:

This case is similar to case 1 except that h_{ntri} increases from 1 μm to 2 μm. The pumping rate and the load carrying capacity over the entire circumference are given in Figure 5.2.5. The trend of Figure 5.2.5 is almost the same as Figure 5.2.2. Except that the pumping rate in Figure 5.2.5 is much larger than it is in Figure 5.2.2 while the load carrying capacity is smaller than it is in Figure 5.2.2.

The increased pumping rate is due to: 1) The larger gap between the shaft and the elastomer provides a larger pumping corridor as shown in Figure 5.2.1 (a), and the axial flow rate is proportional to the oil film thickness cubed, h^3, according to equation (4.2.55). 2) The vapor bubble is less prevalent because of a less intensive hydrodynamic effect due to the enlarged oil film thickness. Note that vapor bubble (cavitation) prevents any pressure driven flow including the axial pumping flow. The decreased load carrying capacity is also due to the less intensive hydrodynamic effect indicated by the decreased pressure gradient in Figure 5.2.7 compared to Figure 5.2.4.

Another phenomenon worth discussion is that as the rotation angle θ approaches 0° (Lead) and 60° (Lag) (see Figure 5.1.2 and Figure 5.1.7) the axial pumping rate is almost zero. This is because the equilateral triangle is geometrically symmetrical about the fluid incoming direction when $\theta = 0^\circ$ and 60° and an equal amount of oil is pumped toward both the oil side and the air side. Consequently there is almost no axial pumping preference when $\theta = 0^\circ$ and 60° compared to other orientations.

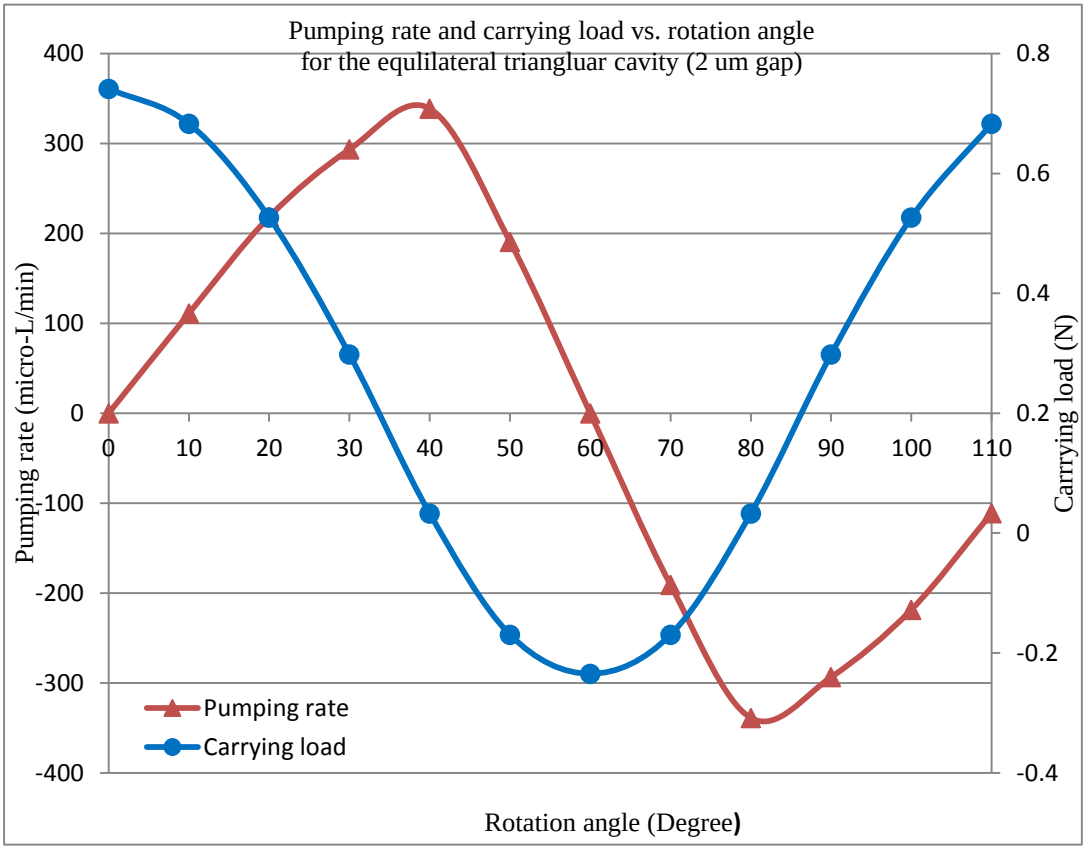

Figure 5.2.5 Angle rotation test for a single triangular surface cavity ($h_{ntri} = 2$ μm)

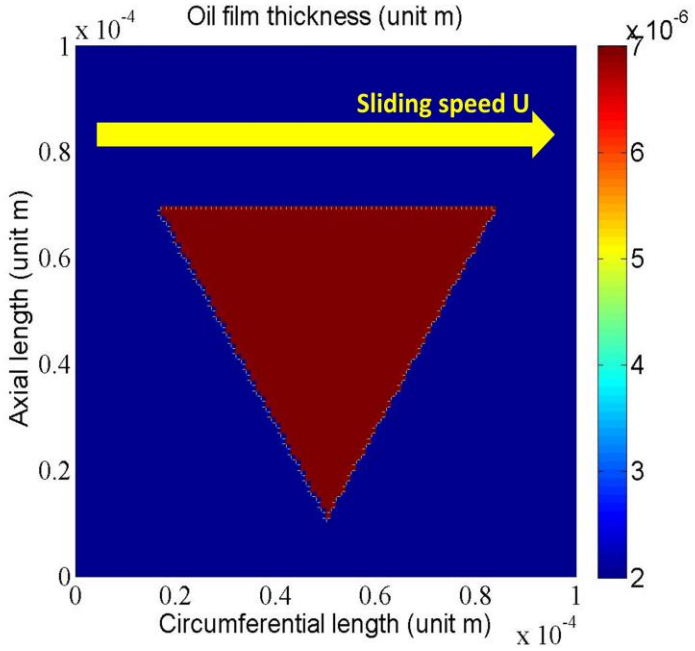

Figure 5.2.6 Oil film thickness over a single triangular cavity ($h_{ntri} = 2$ μm)

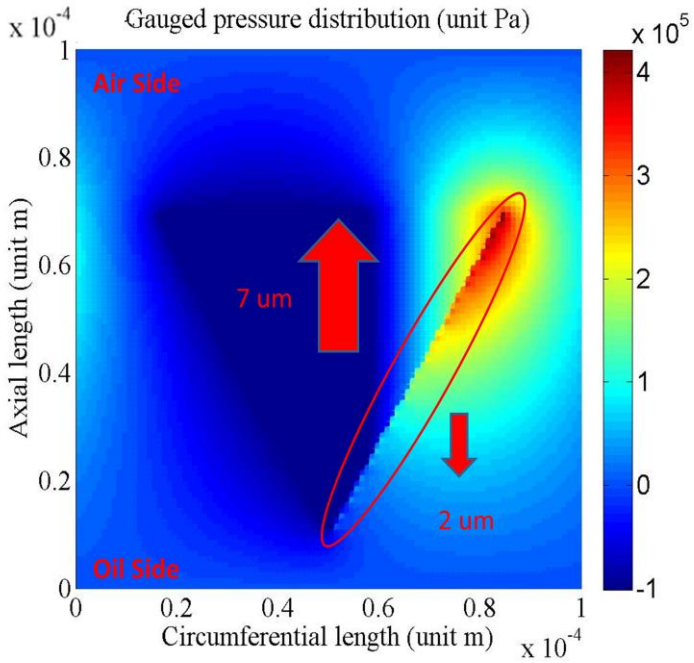

Figure 5.2.7 Gauged pressure distribution over a single triangular cavity ($h_{ntri} = 2$ μm)

Case 3: (Angle rotation test for a single triangular asperity with hntri=6um)

Pattern: single equilateral triangular asperity; (see Figure 5.1.6 (b))

$h_{ntri} = 6$ μm; dasp $= 5$ μm; $U = 5.486$ m/s (750 RPM); $\mu = 0.035$ Pa · s; $P_c = 0$ Pa; $P_{b1} = P_{b2} = 101325$ Pa ; $\theta = 0^{\circ}\sim110^{\circ}$, 10° each rotation; $L_x = 100$ μm ; $L_y = 100$ μm; $L_{tri} = 96.5$ μm; $m = 101$; $n = 101$ (5.2.3)

Results and interpretation:

The pumping rate and the load carrying capacity for the entire circumference are given in Figure 5.2.8. Two important features are found in Figure 5.2.8. 1) The triangular asperity tends to pump oil toward its apex which is almost completely opposite to the triangular cavity; 2) The triangular asperity pumps much more oil and provides much

larger load carrying capacity compared to the triangular cavity.

As shown in Figure 5.2.10, vapor bubble (cavitation) truncates the negative fluid pressure on one side of the triangular asperity. The single positive pressure peak on the other side of the triangular asperity drives the oil toward both the apex and the base. Because of the impedance caused by the asperity to the flow, more oil is directed toward the apex of the triangular asperity.

The triangular asperity pumps much more oil than the triangular cavity 1) because the hydrodynamic effect of the fluid around the surface asperity is more intensive than it is around the surface cavity. This can be proved simply by comparing the pressure distribution shown in Figure 5.2.10 to that shown in Figure 5.2.4. 2) In addition this is because the inter-asperity oil film thickness is much larger than the inter-cavity oil film thickness. In this case the inter-asperity oil film thickness is $h_{ntri} = 6\ \mu m$, while in case 1 the inter-cavity oil film thickness is only $h_{ntri} = 1\ \mu m$. The inter-asperity oil film works just like a huge pumping corridor.

Recalling that the axial pumping rate is proportional to the oil film thickness cubed, h^3, as given in equation (4.2.55), it is not surprising to see that the triangular cavity has an axial pumping rate of only several hundred micro-liters per minute while the triangular asperity could pump almost ten thousand micro-liters per minute. This numerical result matches the experiment result shown in Figure 5.1.8 and Figure 5.1.9.

Also note that the pumping rate is very small between the rotation angle of $40^{\circ}\sim80^{\circ}$. 1) This is first caused by the geometrical symmetry of the equilateral triangle about the

fluid incoming direction when θ approaches 30° and 60°. This has been discussed in case 2. 2) This is also caused by the vapor bubbles (cavitation). A large area of vapor bubble (cavitation) is observed between the rotation angle of 40°~80°. In the cavitation area, there is no pressure driven flow, thus there is no axial pumping effect. The maximum load carrying capacity is about $5.5\,\mathrm{N}$ which is much larger than the value $0.6\mathrm{N}$ for the triangular cavity in case 1. However this number is still much smaller than the sealing load $60\,\mathrm{N}$ indicating that a single line of triangular surface asperities also can't hold up a $1\,\mu\mathrm{m}$ gap between the elastomer and the shaft surface.

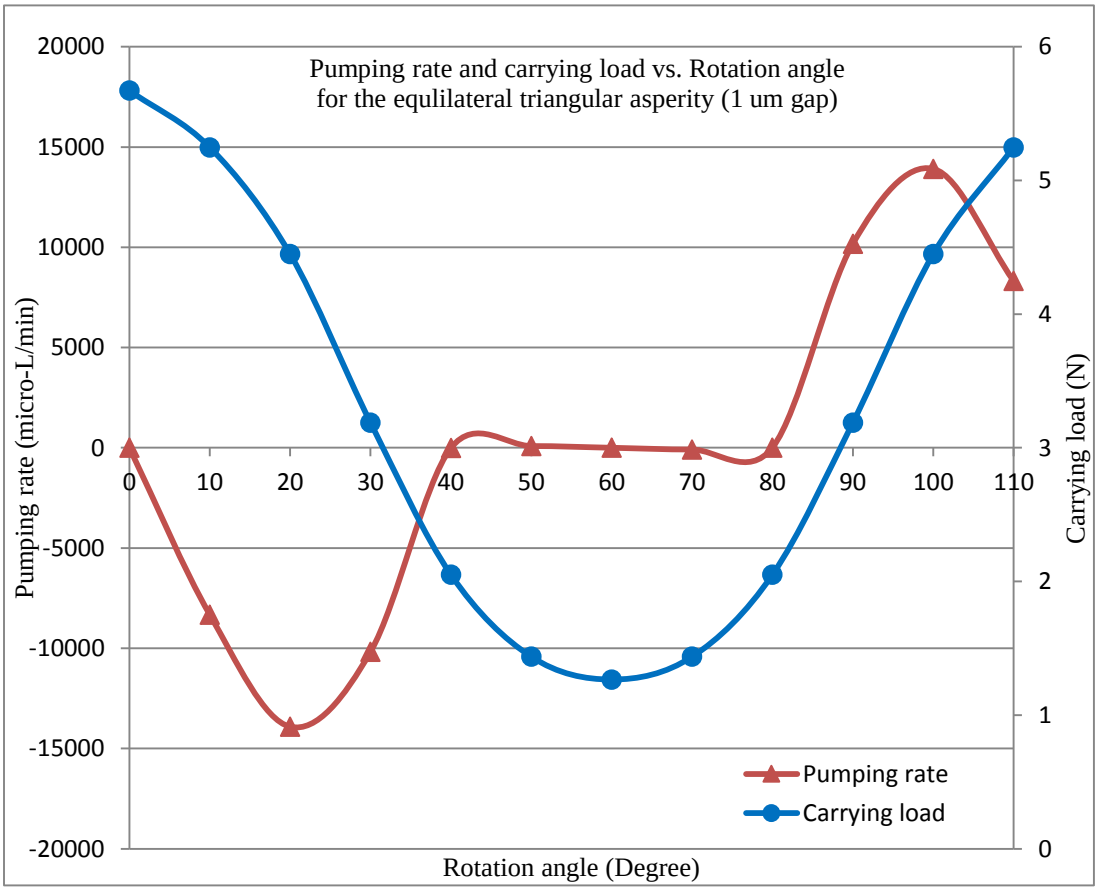

Figure 5.2.8 Angle rotation test for a single triangular surface asperity ($h_{ntri} = 6\ \mu m$)

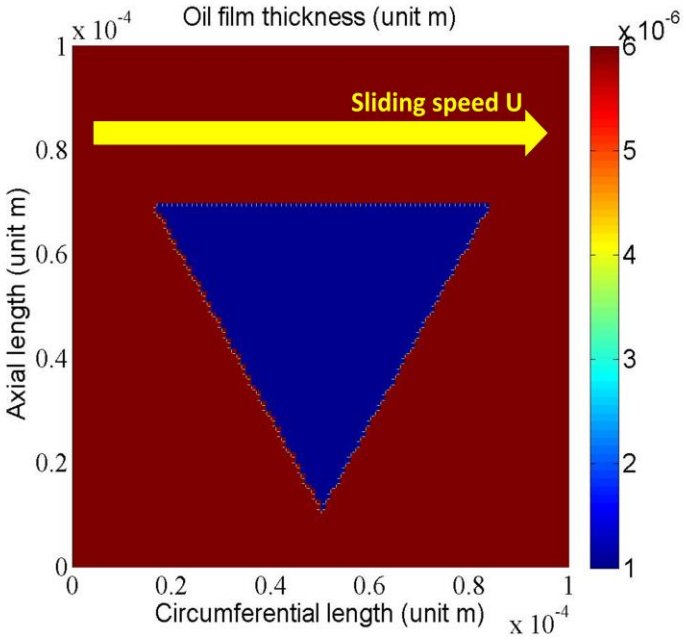

Figure 5.2.9 Oil film thickness over a single triangular asperity ($h_{ntri} = 6$ μm)

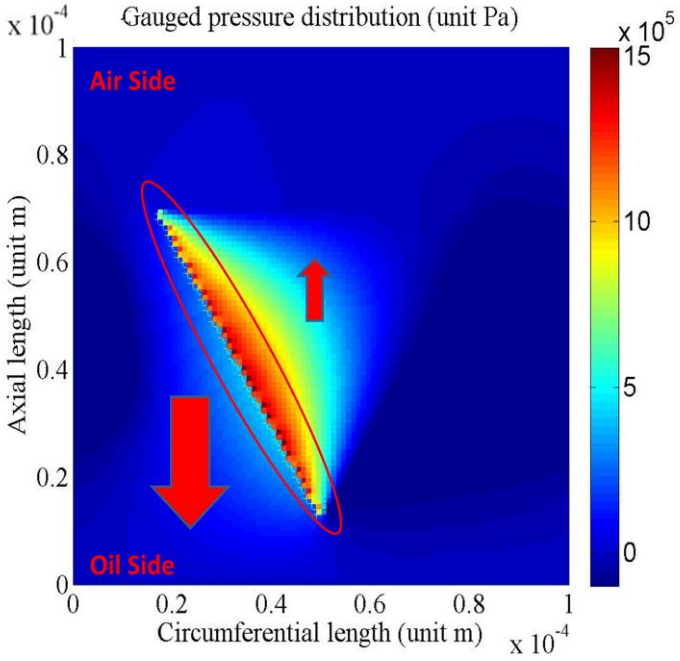

Figure 5.2.10 Gauged pressure distribution over a single triangular asperity ($h_{ntri} = 6$ μm)

Case 4: (Angle rotation test for a single triangular asperity with hntri=7um)

Pattern: single equilateral triangular asperity; (see Figure 5.1.6 (b))

$h_{ntri} = 7\ \mu m;\ dasp = 5\ \mu m;\ U = 5.486\ m/s$ (750 RPM); $\mu = 0.035\ Pa \cdot s;\ P_c = 0\ Pa;$ $P_{b1} = P_{b2} = 101325\ Pa;\ \theta = 0^\circ \sim 110^\circ,\ 10^\circ$ each rotation; $L_x = 100\ \mu m;\ L_y = 100\ \mu m;\ L_{tri} = 96.5\ \mu m;\ m = 101;\ n = 101$ (5.2.4)

Results and interpretation:

The angle rotation test result is given in Figure 5.2.11. The general trend in Figure 5.2.11 is almost the same as in Figure 5.2.8. Compared to Figure 5.2.8, the pumping rate does not change much as the base oil film thickness h_{ntri} increases from $5\ \mu m$ to $6\ \mu m$. While in case 1-2 for the triangular cavity, the pumping rate increases significantly as the base oil film thickness h_{ntri} increases from $1\ \mu m$ to $2\ \mu m$. This is due to both the geometry difference between the cavity and the asperity and the nonlinearity of the Reynolds equation. Specifically, in the Reynolds equation the pressure gradient and the pumping rate are related to the oil film thickness cubed, h^3. When the oil film thickness increases from $1\ \mu m$ to $2\ \mu m$ the percentage increase for h^3 is about $700\ \%$ referring to $1\ \mu m$; When the oil film thickness increases from $6\ \mu m$ to $7\ \mu m$ the percentage increase for h^3 is only about $58.79\ \%$ referring to $6\ \mu m$.

Compared to Figure 5.2.8, there are two small differences. 1) Less vapor bubbles (cavitation) present; 2) The axial pumping effect slightly decreases. These two differences are both due to the increase of the base oil film thickness which decreases the

hydrodynamic effect of the lubricant flow. The decrease of the hydrodynamic effect is also vindicated by the decrease of the load carrying capacity as well as the relaxed pressure gradient shown in Figure 5.2.13 compared to Figure 5.2.10 .

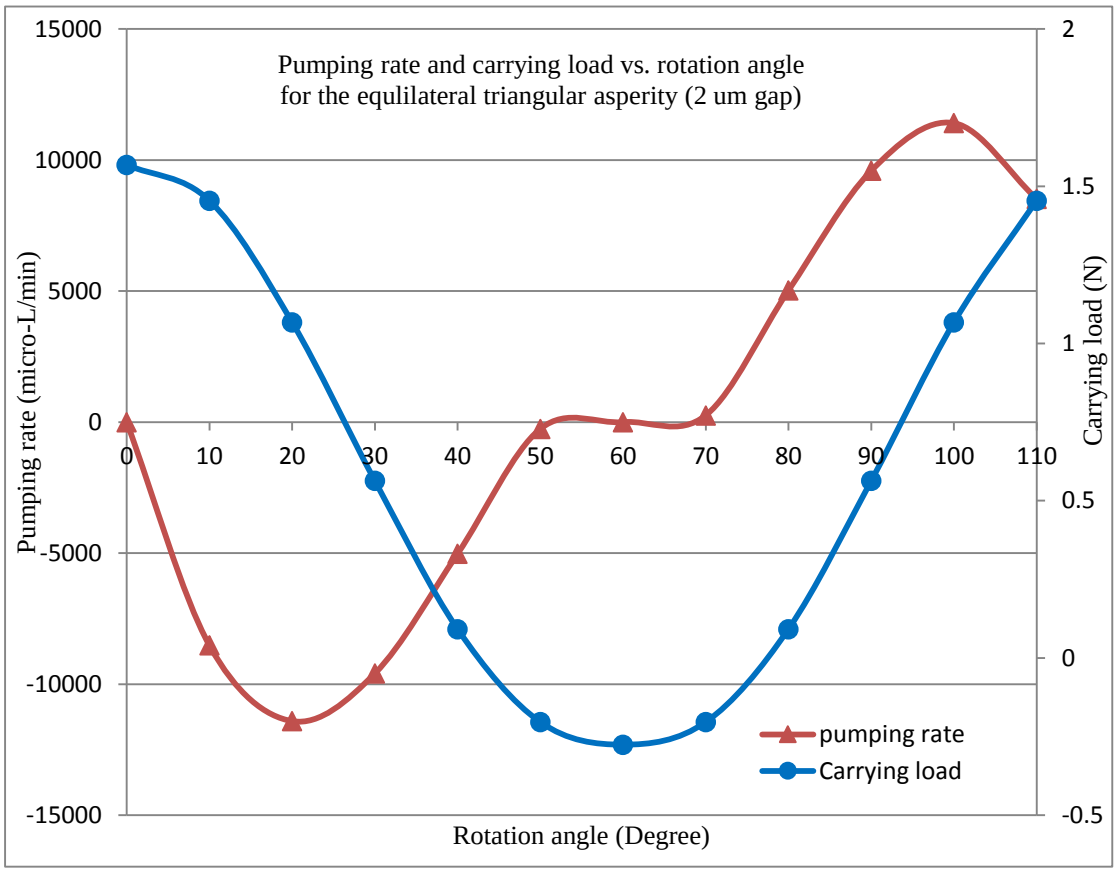

Figure 5.2.11 Angle rotation test for a single triangular surface asperity ($h_{ntri} = 7$ μm)

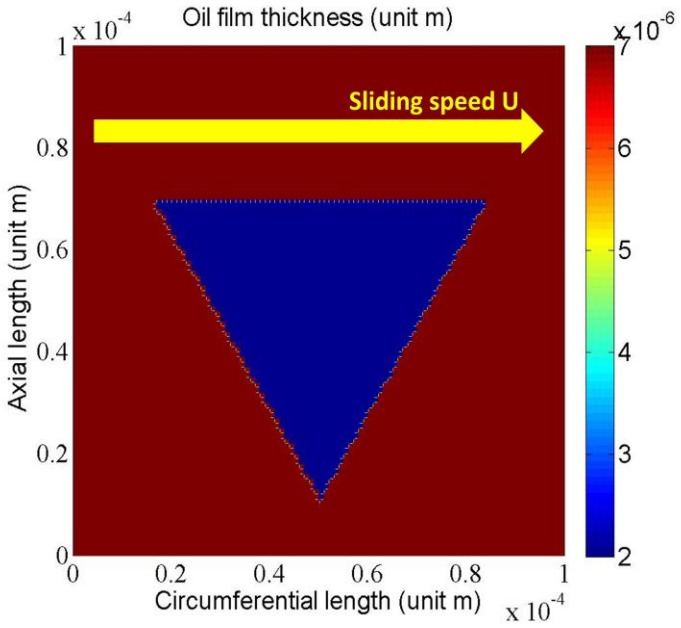

Figure 5.2.12 Oil film thickness over a single triangular asperity ($h_{ntri} = 7$ μm)

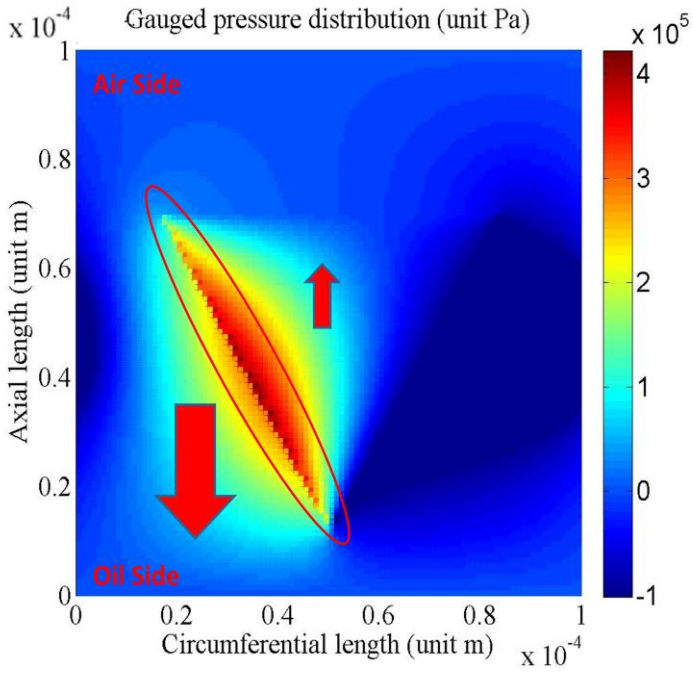

Figure 5.2.13 Gauged pressure distribution over a single triangular asperity ($h_{ntri} = 7$ μm)

Conclusion for case 1-4:

Numerical study cases 1-4 initially prove the directional pumping ability of a single triangular cavity or asperity (which represents a line of equally spaced triangles along the entire circumference). The general conclusion is that triangular cavity tends to pump oil toward its base while the triangular asperity tends to pump oil toward its apex. This means the triangular asperity pumps oil to its pointing direction while the triangular cavity pumps oil oppositely to its pointing direction. In addition, triangular asperity pumps much more oil than the triangular cavity given that the elastomer does not touch the surface texture and maintain $1\sim2\ \mu m$ above the surface texture. The directional pumping mechanism for the surface triangles has also been revealed as the vapor bubble (cavitation) truncates the negative pressure on one side of the surface triangle and the single positive pressure peak on the other side of the surface triangle drives the oil toward the base for the cavity case and toward the apex for the asperity case. This pumping mechanism is different from the directional pumping mechanism of the sinusoidal surface undulations reported in reference [7]. For the sinusoidal surface undulations, the directional pumping ability is due to the different wiping angles which reflect the incoming flow toward different directions as shown in Figure 2.5.1.

Case 5: (Influence of the cavitation threshold pressure Pc to a single triangular cavity)

Pattern: single equilateral triangular cavity; (see Figure 5.1.6 (a))

$h_{ntri} = 2\ \mu m$; dcav $= 5\ \mu m$; $U = 5.486\ m/s$ (750 RPM) ; $\mu = 0.035\ Pa \cdot s$; $P_c = 0 \sim -101325\ Pa,\ -10132.5\ Pa$ each increment; $P_{b1} = P_{b2} = 101325\ Pa$; $\theta = 90^{\circ}$; $L_x = 100\ \mu m$; $L_y = 100\ \mu m$; $L_{tri} = 96.5\ \mu m$; $m = 101$; $n = 101$ (5.2.5)

Results and interpretation:

The pumping rate and the load capacity vs. cavitation threshold pressure curves are given in Figure 5.2.14. The general trend shows that as the cavitation threshold pressure decreases (which means the vapor bubble is more difficult to form), both the pumping rate and the load carrying ability increase.

Figure 5.2.15- Figure 5.2.18 give the gauged pressure distribution and the cavitation index for the simulation when the cavitation threshold pressure is $0\ Pa$ and $-101325\ Pa$ respectively. It can be seen that a lower caviation threshold pressure inhibits the formation of the vapor bubble while raising the positive fluid pressure around the triangle leading to an increased load capacity. Less vapor bubbles are also responsible for an increased pumping rate because the vapor bubble tends to impede any axial pressure driven flow. However, it should be noted that as the cavitation (vapor bubble) area further decreases shrinking to the edge of the surface triangle, both the load capacity and the pumping rate would decrease and eventually go to zero. Because if there is absolutely no cavitation formed, the fluid pressure distribution on the two edges of the

surface triangle would be perfectly anti-symmetrical resulting in a zero net load capacity. Anti-symmetrical fluid pressure distribution also means the two edges of the triangle separated by the center line would pump the same amount of oil to the opposite directions and form a zero net pumping rate. The influence of the cavitation threshold pressure to the lubricant field is strongly nonlinear.

The cavitation threshold pressure P_c is an important property of the lubricant depending on oil type. Since the actual cavitation threshold pressure for the SAE20W50 oil is not measured in the experiment, a value of $P_c = 0$ from reference [7], [42]-[43], [49]-[53] is used in this study.

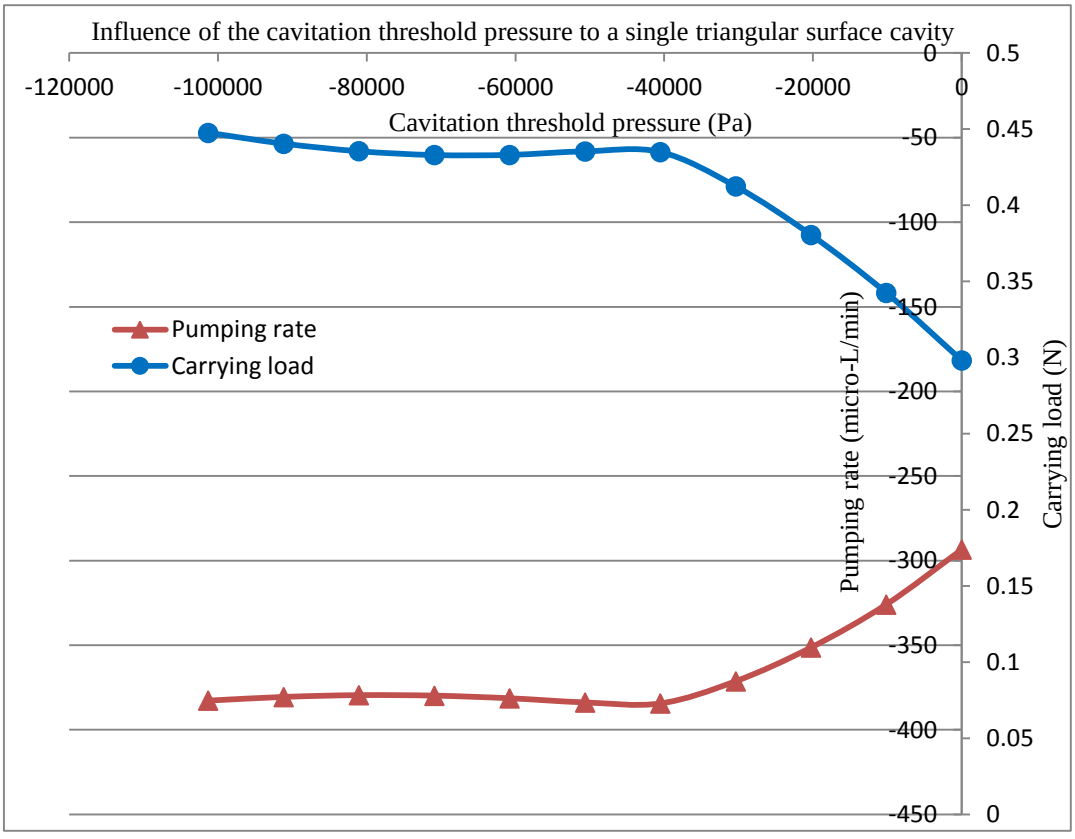

Figure 5.2.14 Influence of the cavitation threshold pressure to a single triangular cavity

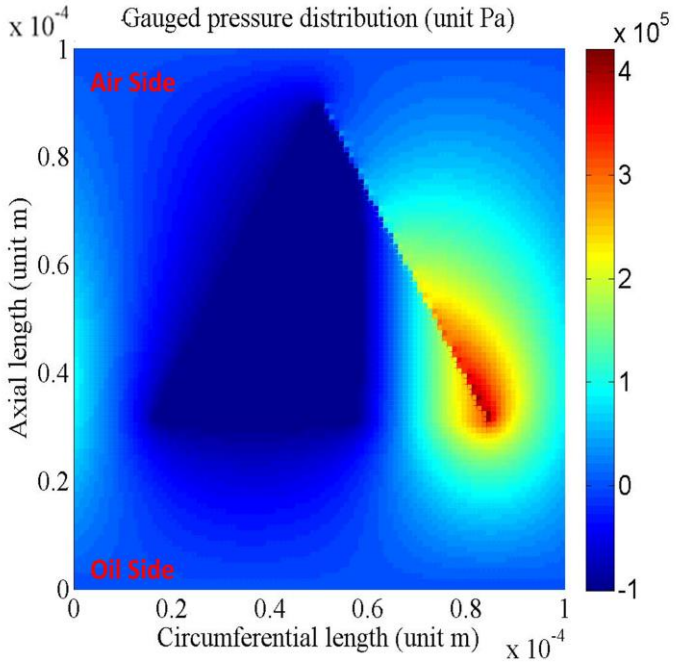

Figure 5.2.15 Gauged pressure distribution over a single triangular cavity with (P_c = 0 Pa)

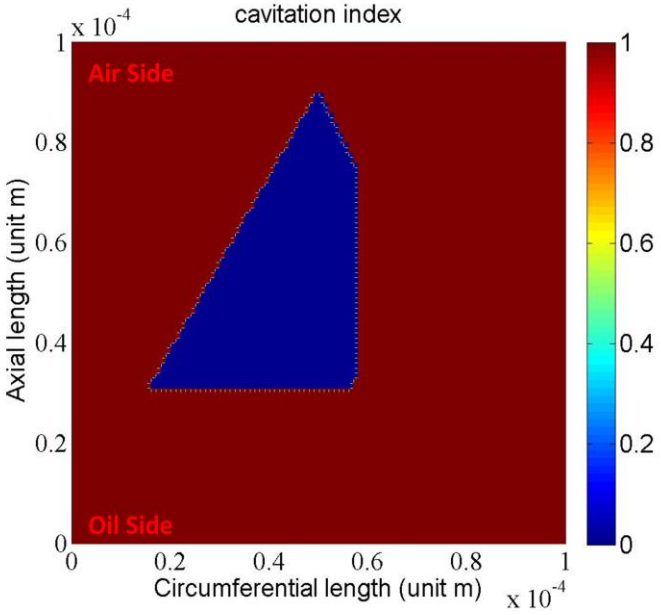

Figure 5.2.16 Cavitation index over a single triangular cavity with (P_c = 0 Pa)

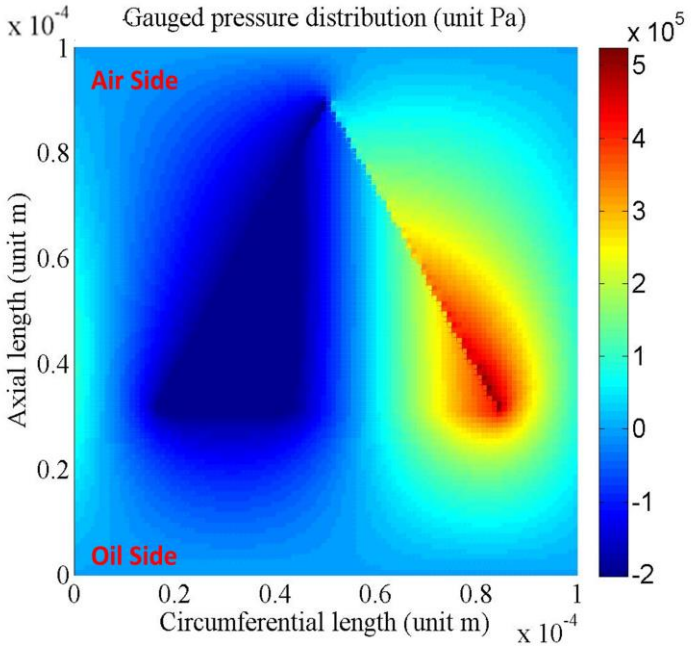

Figure 5.2.17 Gauged pressure distribution over a single triangular cavity with ($P_c = -101325$ Pa)

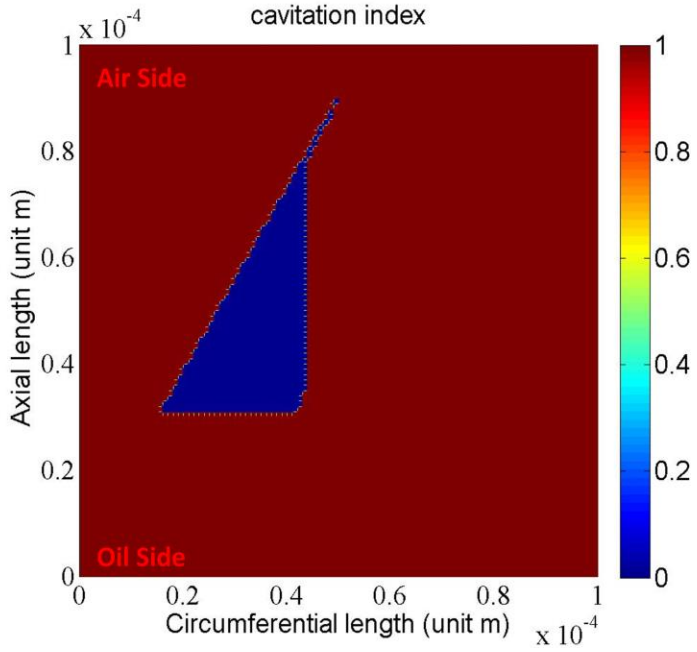

Figure 5.2.18 Cavitation index over a single triangular cavity with ($P_c = -101325$ Pa)

Case 6: (Influence of the cavitation threshold pressure Pc to a single triangular asperity)

Pattern: single equilateral triangular asperity; (see Figure 5.1.6 (b))

$h_{ntri} = 2\ \mu m$; $dasp = 5\ \mu m$; $U = 5.486\ m/s$ (750 RPM) ; $\mu = 0.035\ Pa \cdot s$; $P_c = 0 \sim -101325\ Pa,\ -10132.5\ Pa$ each increment; $P_{b1} = P_{b2} = 101325\ Pa$; $\theta = 90^{\circ}$; $L_x = 100\ \mu m$; $L_y = 100\ \mu m$; $L_{tri} = 96.5\ \mu m$; $m = 101$; $n = 101$

(5.2.6)

Results and interpretation:

The pumping rate and the load capacity vs. cavitation threshold pressure curves are given in Figure 5.2.19. The general trend shows that as the cavitation threshold pressure decreases, both the pumping rate and the load carrying ability decrease.

It is also seen that the vapor bubble area decreases as the cavitation threshold pressure decrease. However, this does not lead to an increase in the pumping rate or an increase load capacity. In the contrary, the pumping rate and the load capacity decrease. This is because the positive pressure peak on one side of the triangular asperity decreases. As the cavitation area completely disappears due to an even smaller cavitation pressure, both the pumping rate and the load capacity would become zero because of an anti-symmetrical fluid pressure distribution which has been introduced in case 5

Figure 5.2.20- Figure 5.2.23 give the gauged pressure distribution and the cavitation index for the simulation when the cavitation threshold pressure are $0\ Pa$ and $-101325\ Pa$ respectively.

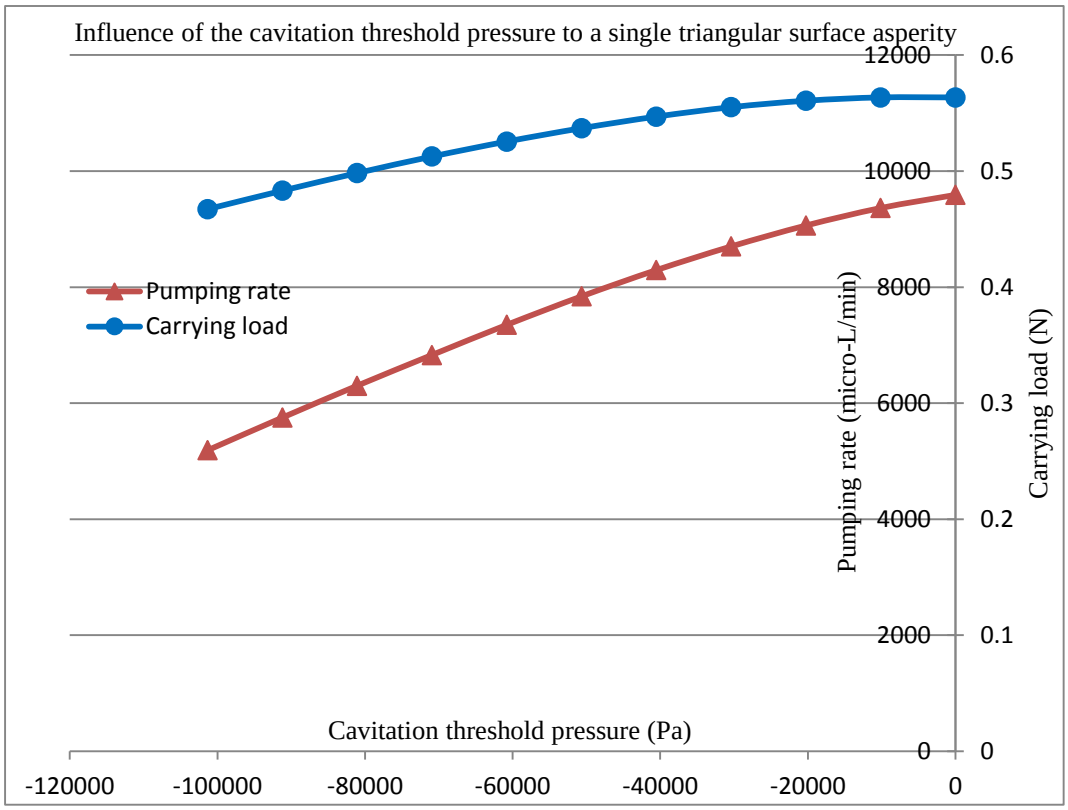

Figure 5.2.19 Influence of the cavitation threshold pressure to a single triangular asperity

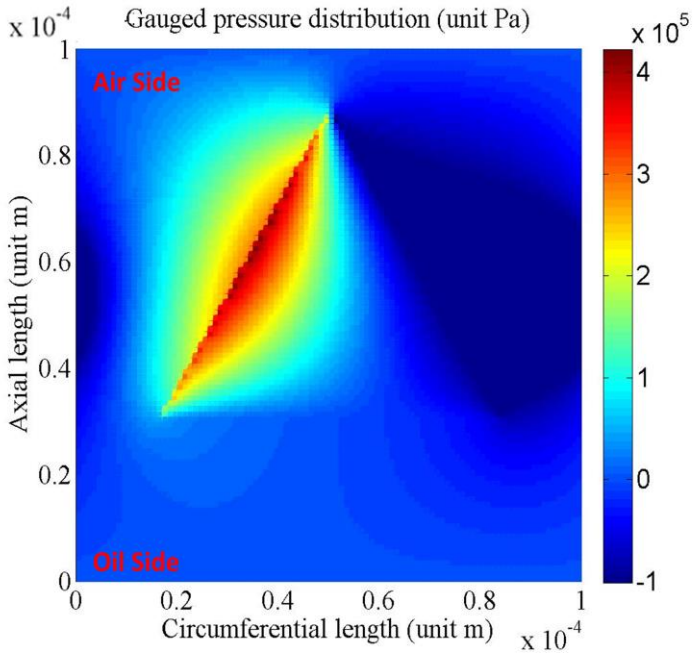

Figure 5.2.20 Gauged pressure distribution over a single triangular asperity with (P_c = 0 Pa)

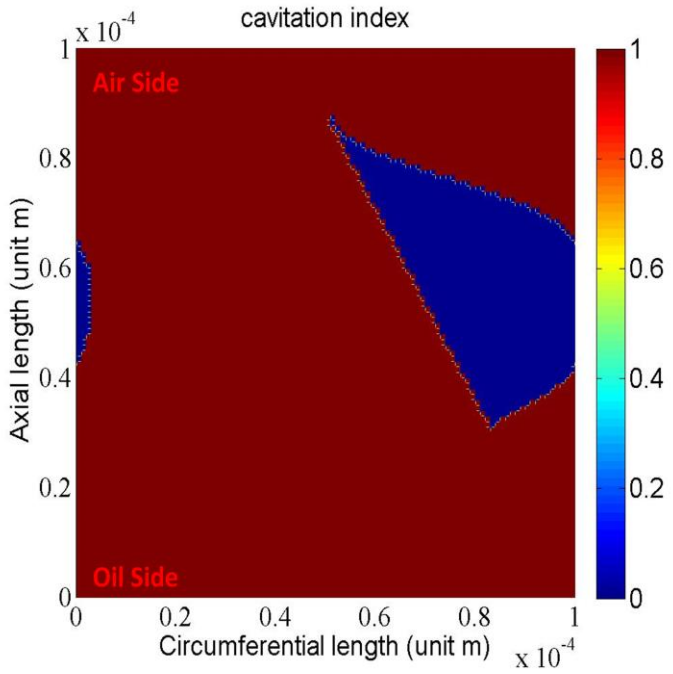

Figure 5.2.21 Cavitation index over a single triangular asperity with ($P_c = 0$ Pa)

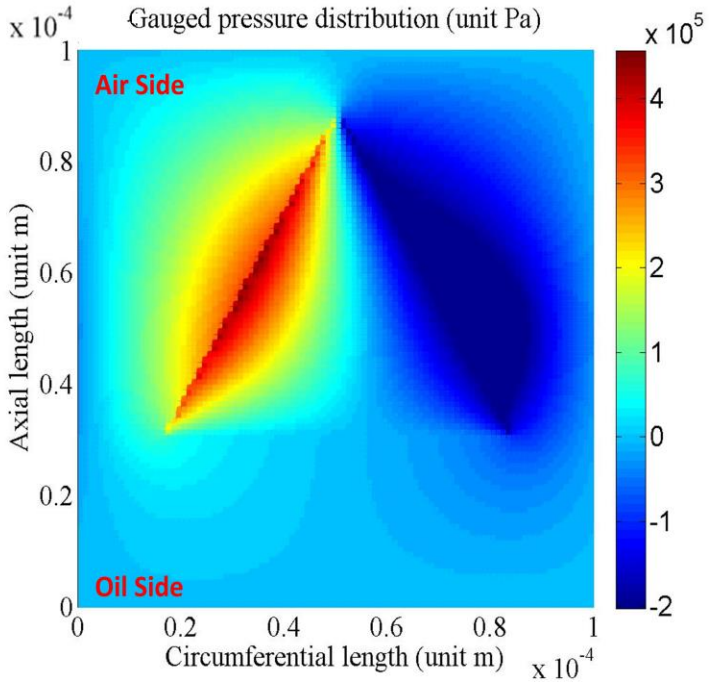

Figure 5.2.22 Gauged pressure distribution over a single triangular asperity with ($P_c = -101325$ Pa)

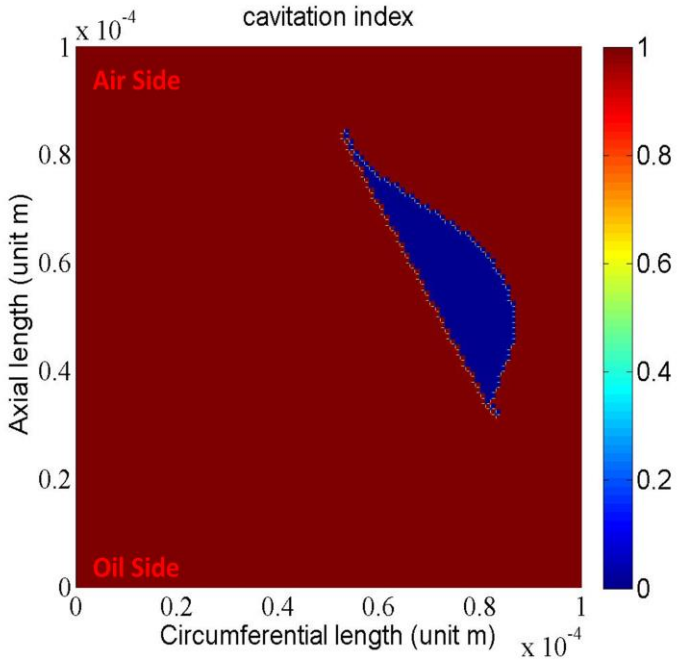

Figure 5.2.23 Cavitation index over a single triangular asperity with ($P_c = -101325$ Pa)

Conclusion for case 5-6

The decrease of the cavitation threshold pressure makes it more difficult for the vapor bubble to form and consequently leads to a smaller cavitation area as shown in case 5-6. But its influence to the axial pumping rate as well as the load carrying capacity is uncertain. The relationship between the fluid pressure distribution and the cavitation threshold pressure is nonlinear and is sensitive to other numerical parameters like the oil film thickness distribution.

5.3 Numerical Study on Staggered Surface Triangles

Case 7: (staggered equilateral triangular cavities orientated at 0, 30, 60, 90 degree with hntri=1um)

Pattern: staggered equilateral triangular cavities (see Figure 5.1.3 for the staggered pattern)

$h_{ntri} = 1\mu m;\ dcav = 5\mu m;\ U = 5.486\ m/s\ (750\ RPM);\ \mu = 0.035\ Pa \cdot s;\ P_c = 0\ Pa;$ $P_{b1} = P_{b2} = 101325 Pa;\ \theta = 0^{\circ}, 30^{\circ}, 60^{\circ}, 90^{\circ};\ L_x = 228\ \mu m;\ L_y = 150\ \mu m;\ L_{tri} =$ $96.5\ \mu m;\ m = 229\ ;\ n = 151$ (5.3.1)

Result and interpretation

The pumping rate and the carrying load vs. pointing angle for the staggered triangular cavities with $h_{ntri} = 1\ \mu m$ are given in Figure 5.3.1. Compared to case 1 in section 5.2, the axial computational length doubles in this case covering two rows of staggered triangles in the axial direction. The pumping rate at the pointing angle $\theta = 0^{\circ}, 30^{\circ}, 60^{\circ}, 90^{\circ}$ in Figure 5.3.1 does not change a lot while the carrying load doubles compared to Figure 5.2.2. The staggered triangular cavities still pump oil toward their bases and the impedance caused by the staggered pattern does not influence the axial pumping rate too much. Like the single triangular cavity case, the excessive presence of the vapor bubble greatly inhibits the axial pumping ability in this case. The load capacity almost doubles simply because an additional row of triangles is included. Figure 5.3.2 shows the oil pressure distribution over the staggered triangular cavities.

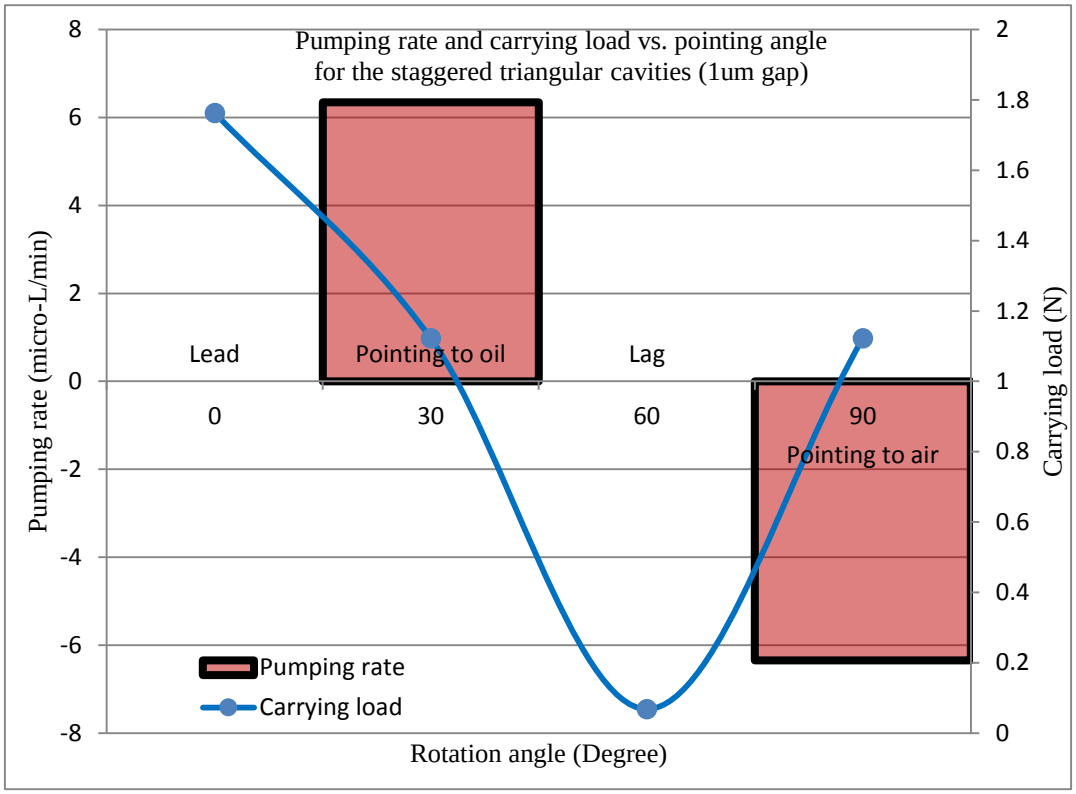

Figure 5.3.1Pumping rate and load carrying capacity for the staggered triangular cavities ($h_{ntri} = 1$ μm)

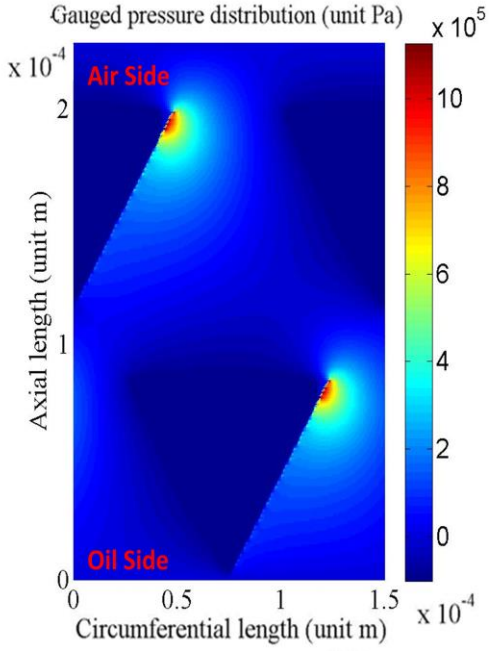

Figure 5.3.2 Oil pressure distribution over the staggered triangular cavities ($h_{ntri} = 1$ μm)

Case 8: (staggered equilateral triangular cavities orientated at 0, 30, 60, 90 degree with hntri=2um)

Pattern: staggered equilateral triangular cavities (see Figure 5.1.3 for the staggered pattern)

$h_{ntri} = 2\mu m;\ dcav = 5\mu m;\ U = 5.486\ m/s\ (750\ RPM);\ \mu = 0.035\ Pa \cdot s;\ P_c = 0\ Pa;\ P_{b1} = P_{b2} = 101325 Pa;\ \theta = 0^{\circ}, 30^{\circ}, 60^{\circ}, 90^{\circ};\ L_x = 228\ \mu m;\ L_y = 150\ \mu m;\ L_{tri} = 96.5\ \mu m;\ m = 229\ ;\ n = 151$ (5.3.2)

Result and interpretation:

The pumping rate and the carrying load vs. pointing angle for the staggered triangular cavities with $h_{ntri} = 2\ \mu m$ are given in Figure 5.3.3. This case is different from case 7 as the base oil film thickness $h_{ntri} = 2\ \mu m$. The increase of the base oil film thickness greatly increases the pumping rate of the staggered triangular cavities. The reason for this has been explained in case 2. Compared to Figure 5.2.5 in case 2, the staggered pattern does not change the pumping rate at $\theta = 30^{\circ}$ and $\theta = 90^{\circ}$ a lot. Figure 5.3.4 shows the oil pressure distribution and Figure 5.3.5 shows the axial flow rate distribution over the staggered triangular cavities in this case. It is seen clearly that the triangular cavities drive oil toward its bases indicated by a positive flow rate in Figure 5.3.5.

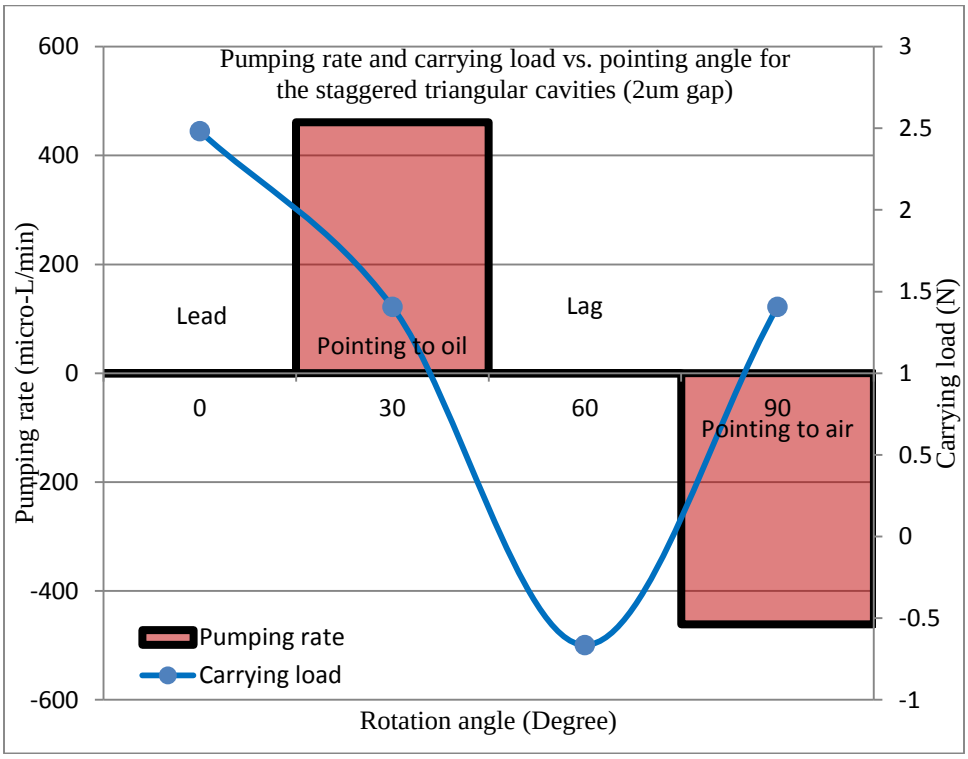

Figure 5.3.3 Pumping rate and load carrying capacity for the staggered triangular cavities ($h_{ntri} = 2$ μm)

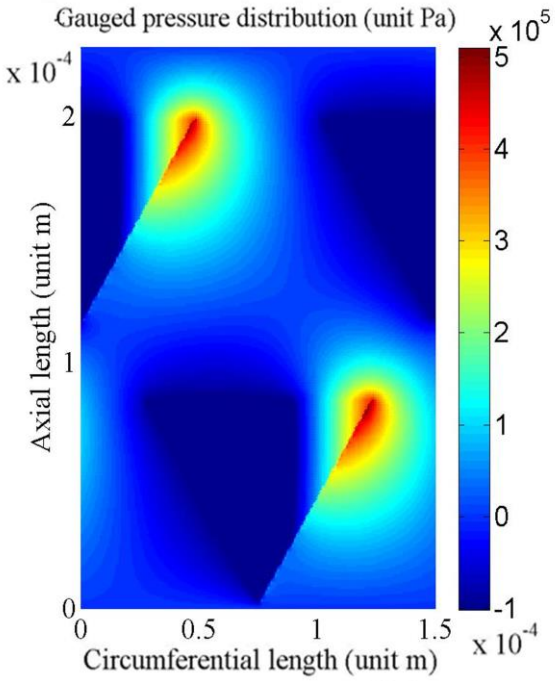

Figure 5.3.4 Oil pressure distribution over the staggered triangular cavities ($h_{ntri} = 2$ μm)

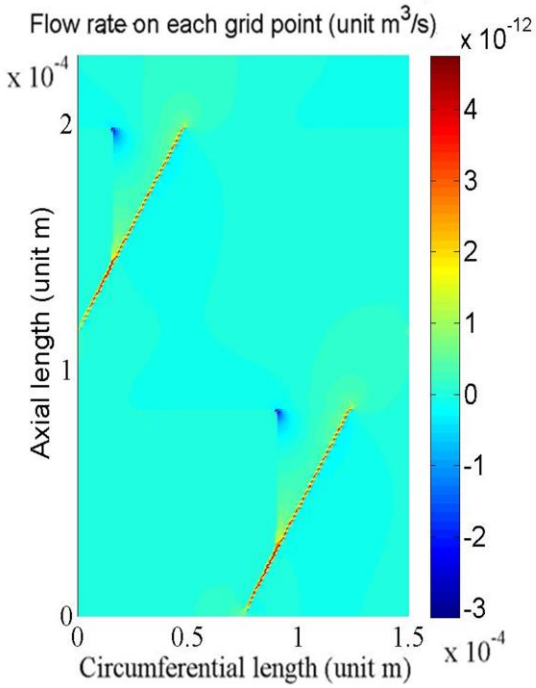

Figure 5.3.5 Axial flow rate over the staggered triangular cavities ($h_{ntri} = 2\ \mu m$)

Case 9: (staggered equilateral triangular asperities orientated at 0, 30, 60, 90 degree with hntri=6um)

Pattern: staggered equilateral triangular asperities (see Figure 5.1.3 for the staggered pattern)

$h_{ntri} = 6\mu m;\ dasp = 5\mu m;\ U = 5.486\ m/s\ (750\ RPM);\ \mu = 0.035\ Pa \cdot s;\ P_c = 0\ Pa;\ P_{b1} = P_{b2} = 101325 Pa;\ \theta = 0^{\circ}, 30^{\circ}, 60^{\circ}, 90^{\circ};\ L_x = 228\ \mu m;\ L_y = 150\ \mu m;\ L_{tri} = 96.5\ \mu m;\ m = 229\ ;\ n = 151$ (5.3.3)

Result and interpretation:

The pumping rate and the carrying load vs. pointing angle for the staggered triangular asperities with $h_{ntri} = 6\ \mu m$ are given in Figure 5.3.6. Compared to Figure

5.2.8 in case 3, the staggered pattern does not change the pumping ability of the triangular asperities too much at $\theta = 0^{\circ}, 30^{\circ}, 60^{\circ}, 90^{\circ}$; while increases the load capacity significantly. At $\theta = 30^{\circ}$, the carrying load increases from about 3 N to about 16 N. At $\theta = 90^{\circ}$ the carrying load increases from about 3 N to 8 N.

Also the staggered triangular asperities pump much more oil than the staggered triangular cavities. The reason for this has been given in case 3 in section 5.2. Figure 5.3.7 shows the oil pressure distribution over the staggered triangular cavities in this case.

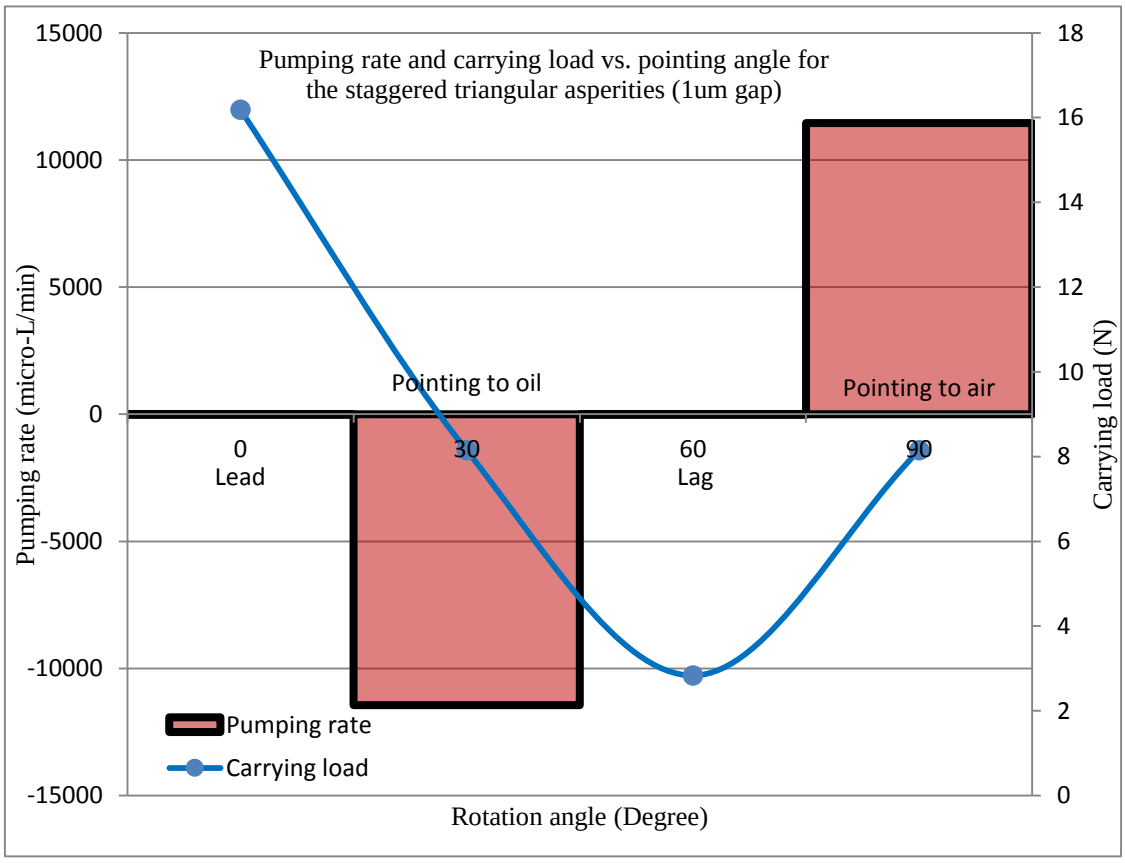

Figure 5.3.6 Pumping rate and load carrying capacity for the staggered triangular asperities ($h_{ntri} = 6\ \mu m$)

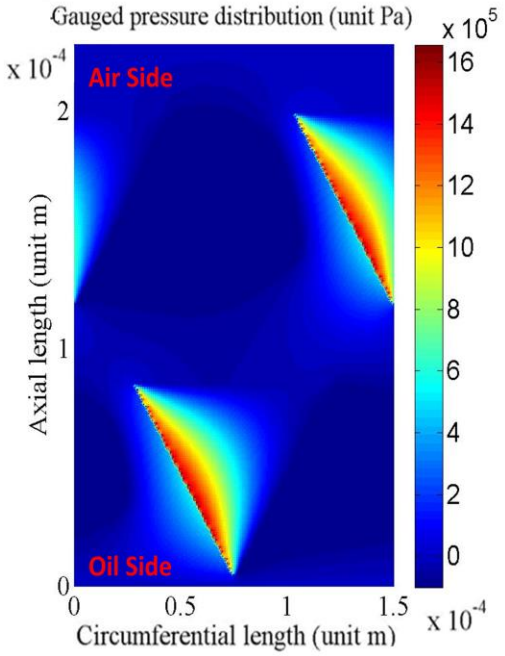

Figure 5.3.7 Oil pressure distribution over the staggered triangular asperities ($h_{ntri} = 6\ \mu m$)

Case 10: (staggered equilateral triangular asperities orientated at 0, 30, 60, 90 degree with hntri=7um)

Pattern: staggered equilateral triangular asperities (see Figure 5.1.3 for the staggered pattern)

$h_{ntri} = 7\mu m;\ dasp = 5\mu m;\ U = 5.486\ m/s\ (750\ RPM);\ \mu = 0.035\ Pa \cdot s;\ P_c = 0\ Pa;\ P_{b1} = P_{b2} = 101325 Pa;\ \theta = 0^{\circ}, 30^{\circ}, 60^{\circ}, 90^{\circ};\ L_x = 228\ \mu m;\ L_y = 150\ \mu m;\ L_{tri} = 96.5\ \mu m;\ m = 229;\ n = 151$ (5.3.4)

Result and interpretation:

The pumping rate and the carrying load vs. pointing angle for the staggered triangular asperities with $h_{ntri} = 7\ \mu m$ are given in Figure 5.3.8. Compared to Figure

5.3.6 in case 9, the pumping rate does not change too much as the base oil film thickness h_{tri} increases from 6 μm to 7 μm. The reason for this has been given in case 3 in section 5.2. The carrying load decreases as the base oil film thickness increases when compared to Figure 5.3.6. Figure 5.3.9 shows the oil pressure distribution and Figure 5.3.10 shows the axial flow rate distribution over the staggered triangular asperities in this case. It is seen clearly that the oil is driven toward the apexes indicated by a negative axial flow rate around one side of the triangular asperities.

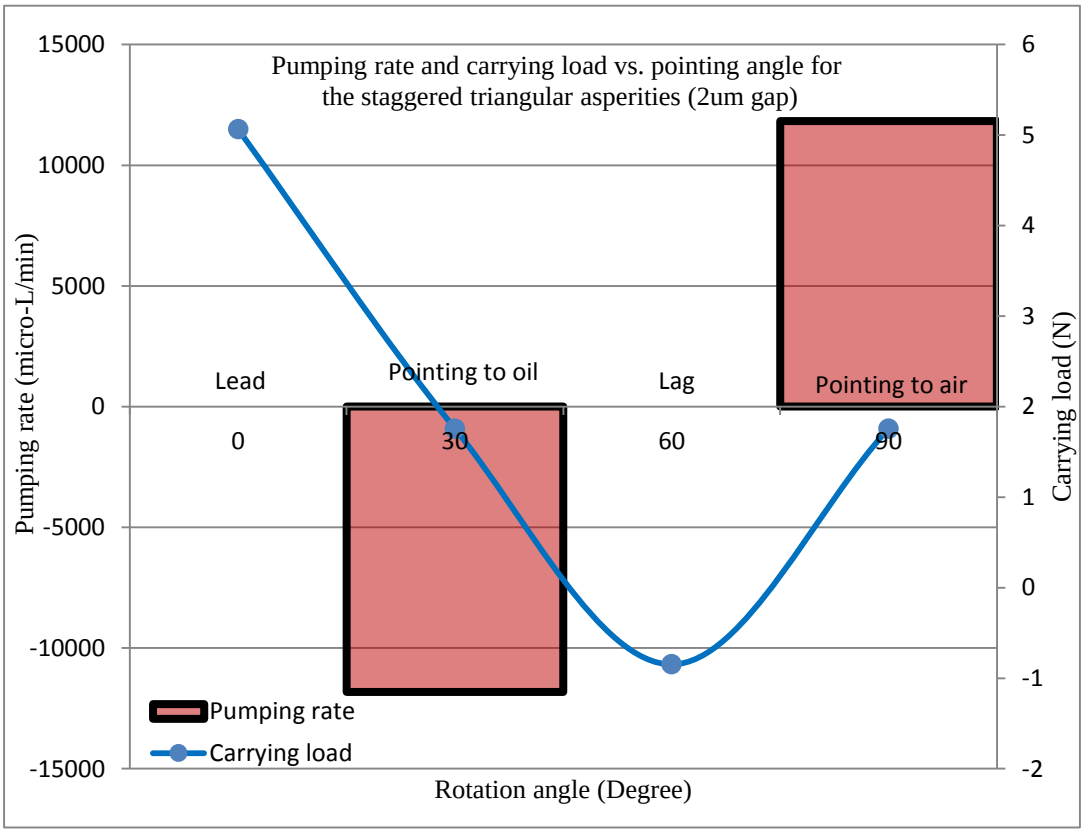

Figure 5.3.8 Pumping rate and load carrying capacity for the staggered triangular asperities ($h_{ntri} = 7$ μm)

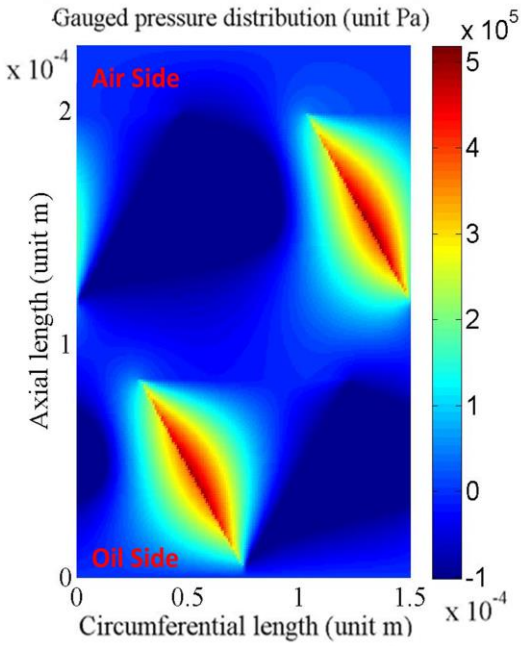

Figure 5.3.9 Oil pressure distribution over the staggered triangular asperities (h_{ntri} = 7 μm)

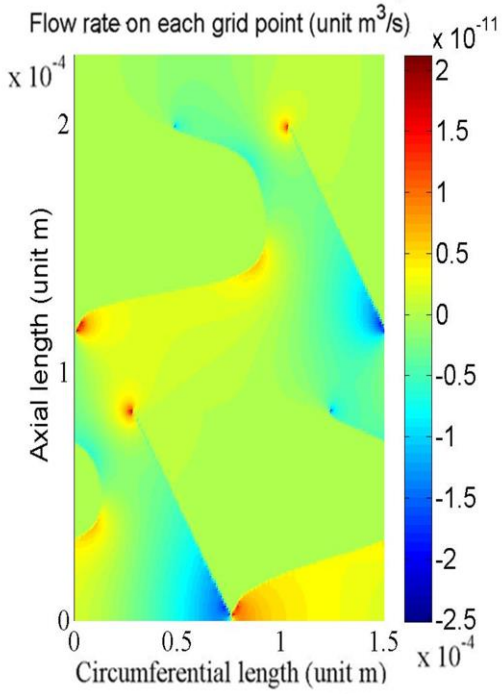

Figure 5.3.10 Axial flow rate over the staggered triangular asperities (h_{ntri} = 7 μm)

5.4 Double Long Staggered Surface Triangular Texture

Case 11: (double staggered equilateral triangular cavities orientated at 0, 30, 60, 90 degree with hntri=1um)

Pattern: double long staggered equilateral triangular cavities

$h_{ntri} = 1\mu m;\ dcav = 5\mu m;\ U = 5.486\ m/s$ (750 RPM); $\mu = 0.035\ Pa \cdot s;\ P_c = 0\ Pa;$ $P_{b1} = P_{b2} = 101325Pa;\ \theta = 0^{\circ} \sim 110^{\circ},\ 10^{\circ}$ each rotation; $L_x = 448\ \mu m;\ L_y = 300\ \mu m;\ L_{tri} = 96.5\ \mu m;\ m = 449;\ n = 301$ (5.4.1)

Result and interpretation:

This section is intended for testing the influence of the sealing zone length to the axial pumping rate of the surface triangles. Other than the computational length, which is increasing from $224\ \mu m$ to $448\ \mu m$ and covering two additional rows of staggered triangles , everything else in this section is the same as it is in section 5.3. Case 11-14 are corresponding to case 7-10 in section 5.3.

The pumping rate and the carrying load vs. pointing angle for the double staggered triangular cavities with $h_{tri} = 6\ \mu m$ are given in Figure 5.4.1. Compared to Figure 5.3.1 in section 5.3, the pumping rate of the double staggered triangular cavities does not change much while the load carrying capacity almost doubled. The reason for the insignificant axial flow change is the series connecting pattern of the surface triangles. Each line of triangles contributes to the axial pumping rate in a sequential way. The increase of the load capacity is simply because more surface triangles are included.

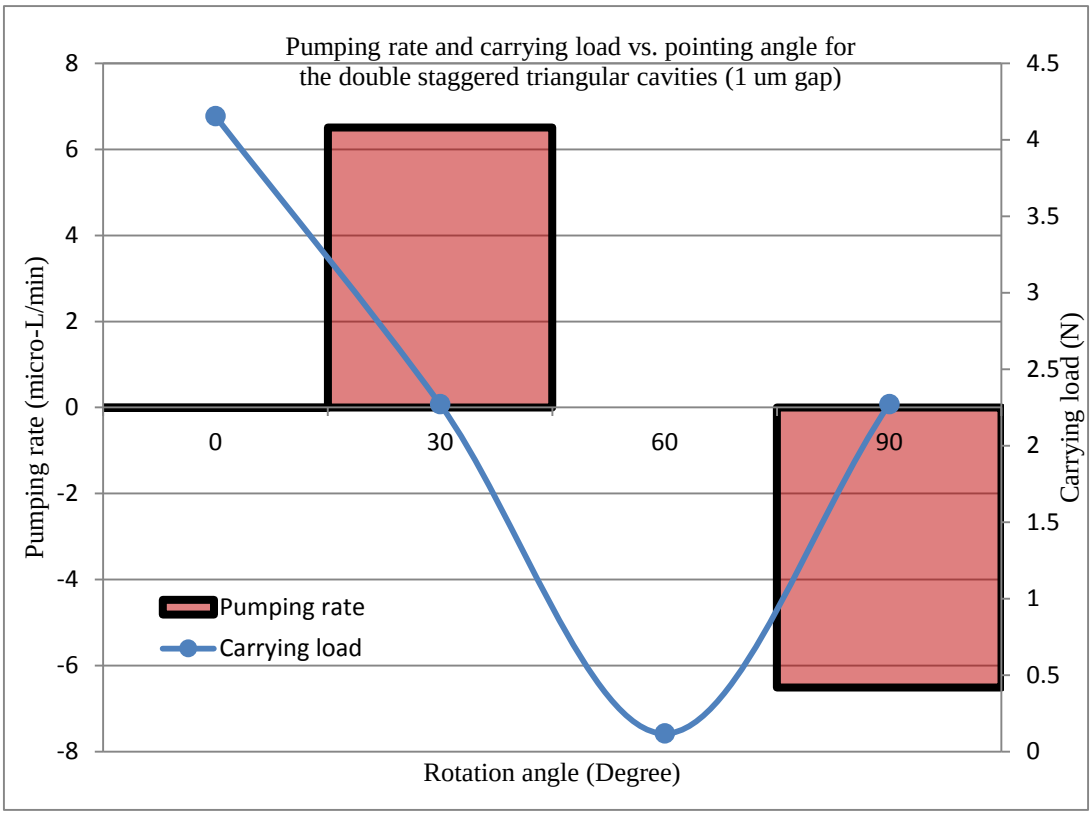

Figure 5.4.1 Pumping rate and load carrying capacity for the double staggered triangular cavities ($h_{ntri} = 1\mu m$)

Case 12: (double staggered equilateral triangular cavities orientated at 0, 30, 60, 90 degree with hntri=2um)

Pattern: double long staggered equilateral triangular cavities;

$h_{ntri} = 2\mu m$; dcav $= 5\mu m$; $U = 5.486\ m/s$; $\mu = 0.035\ Pa \cdot s$; $P_c = 0\ Pa$; $P_{b1} = P_{b2} = 101325 Pa$; $\theta = 0^{\circ} \sim 110^{\circ}$, 10° each rotation; $L_x = 448\ \mu m$; $L_y = 300\ \mu m$; $L_{tri} = 96.5\ \mu m$; $m = 449$; $n = 301$ (5.4.2)

Result and interpretation:

The pumping rate and the carrying load vs. pointing angle for the double staggered

triangular cavities with $h_{ntri} = 7\ \mu m$ are given in Figure 5.4.2. Compared to Figure 5.4.1 the pumping rate increases significantly while the carrying load decreases. The reason for this has been explained in case 2 in section 5.2.

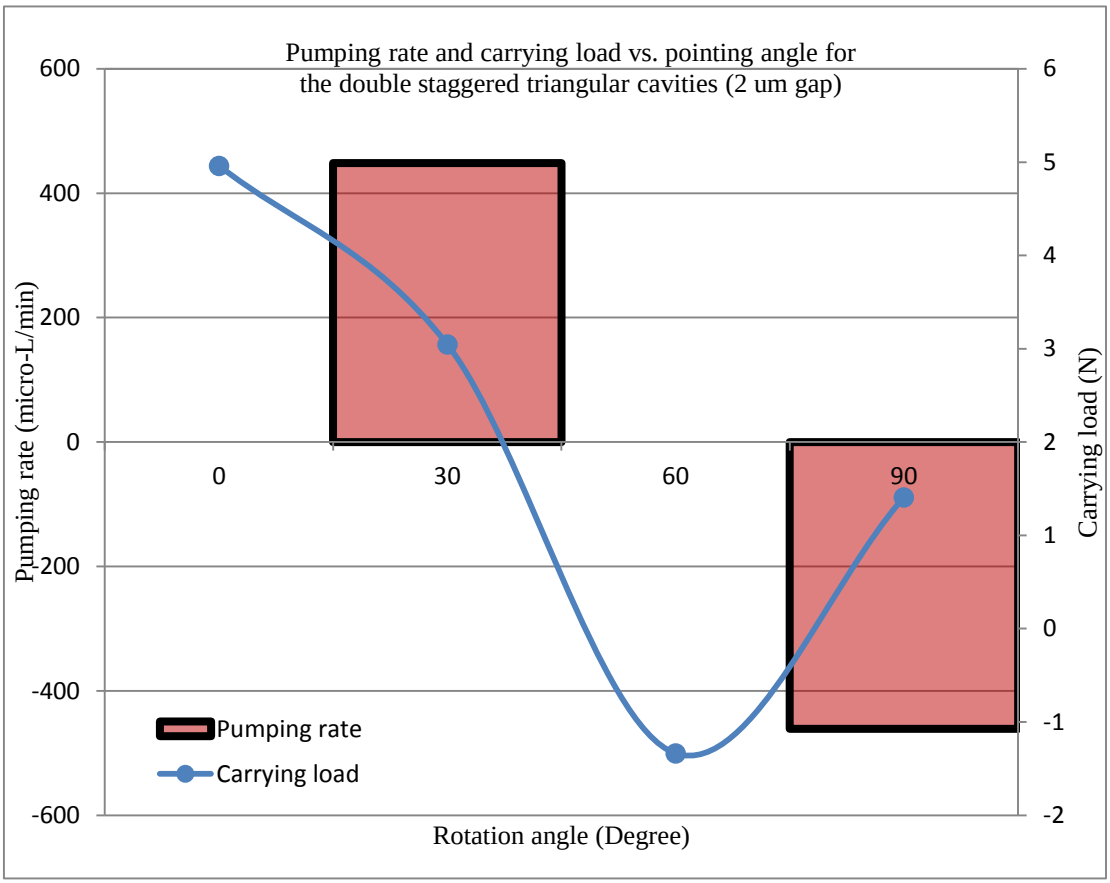

Figure 5.4.2 Pumping rate and load carrying capacity for the double staggered triangular cavities ($h_{ntri} = 2\mu m$)

Case 13: (double staggered equilateral triangular asperities orientated at 0, 30, 60, 90 degree with hntri=6um)

Pattern: double long staggered equilateral triangular asperities;

$h_{ntri} = 6\mu m$; $dasp = 5\mu m$; $U = 5.486\ m/s$; $\mu = 0.035\ Pa \cdot s$; $P_c = 0\ Pa$; $P_{b1} = P_{b2} = 101325 Pa$; $\theta = 0^\circ \sim 110^\circ$, 10° each rotation; $L_x = 448\ \mu m$; $L_y = 300\ \mu m$; $L_{tri} = 96.5\ \mu m$; $m = 229$; $n = 151$ (5.4.3)

Result and interpretation:

The pumping rate and the carrying load vs. pointing angle for the double staggered triangular asperities with $h_{ntri} = 6\ \mu m$ are given in Figure 5.4.3. Compared to Figure 5.3.5 in case 9 section 5.3, the pumping ability of the staggered triangular asperities does not change a lot as the effective sealing length doubles. The carrying load significantly increases almost doubles as more asperities are included. The reason for the above result has been given in case 11 of this section.

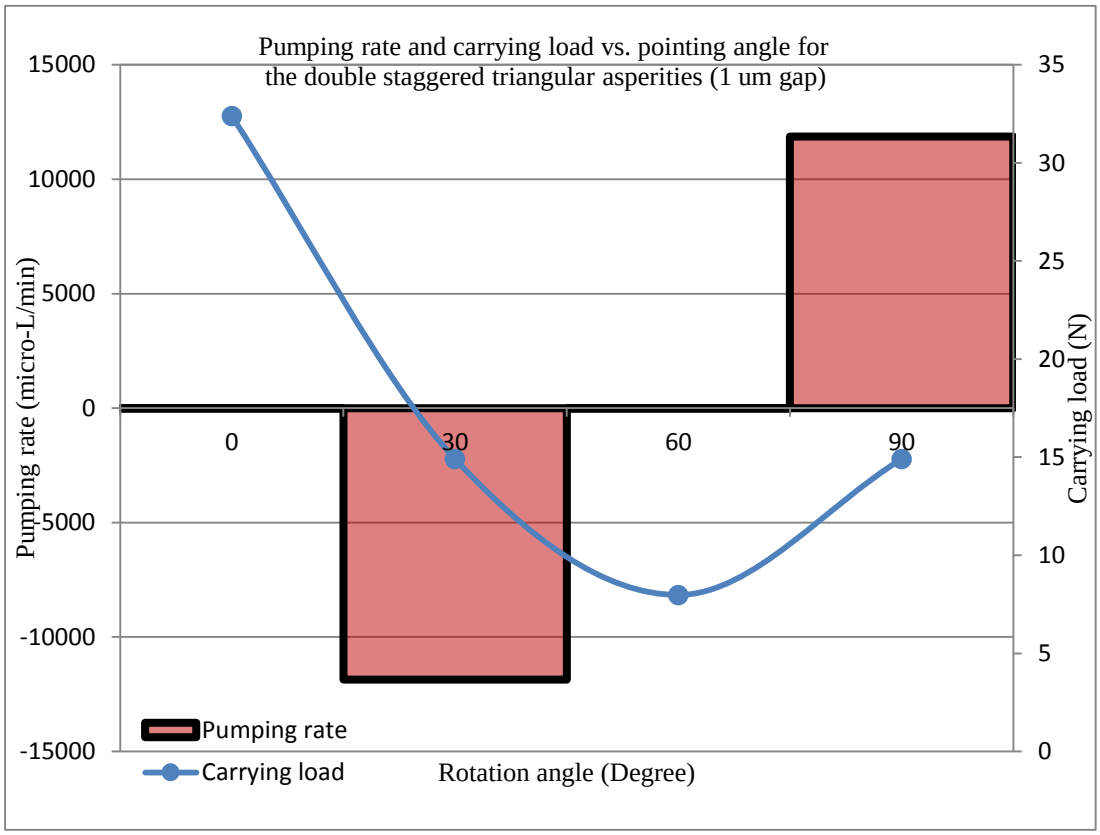

Figure 5.4.3 Pumping rate and load carrying capacity for the double staggered triangular asperities ($h_{ntri} = 1\mu m$)

Case 14: (double staggered equilateral triangular asperities orientated at 0, 30, 60, 90 degree with hntri=7um)

Pattern: double long staggered equilateral triangular asperities;

$h_{ntri} = 7\mu m$; dasp $= 5\mu m$; $U = 5.486\ m/s$; $\mu = 0.035\ Pa \cdot s$; $P_c = 0\ Pa$; $P_{b1} = P_{b2} = 101325 Pa$; $\theta = 0^{\circ} \sim 110^{\circ}$, 10° each rotation; $L_x = 448\ \mu m$; $L_y = 300\ \mu m$; $L_{tri} = 96.5\ \mu m$; $m = 229$; $n = 151$ (5.4.4)

Result and interpretation:

The pumping rate and the carrying load vs. pointing angle for the double staggered

triangular asperities with $h_{ntri} = 7\ \mu m$ are given in Figure 5.4.4. Compared to Figure 5.4.3 the pumping rate changes slightly and the carrying load decreases significantly. The reason for this has been explained in case 4 in section 5.2.

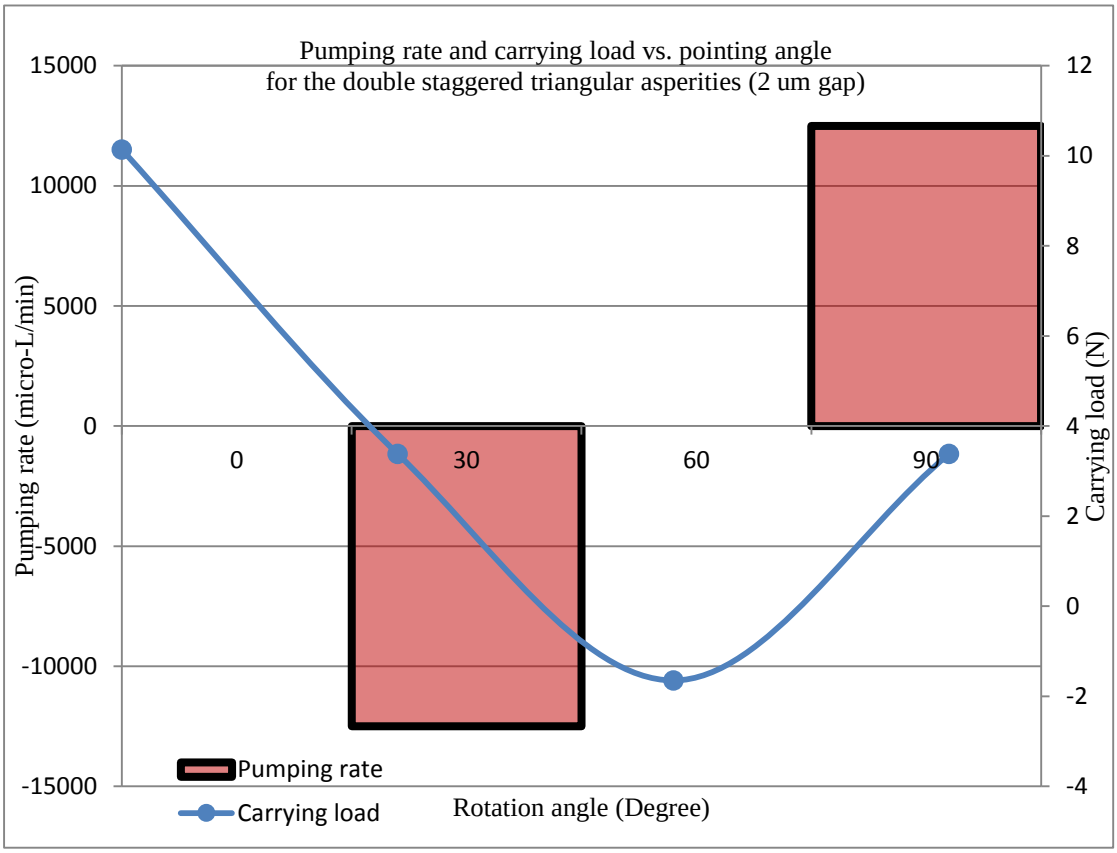

Figure 5.4.4 Pumping rate and load carrying capacity for the double staggered triangular asperities ($h_{ntri} = 2\mu m$)

5.5 Surface Triangles Coupled with the Lip Seal Model

In this section, the fluid dynamics calculation is coupled with the solid mechanics model of the lip seal which is described in details in section 3.4. According to the pilot research results like [7], [42]-[43], [49]-[53] and the study cases in the previous sections

of this chapter, the fluid calculation result is quite sensitive to the oil film thickness variation which is related to the local contact status between the elastomer and the surface textures as shown in Figure 3.4.6. For this reason the linear finite element model introduced in section 3.4 is used to study the influence of the coupling to the system.

Using the algorithm and the numeric parameters introduced in section 3.4, the axial sealing zone width (contact length) obtained from the static contact analysis is 420 μm covering about three rows of staggered surface triangles as indicated by the contact index in Fig 3.4.6. In the experiment mentioned in section 5.1, the sealing width of different seals estimated from the wear scars (as shown in Figure 1.2.3) on the elastomer using Scanning Electronic Microscope (SEM) varied from 210 μm to 635 μm, indicating a large variability due to the unique wear process of each seal. The 420 μm sealing width falls within this range. This value for the sealing zone width is also consistent with the sealing zone width of around 400 μm reported in reference [42]-[43], [49]-[53] for the worn lip seal after the "break in" stage.

In this study, the worn sealing zone width is approximated by using an elastic modulus in the lower range of that for nitrile rubber. The elastic modulus provided by the manufacturer for the nitrile rubber elastomer ranges from about 1-14 Mpa. A value of $E = 1.5$ Mpa is used in this study. Values from the higher range (e.g $E = 10.5$ Mpa) result in sealing zone widths of 100-200 μm which are consistent with previous finite element analysis results [7] for new seals. A better approach would be measuring the wear of the elastomer directly (as shown in Figure 5.5.1) and incorporate it into the FE

model as the instantaneous geometry to match the sealing zone width. However, the instantaneous wear condition is not available for the real life seal test mentioned in section 5.1.

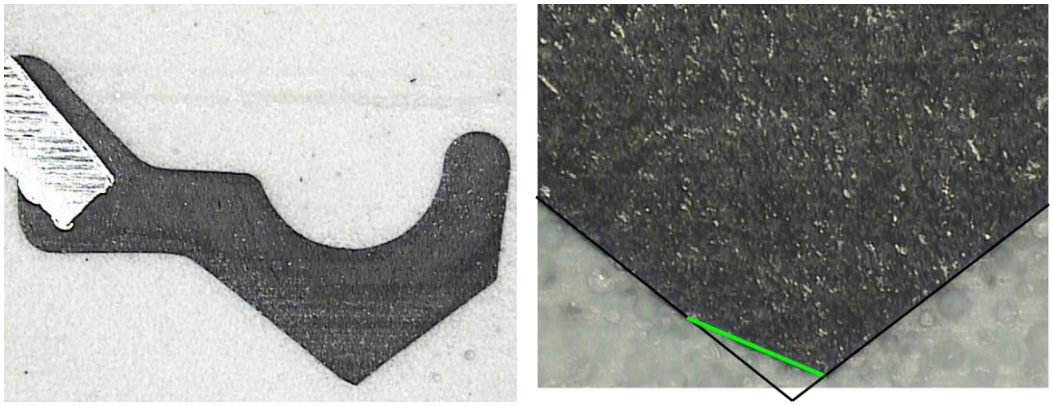

Figure 5.5.1 Worn elastomer after the “break in” stage

The fluid-solid coupling iteration starts from the status that the elastomer and the shaft are in contact as indicated by the contact index in Figure 3.4.6. An initial guessing oil film thickness is prescribed for the iteration to start. An equilibrium oil film distribution is reached after the iteration. Figure 5.5.2 shows the oil film pressure distribution around the staggered triangular surface cavities at the beginning of the iteration. The pressure distribution plot is consistent with the fluid calculation results in the previous sections that the negative fluid pressure on one side of the surface triangle is truncated by the vapor bubble (cavitation). Figure 5.5.3 shows the load capacity vs. speed and the pumping rate vs. speed curve for the seal running against the staggered triangular cavities with the rotation angle of $\theta = 90^{\circ}$ (see Figure 5.1.6). Figure 5.5.4 shows the

speed testing result for the seal running against the staggered triangular asperities with the same rotation angle of $\theta = 90^{\circ}$. By comparison, it is found that the staggered triangular cavities and the staggered triangular asperities with the same orientation pump oil to the opposite directions. The triangular cavities pointing to the air side reversely pump oil to the oil side (to their bases). It is also shown that the staggered triangular asperities provide more load capacity and pumping effect than the staggered triangular cavities especially at a high speed. The results in Figure 5.5.3 and Figure 5.5.4 are consistent with the study cases in the previous sections of this chapter, indicating that the coupling with the lip seal model does not change the directional pumping properties of the surface triangles.

The numerical model also predicts that without the elastomer roughness and the squeezing effect, neither the staggered triangular cavities nor the staggered triangular asperities pattern can generate enough hydrodynamic lifting force to counter-balance the sealing load which is $60 \sim 70\ \mathrm{N}$. The maximum supporting force generated by the staggered triangular asperities at the speed of $1000\ \mathrm{rpm}$ is about $40\ \mathrm{N}$. This means the partial contact exists between the elastomer and the shaft in the model. A $1\ \mu\mathrm{m}$ oil film thickness is assumed in the contact area when calculating the pumping rate. This assumption is physically motivated by the following "factors" 1) in the experiment introduced in section 5.1, it was observed that for the tests used for comparison the seals ran in full hydrodynamic lubrication and very minimal contact occurred as long as the sealing zone was flooded with the oil during the oil drop test; 2) as shown in [42]-[43],

[49]-[53] and later in Figure 5.5.8 (b) of this study the elastomer roughness minimizes the area in contact and provides small pumping paths among the asperities in contact; 3) the composite surface roughness measured from these seals in [84] was approximately 1 μm.

Figure 5.5.5 shows the load capacity vs. the rotation angle and the pumping rate vs. the rotation angle curves for the seal running against staggered triangular cavities. Figure 5.5.6 shows the load capacity vs. the rotation angle and the pumping rate vs. the rotation angle curves for seal running against the staggered triangular asperities. The operating speed is 750 rpm. The negative load capacity in Figure 5.5.5 is caused by the excessive presence of the cavitation in which the gauged oil pressure is $-101{,}325$ Pa. It is seen more clearly that the staggered triangular asperities tend to pump oil toward its apex as the maximum forward pumping rate occurs at the rotation angle of $\theta = 90^{\circ}$ (pointing to the air side) and the maximum reverse pumping occurs at the rotation angle of $\theta = 30^{\circ}$ (pointing to the oil side) (see Figure 5.1.6). For the staggered triangular cavities, the maximum forward pumping rate and the maximum reverse pumping rate are obtained at $\theta = 50^{\circ}$ and $\theta = 80^{\circ}$ which deviate from ideally the best pumping angle $\theta = 30^{\circ}$ and $\theta = 90^{\circ}$. The deviation is caused by the single load peak between the angle of $\theta = 60^{\circ}$ and $\theta = 70^{\circ}$ shown in Figure 5.5.5. In general, the staggered triangular cavities pump oil toward their bases. The explanation for the directional pumping ability of the surface triangles has been given in sections 5.2-5.4 and is not to be repeated here.

It is also found that when the orientation of the triangle is leading ($\theta = 0^{\circ}$) or lagging ($\theta = 60^{\circ}$) (see Figure 5.1.6), there is no significant pumping effect for either the cavity or

the asperity which is consistent with the numerical results presented in sections 5.2-5.4. This is because in the leading and the lagging cases, the triangle is symmetrical about the circumferential direction (fluid incoming direction), thus there is no significant pumping preference. Though the pumping rate at the angle of $\theta = 0^{\circ}$ and $\theta = 60^{\circ}$ is insignificant compared to the values at other orientation, there exists a small pumping rate because of the uneven axial sealing force shown in Figure 3.4.5 (a) slightly undermines the symmetry of the axial oil film distribution.

Another finding is that the surface asperity provides more load capacity and pumping effect at most of the orientations.

Finally the numerical results show that the maximum reverse pumping rate is larger than the maximum forward pumping rate for both the cavity and the asperity. In the numerical model, this is caused by the uneven axial sealing force shown in Figure 3.4.5 (a) due to the asymmetrical geometry of the seal with respect to its apex as shown in Figure 3.4.1. This finding in the numerical model also provides a reasonable explanation to the experiment observation that for both the triangular cavities and the triangular asperities, the reverse pumping rate is higher than the forward pumping rate.

In general the numerical results match the trend of the experiment results shown in Figure 5.1.7 and Figure 5.1.8 in section 5.1 as 1) the cavity pumps toward its base and the asperity pumps toward its apex; 2) the asperity pumps much more oil than the cavity; 3) the backward pumping is larger than the forward pumping. Table 1 provides the percentage difference for the pumping rate between the model and the experiment. “Cav”

means the pumping rate for the cavity cases and “Asp” means the pumping rate for the asperity cases. The pumping rate for the experiment comes from Figures 5.1.7 and 5.1.8. The pumping rate for the model comes from Figures 5.5.5 and 5.5.6.

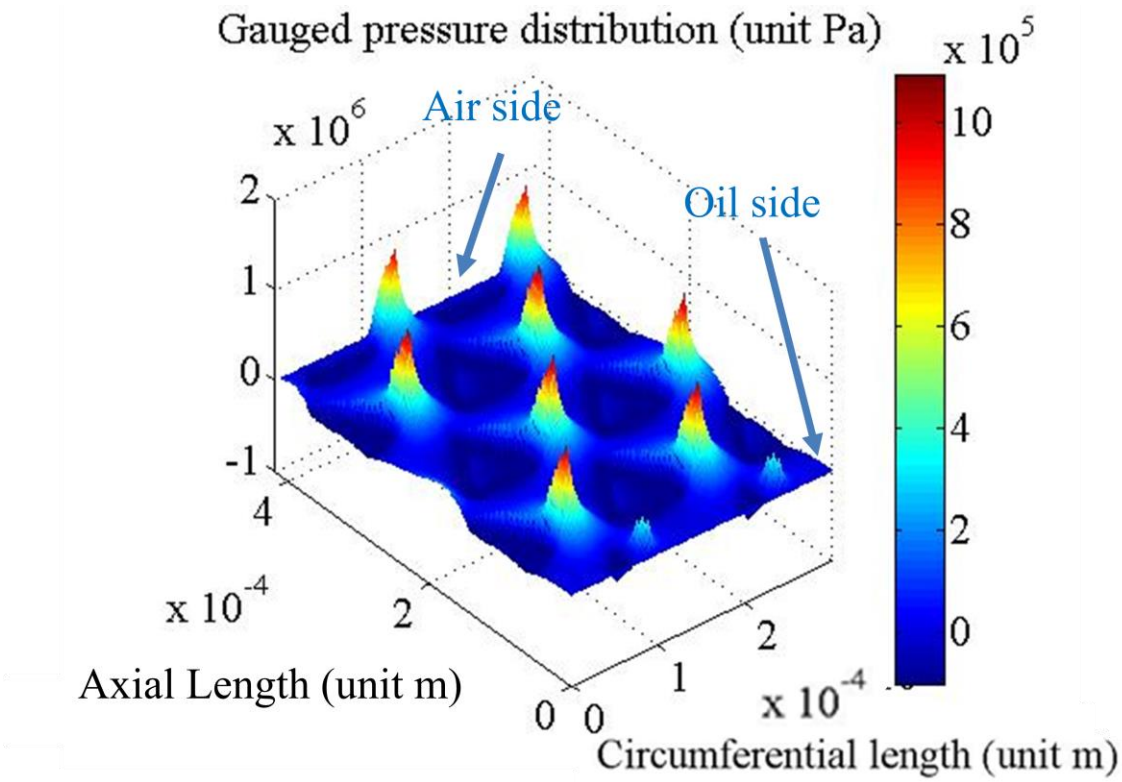

Figure 5.5.2 Gauged oil pressure distribution around the staggered triangular cavities

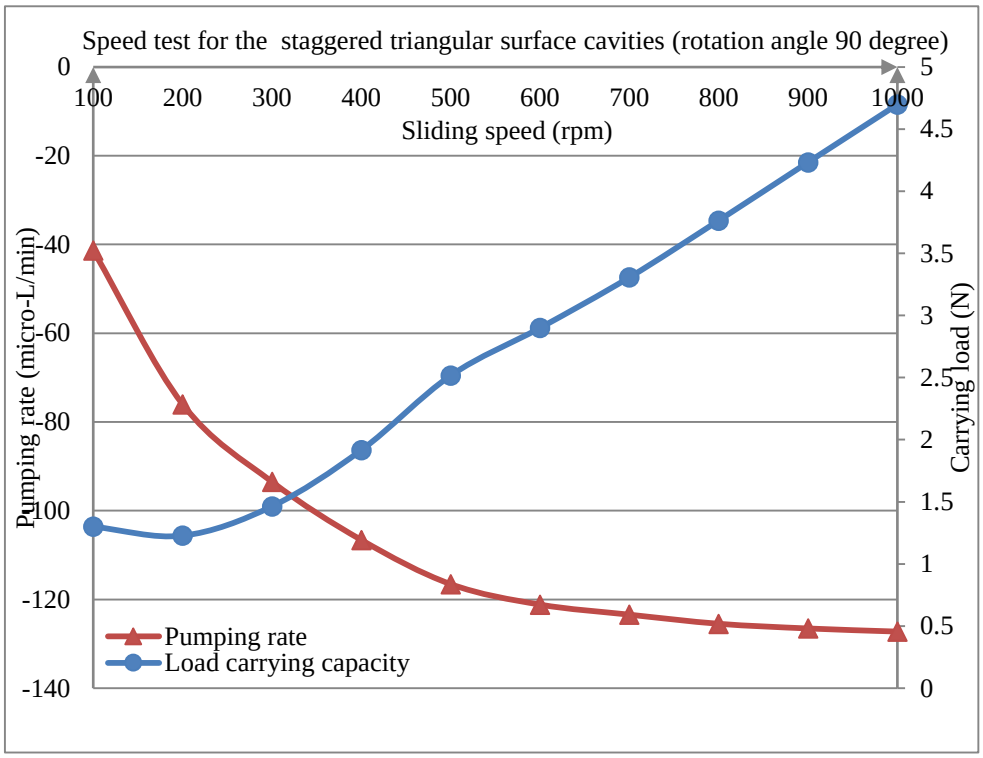

Figure 5.5.3 Shaft speed result for the triangular surface cavities

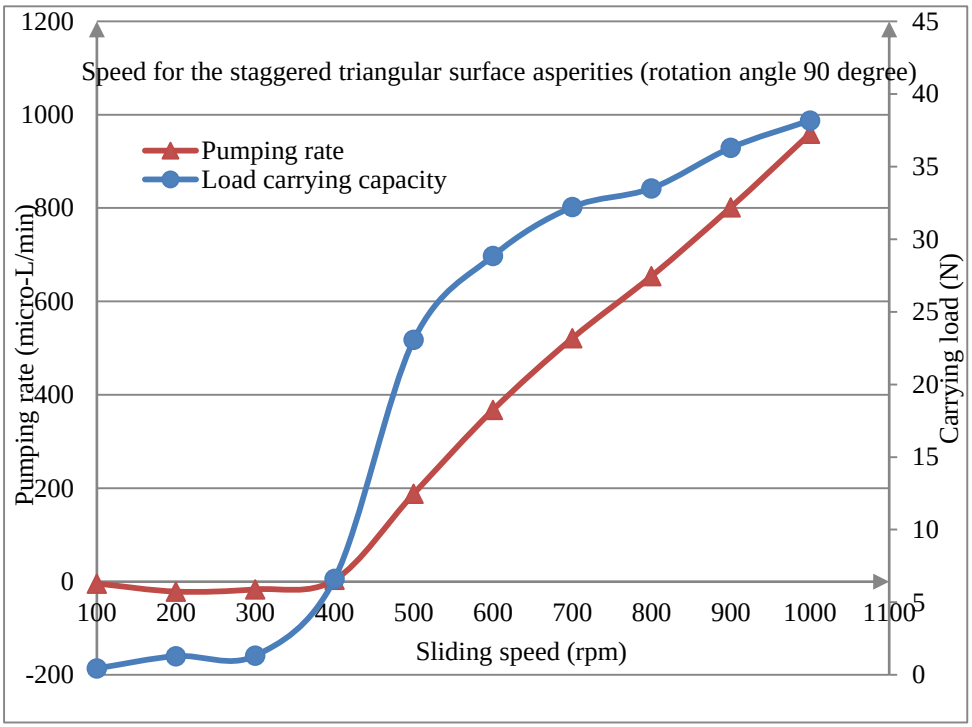

Figure 5.5.4 Shaft speed result for the surface triangular asperities

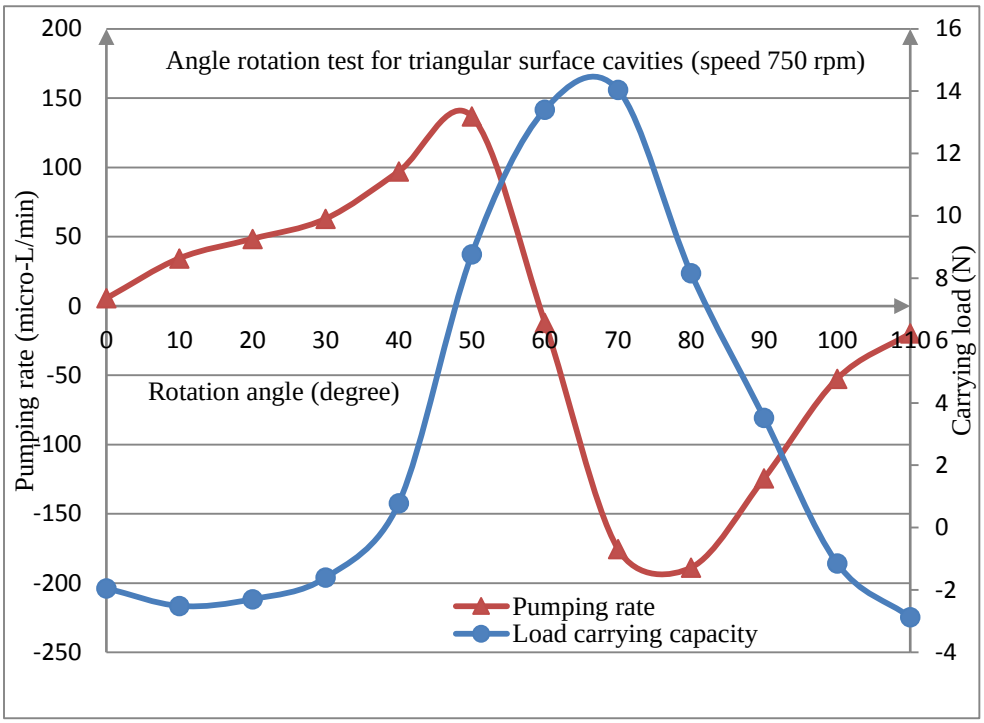

Figure 5.5.5 Angle rotation result for the triangular surface cavities

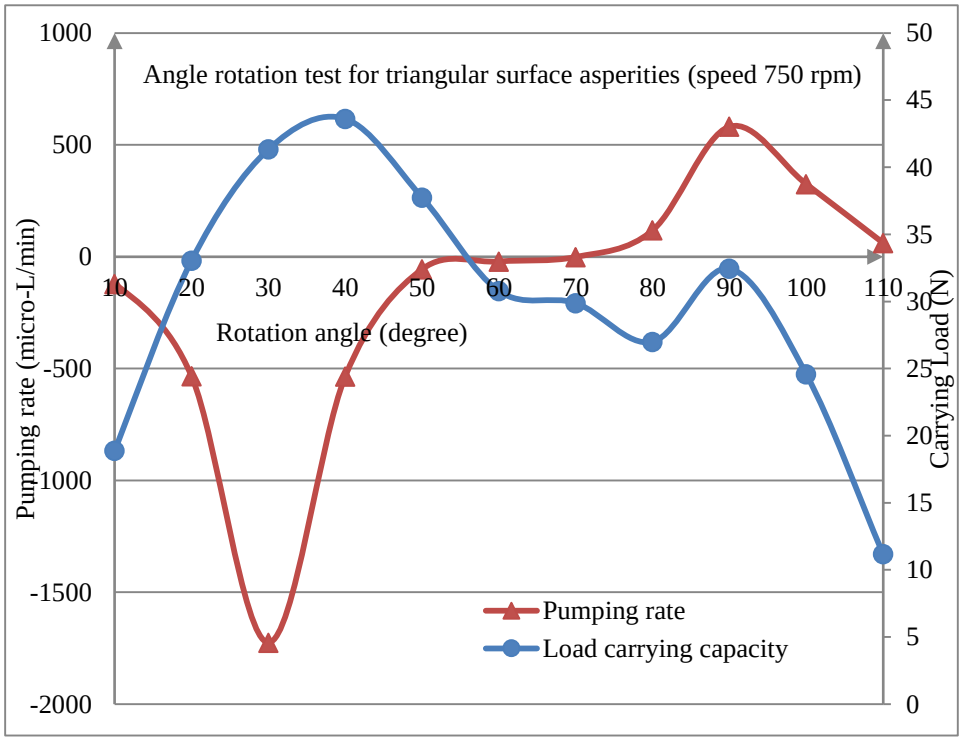

Figure 5.5.6 Angle rotation result for the triangular surface asperities

Table 1 Pumping rate comparison between the model (Figure 5.5.5 and Figure 5.5.6) and the experiment (Figure 5.1.8 and Figure 5.1.9)
(smooth elastomer)

Pumping rate (micro-L/min)	**Model**	**Experiment** (mean value)	Percentage Difference
Cav to air	-124.4	-811.5	84.7%
Cav to oil	62.9	81.5	22.8%
Cav lead	5.6	-376.6	101.5%
Cav lag	-12.0	-398.1	96.9%
Asp to air	581.5	3516.9	83.4%
Asp to oil	-1724.9	-6648.0	74.1%

Discrepancies between the model and the experiment

By checking Table 1, two discrepancies are found between the numerical results and the experimental results. The first discrepancy is that: the pumping rate taken from the experiment is larger than the pumping rate predicted by the model shown in Figure 5.5.3-Figure 5.5.6 especially for the asperity cases. There are three most possible causes:

1) A relatively small elastic modulus is used in the FE model trying to match the sealing zone width of the worn elastomer (1.5 Mpa is used instead of 10.5 Mpa), this causes the numerically softened elastomer to deform deep into the valley of the surface cavity or the surface asperity as demonstrated in Figure 5.5.7. The contact status index in Figure 3.4.6 also indicates that the elastomer touches the bottom faces of the triangular cavities and the triangular asperities. If a larger elastic modulus of 10.5 Mpa (A typical

elastomer seal value) is used in the FE model the elastomer will deform less into the valleys of the surface triangles and a larger pumping rate is expected because of a larger average oil film thickness. The impact of the material stiffness to the FE model should be especially large for the triangular asperity cases because the elastomer running against surface asperities will have a larger inter-asperity oil film thickness of around 5 μm if the elastomer does not deform into the inter-asperity space. Actually the study cases 11-14 in section 5.4 have already shown that if the rubber elastomer floats over the surface triangles but does not deformed into the valleys of them, the pumping rate from the fluid calculation would be very close to the experiment results.

2) The squeeze oil film effect is absent from the model. The squeezing effect caused by the surface triangles might provide more load carrying capacity which helps to enlarge the oil film thickness over the inter-cavity or inter-asperity pumping paths. The influence of the squeezing term was previously studied in reference [51-53] by Salant and Shen. Their conclusion is that the squeezing effect incurred by the random shaft roughness could increase the load carrying capacity of the oil film considerable, for example 37% in one study case.

3) The viscoelasticity of the material is absent from the model. In the real system, the elastomer should be hardened at a high operating speed due to the viscoelasticity. The impact of the viscoelasticity is just like the impact of the stiffer material.

Another discrepancy is that: in the model, the triangular cavities leading (0°) and the triangular cavities lagging (60°) pump very little oil (see Figure 5.1.6), while in the

experiment they reversely pumped significantly more oil than the smooth shaft did as shown in Figure 5.1.7. Warren [83] found this experimentally and attributes this phenomenon to the uneven sealing force across the sealing zone as well as the elastomer roughness.

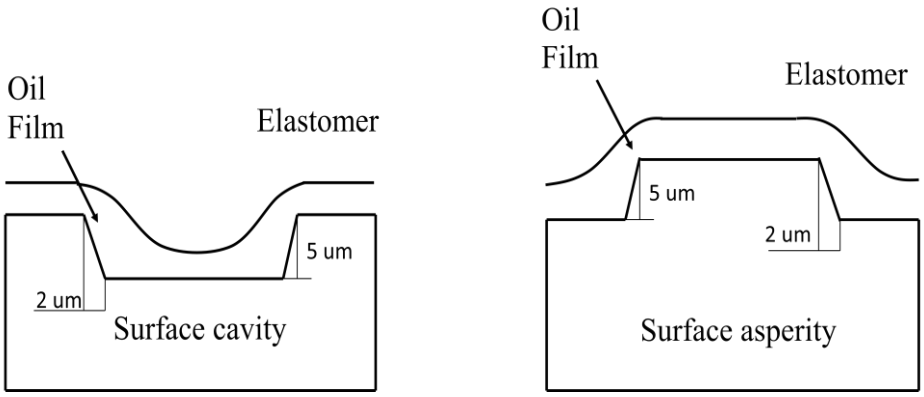

Figure 5.5.7 Elastomer surface imprints into the surface triangles

To study the impact of the rough elastomer on the pumping ability, the model is modified to include elastomer roughness. It is assumed that the elastomer roughness has the sinusoidal pattern as shown in Figure 5.5.8 (a) and described in equation (5.5.1). Figure 5.5.8 (b) shows the static contact status between the staggered triangular surface cavities and the elastomer with sinusoidal surface roughenss. The elastomer roughness used in this study is a little larger than the actual surface roughness to make the influence more obvious. Results at four orientations at the speed of 750 rpm are shown in Figure 5.5.9 for the staggered triangular cavities. It is seen that the elastomer roughness magnifies the pumping ability. This magnification effect is accompanied by an obvious

increase of the carrying load (compared to Figure 5.5.5), which helps to enlarge the clearance. The surface roughness on the seal further disrupts the axial symmetry of the oil film. Thus a larger reverse pumping is observed for the leading and the lagging cases. However, the magnitude of the reverse pumping in these two cases is still much smaller than that of the staggered triangular cavities pointing to air. Table 2 provides the percentage difference for the pumping rate between the modified model (considering the elastomer roughness) and the experiment.

The study on the elastomer roughness provides an initial explanation to the second discrepancy between the numerical model and the experiment. It is reasonable to estimate that as the accuracy of the numerical model is improved as: 1) a non-linear FEA rather than a linear FEA is employed to analyze the contact between the elastomer and the shaft 2) squeeze oil film effect is included and 3) the wear of the elastomer is measured as an primary input for the FEA, the difference for the pumping rate between the numerical model and the experiment should be reduced.

$$r(x,y) = 2.5 \times 10^{-6} \cdot \sin\left(12 \times \frac{2\pi x}{L_x}\right) \cdot \sin\left(24 \times \frac{2\pi y}{L_y}\right) \tag{5.5.1}$$

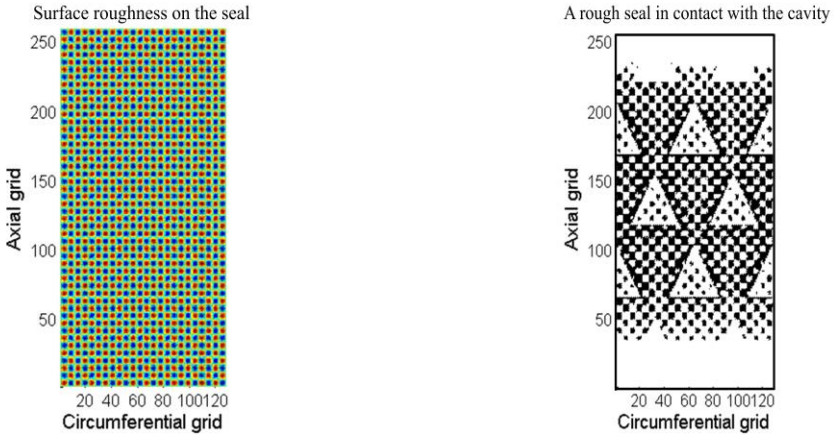

(a) (b)

Figure 5.5.8 Rough seal surface (a) and the zero speed contact status with the cavities (b)

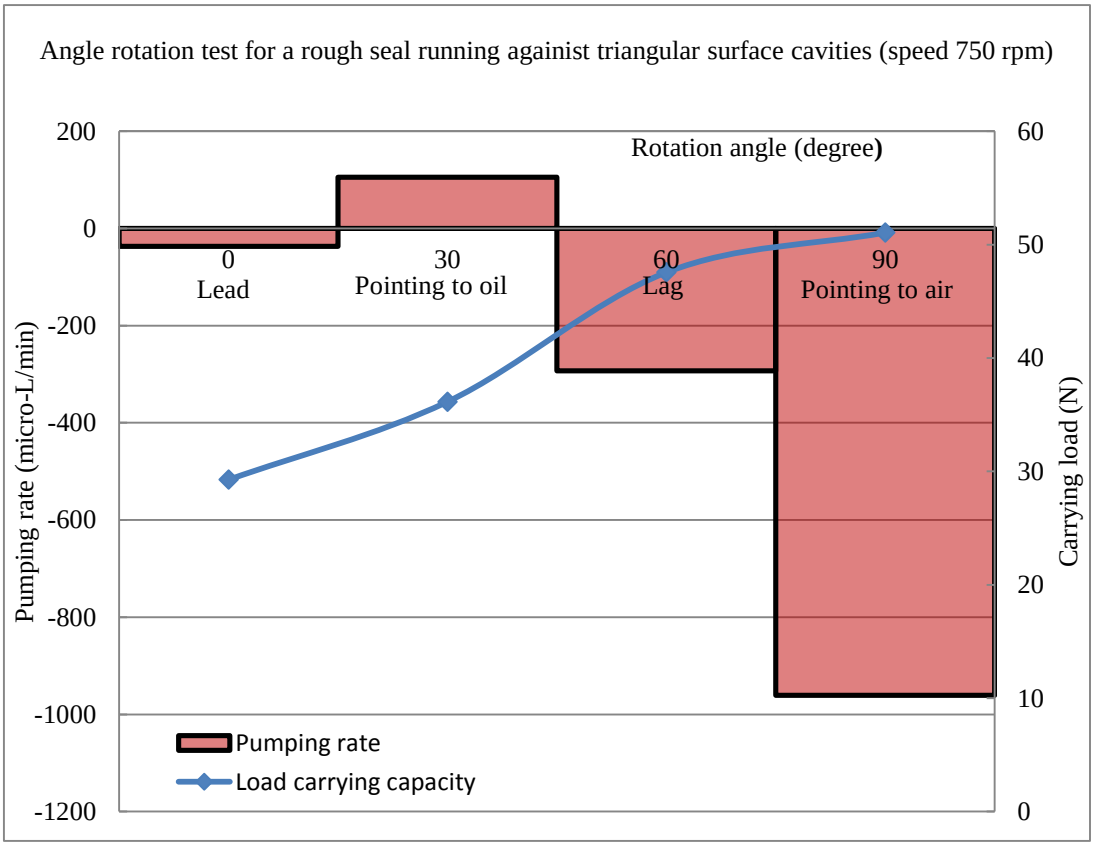

Figure 5.5.9 Angle rotation result for a rough seal against the triangular surface cavities

Table 2 Pumping rate comparison between the modified model (Figure 5.5.9) and the experiment (Figure 5.1.8)
(Rough elastomer)

Pumping rate (micro-L/min)	**Model**	**Experiment** (mean value)	Percentage Difference
Cav to air	-960.6	-811.5	−18.4%
Cav to oil	105.6	81.5	−29.6%
Cav lead	-36.7	-376.6	90.2%
Cav lag	-293.1	-398.1	26.4%

CHAPTER 6 CONCLUSIONS AND RECOMMENDATIONS FOR FUTURE WORK

6.1 Conclusions

Through the numerical study and the experimental benchmark work introduced in the previous chapters, it has been shown that it is possible to control the pumping direction of the conventional lip seal with surface textured shafts. The directional pumping mechanisms for the surface triangles have been revealed:

1) The directional pumping ability of the surface triangles are related to the vapor bubbles (cavitation) which truncates the negative fluid pressure on one side of the surface triangle creating asymmetrical pressure distribution around the surface triangle. This directional pumping mechanism has not been seen before in the surface texturing design like in reference [7].
2) The triangular surface cavities tend to pump oil toward its base.
3) The triangular surface asperities tend to pump oil toward its apex
4) The triangular surface asperities pump much more oil than the triangular surface cavities because the triangular asperities have a larger inter-asperity oil film thickness.
5) The triangular surface asperities provides much more carrying load than the triangular surface cavities because triangular asperities incur a stronger hydrodynamic effect than the triangular cavities.

6) The coupling with the lip seal does not change the directional pumping ability of the surface triangles much. However the uneven axial sealing pressure distribution across the sealing zone causes the reverse pumping rate to be larger than the forward pumping rate.

7) The reverse pumping phenomenon of the surface triangles with the pointing angle of 0° and 60° is also related to the uneven axial oil film distribution which is caused by the uneven axial sealing pressure distribution across the sealing zone. Elastomer roughness aggravates the asymmetry of the axial oil film distribution and increases the reverse pumping rate of the surface triangles with the pointing angle 0° and 60°.

The real physics beyond the lip seal running against surface textured shafts may be more complicated than the explanation 1)-7). However the findings 1)-7) prove four important things.

First, the assumption that strong viscous flow dominates the lip seal system is reasonable since the Reynolds equation gives a close prediction about the pumping rate of the lubricant flow interrupted by the surface triangles. Compared to the previous studies on the conventional lip seal [42]-[43], [49]-[53], the directional pumping phenomena for the surface triangles is more obvious and more easily captured by the numerical model.

Second, the JFO cavitation theory is important in study of the lip seal running against surface textured shafts since the main mechanism for the directional pumping of the

surface triangles is related to the vapor bubble (cavitation) of the lubricant. This cavitation related directional pumping mechanism has not been seen before. Reference [7] also studies the directional pumping ability of the shafts with sinusoidal surface textures. However in reference [7], the cavitation is not the main reason for the directional pumping but serves to provide an additional carrying load which has been introduced in section 1.1.

Third, the performance of the lip seal running against the surface textured shaft is quite sensitive to the shaft texture pattern since the solution of the Reynolds equation depends on the oil film thickness cubed, h^3. This is the unique finding of this study which covers both the triangular cavity and the triangular asperity. The gap of the pumping rate between the cavity and the asperity is very big as the cavity pumps hundreds micro-liter per minute while the asperity pumps more than five thousands micro-liter per minute. This finding means the design space left to the tribology engineer is huge. Also the design of the surface texture must be very precise to achieve the desired directional pumping ability.

Fourth, the uneven sealing pressure which is important to the functioning of the conventional lip seal [30], [31] is also proved to be important to the lip seal running against surface textured shafts. The uneven sealing pressure distribution causes the reverse pumping rate to be larger than the forward pumping rate, which is consistent to the reverse pumping theory for the conventional lip seal running against the smooth shaft.

6.2 Future Work

1) Wear plays an important role in the lip seal system. It has been introduced that for the conventional lip seal running against the smooth shaft, wear happened as a consequence of the inadequate hydrodynamic lifting force during the “break in” stage. For the conventional lip seal running against the shafts with triangular surface textures, wear still happened because of the “starvation” period of the sealing zone during the oil drop test. Wear could change the sealing pressure distribution and the total sealing load and thus influence the coupling between the solid model of the elastomer and the fluid model of the lubricant oil. At least, an empirical model for the wear of the elastomer is needed to modify the instantaneous geometry of the elastomer in the FEA. Figure 6.2.1 shows one possible quadratic time evolving pattern of the sealing zone width due to the wear of the elastomer

2) The squeeze oil film effect (the squeezing term in the Reynolds equation) should be considered. The squeeze oil film effect is not included in this study because the squeezing term in the Reynolds equation will lead to a transient analysis which requires much more computational time. However, the squeeze oil film effect is important as it might provide an extra load carrying capacity which could enlarge the oil film thickness between the elastomer and the shaft. In this study, it is seen that the surface textures on the shaft and the surface roughness on the elastomer together could not generate sufficient hydrodynamic lifting force to separate the elastomer from the shaft and partial contact always happens. The main reason for this might be the missing of the squeeze oil

film effect, which means the load carrying capacity for the shaft texture is underestimated.

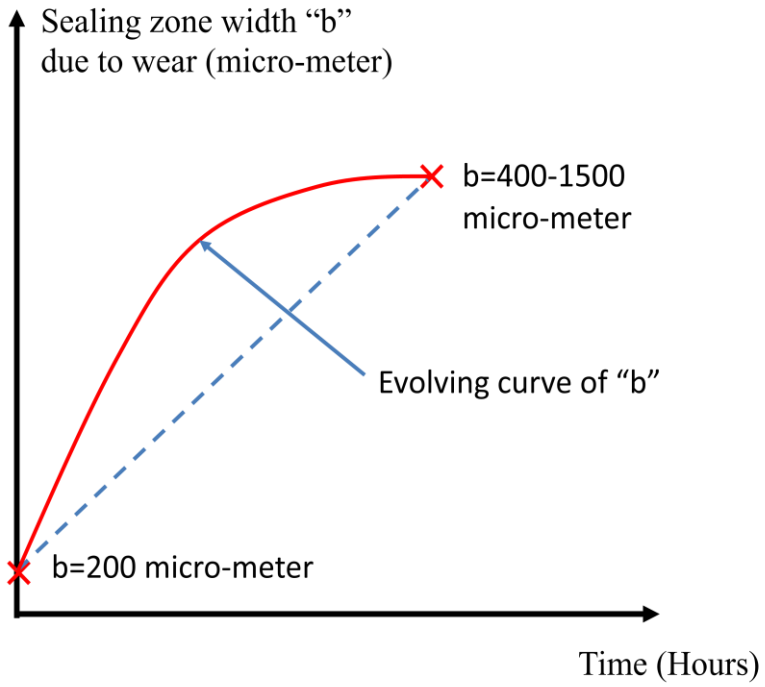

Figure 6.2.1 Sealing width evolution over time

3) A linear FE model is employed in this study for the contact analysis between the elastomer and the shaft triangles. It has been introduced in Chapter 3 that linear FEM is not accurate in predicting the large deformation of the structure. In this study, the direct consequence for employing the linear FEM is the inaccurate sealing pressure distribution across the sealing zone. According to the conclusion 6) and 7) in section 6.1, the accuracy of the axial sealing pressure distribution is fairly important. Thus a nonlinear lip seal contact model is recommended.

REFERENCES

[1] D. Shen, 2005, “Deterministic Modeling of a Rotary Lip Seal with Microasperities on The Shaft Surface,” Ph.D. dissertation, Georgia Institute of Technology, Atlanta, GA.

[2] Horve, L.A. 1996, “Shaft Seals for Dynamic Applications,” Marcel Dekker, New York, ISBN 9780824797164

[3] V. Kanakasabai, 2009, “Detailed Surface Analysis of Lip Seal Elastomers Ran Against Shafts Manufactured with Triangular Cavities,” Master thesis, University of Kentucky.

[4] I. Etsion, 2005, “State of the Art in Laser Surface Texturing,” Journal of Tribology, Vol. 127, Issue. 1, pp. 248-253.

[5] S. N. Kortikar, L. S. Stephens, P. C. Hadinata and R. B. Siripuram, 2003, “Manufacturing of Micro-asperities on Thrust Surfaces Using Ultraviolet Photolithography,” In Proceedings of the ASPE Winter Topical Meeting, Raleigh, NC, pp. 148-154

[6] L. S. Stephens, R. Sirirpuram, R. Hayden and B. McCartt, 2004, “Deterministic Micro-asperities on Bearings and Seals Using a Modified LIGA Process,” Journal of Engineering Gas Turbine Power, Vol. 126, pp. 147-154

[7] X. Jia, S. Jung, W. Haas and R. F. Salant, 2011, “Numerical Simulation and Experimental Study of Shaft Pumping by Laser Structured Shafts with Rotary Lip Seals”, Tribology International, Vol. 44, pp. 651-659.

[8] E. T. Jagger, 1957, “Rotary Shaft Seals: the Sealing Mechanism of Synthetic Rubber Seals Running at Atmospheric Pressure,” Proceedings Institution of Mechanical Engineers, Vol. 171, pp. 597-616.

[9] E. T. Jagger, 1957, “Study of the Lubrication of Synthetic Rubber Rotary Shaft Seals,” In Proceedings of the Institution of Mechanical Engineers Conference on Lubrication and wear, London, pp. 409-415.

[10] E. T. Jagger, 1957, “Study of the lubrication of synthetic rubber rotary shaft seals”, Proc. Conf. Lubric. Wear, p.409.

[11] E. T. Jagger and P. S. Walker, 1966-1967, “Further Studies of the Lubricantion of Synthetic Rubber Rotary Shaft Seals,” Proceedings of Institution of Mechanical Engineers, Vol. 181, pp. 191-204.

[12] M. Ogata, T. Fujii and Y. Shimotsuma, 1986, “Study on Fundamental Characteristics of Rotating Lip-type Oil Seals,” In Proceedings of the 13th Leeds±Lyon Symposium on Tribology, Leeds, pp. 553±560.

[13] G. Poll and A. Gabelli, 1992, “Formation of Lubricant Film in Rotary Sealing Contacts, Part Ⅱ- A New Measuring Principle for Lubricant Film Thickness,” Journal of Tribology, Vol. 114, pp. 290-297.

[14] G. Poll, A. Gabelli, P. G. Binnington and J. Qu, 1992, “Dynamic Mapping of Rotary Lip Seal Lubricant Films by Fluorescent Image Processing,” In Proceedings of the 13th BHR Group International Conference on Fluid Sealing, Brugge, Belgium, pp. 55±77.

[15] H. van Leeuwen and M. Wolfert, 1996 and 1997, “The Sealing and Lubrication Principles of Plain Radial Lip Seals: an Experimental Study of Local Tangential Deformations and Film Thickness. In Proceedings of the 23rd Leeds±Lyon Symposium on Tribology, Leeds, pp. 219-232.

[16] H. Ishiwata, 1961, “Friction and sealing characteristics of oil seals”, Paper H2, 2nd int. Conf. on Fluid Sealing (BHRA), April 1964.

[17] H. Ishiwata and F. Hirano, 1965-1966, “The lubricating condition of a lip seal”, Paper 15, Proc. Inst. Mech. Eng., 180 (d +3B): 187

[18] E. T. Jagger, 1966-1967, “Rotary shaft seals: the sealing mechanism of synthetic rubber seals running at atmospheric pressure”, Proc. Inst. Mech. Eng., Vol.181, Pt. 1, No. 9

[19] D. Hamilton, J. Walowit and C. Allen, 1966, “A Theory of Lubrication by Micro-irregularities,” Journal of Basic Engineering, ASME Transactions, Ser.D., pp. 177-185.

[20] D. E. Johnston, 1978, “Using the Frictional Torque of Rotary Shaft Seals to Estimate the Film Parameters and the Elastomer Surface Characteristics,” In Proceedings of the Eighth BHRA International Conference on Fluid Sealing, Durham, paper C1 (BHRA, Cranfield, Bedfordshire).

[21] L. Horve, 1991, “The Correlation of Rotary Shaft Radial Lip Seal Service Reliability and Pumping Ability to Wear Track Roughness and Micro-asperity Formation” In Proceedings of the SAE international congress and Exposition Detroit, Paper 910530

[22] K. Nakamura and Y. Kawahara, 1984, “An Investigation of Sealing Properties of Lip Seals through Observations of Sealing Surfaces under Dynamic Condition. In Proceedings of the Tenth BHRA International Conference on Fluid Sealing, Innsbruck, Austria, pp. 87-105.

[23] M. J. L. Stakenborg, 1988, “On the Sealing Mechanism of Radial Lip Seals,” Tribology International, Vol. 21, pp. 335-340.

[24] H. Hirabayashi and Y. Kawahara, 1977, “A study of sealing phenomena on oil seals”, ASLE, 77 LC-5A-2

[25] Y. Kawahara and H. Hirabayshi, 1978, “An analysis of sealing phenomena on oil seals”, Trans. ASLE, 23:1

[26] L. A. Horve, 1992, “Keynote Address: Understanding the sealing mechanism of the radial lip seal for rotating shafts”, 13th Int. Conf. on Fluid Sealing (BHR)

[27] Y. Kawahara, M. Abe and H. Hirabayshi, 1980, “An Analysis of Sealing Characteristics of Oil Seals,” ASLE Transactions, 1980, Vol.23, pp. 93-102.

[28] K. Nakamura, 1981, “Sealing Mechanism of Rotary Shaft Lip-type Seals,” Tribology International, Vol. 20, pp. 90-101.

[29] M. Iwasaki, 1974, “A study on lip type oil seals (Report 1)---pressure distribution characteristics”, Junkastsu (Lubrication), 19

[30] M. Kammüller, 1986, “Zur Abdichtwikung von Radial-Wellendichtrigen”, Dr.-Ing. Thesis, Universität Stuttgart

[31] H. K. Müller, 1987, ‘‘Concepts of Sealing Mechanism of Rubber Lip Type Rotary Shaft Seals,’’ Proc. 11th BHRA International Conference on Fluid Sealing, B. S. Nau, ed., Elsevier, London, UK, pp. 698–709.

[32] L. A. Horve, 1987, “A Macro-scope view of the sealing phenomenon for radial lip oil seals”, Paper K2, 11th Inter. Conf. on Fluid Sealing (BHR)

[33] L. Floberg and B. Jakobsson, 1957, “The Finite Journal Bearing Considering Vaporization,” Transactions of Chalmers University of Technology, Vol. 190, Gutenberg, Sweden

[34] K. Olsson, 1965, “Cavitation in Dynamically Loaded Bearings,” Transactions of Chalmers University of Technology, Vol. 308, Gutenberg, Sweden

[35] H. Elrod and M. Adams, 1974, “A Computer Program for Cavitation and Starvation Problems,” Cavitation and Related Phenomena in Lubrication, Mechanical Engineering Publications, New York, pp. 37-41.

[36] H. Elrod, 1981, “A Cavitation Algorithm”, Journal of Lubrication Technology, Vol.103, Issue 3, pp. 350-354.

[37] D.Vijayaraghavan and T.G.Ketith,JR, 1989, “Development and Evaluation of Cavitation Algorithm,” Tribology Transactions, Vol. 32, pp. 225-233.

[38] D.Vijayaraghavan and T.G.Ketith,JR, 1990, “An Efficient, Robust and Time Accurate Numerical Procedure Applied to a Cavitation Algorithm,” Journal of Tribology, Vol. 112, Issue. 1, pp. 44-51.

[39] D.Vijayaraghavan and T.G.Ketith,JR, 1990, “Grid Transformation and Adaption Techniques Applied in the Analysis of Cavitated Journal Bearings,” Journal of Tribology, Vol. 112, Issue. 1, pp. 52-59.

[40] D.Vijayaraghavan and T.G.Ketith,JR, 1990, “Analysis of a Finite Grooved Misaligned Journal Bearing Considering Cavitation and Starvation Effects,” Journal of Tribology, Vol. 112, Issue. 1, pp. 60-67.

[41] D. E. Brewe, 1989, “Theoretical Modeling of the Vapor Cavitation in Dynamically Loaded Journal Bearings,” Journal of Tribology, Vol. 108, pp. 628-639.

[42] R. F. Salant and A. L. Flaherty, 1994, “Elastohydrodynamic Analysis of Reverse Pumping in Rotary Lip Seals with Microundulations,” Journal of Tribology, Vol. 116, pp. 56-62.

[43] R. F. Salant and A. L. Flaherty, 1995, ‘‘Elastohydrodynamic Analysis of Reverse Pumping in Rotary Lip Seals with Microasperities,’’ Journal of Tribology, Vol. 117, pp. 53–59.

[44] K. Tønder and R. F. Salant, 1992, “Non-leaking Lip Seals: a Roughness Effect Study,” Journal of Tribology, Vol. 114, pp. 595-599.

[45] N. Patir and H. S. Cheng, 1978, “An Average Flow Model for Determining Effects of Three Dimensional Roughness on Partial Hydrodynamic Lubrication,” Journal of Lubrication Technology, Vol. 100, pp. 12-17.

[46] N. Patir and H. S. Cheng, 1979, “Application of the Average Flow Model to Lubrication between Rough Sliding Surfaces,” Journal of Lubrication Technology, Vol. 101, pp. 220-229.

[47] R. F. Salant and A. H. Rocke, 2004, “Hydrodynamic Analysis of the Flow in a Rotary Lip Seal Using Flow Factors,” Journal of Tribology, Vol.126, pp.156-161.

[48] R. S. Harp and R. F. Salant, 2001, “An Average Flow Model of Rough Surface Lubrication with Inter-asperity Cavitation,” Journal of Tribology, Vol. 123, pp. 134-143.

[49] F. Shi and R. F. Salant, 2000, “A Mixed Soft Elastohydrodynamic Lubrication Model with Interasperity Cavitation and Surface Shear Deformation,” Journal of Tribology, Vol. 122, pp. 308–16.

[50] F. Shi and R. F. Salant, 2001, “Numerical Study of a Rotary Lip Seal with a Quasi-random Sealing Surface,” Journal of Tribology, Vol. 123, pp. 517–24.

[51] D. Shen and R. F. Salant, 2003, “Elastohydrodynamic Analysis of the Effect of Shaft Surface Finish on Rotary Lip Seal Behavior,” Tribology Transactions, Vol. 46, pp. 391-396.

[52] D. Shen and R. F. Salant, 2006, “A Transient Mixed Lubrication Model of a Rotary Lip Seal with a Rough Shaft,” Tribology Transactions, Vol. 49, pp. 621-634

[53] D. Shen and R. F. Salant, 2007, “An Unsteady Mixed Soft EHL Model, with Application to a Rotary Lip Seal,” Tribology International, Vol. 40, pp. 646-651.

[54] Hai Sui, Heiko Pohl, Uwe Schomburg, Gerd Upper and Steffen Heine, 1999, “Wear and Friction of PTFE seals,” Wear, Vol. 224, pp. 175-182.

[55] A. Yang, C. Wen and C. Tseng, 2009, “Analysis of Flow Field Around a Ribbed Helix Lip Seal,” Tribology International, Vol. 42, pp. 649-656.

[56] K. L. Johnson, 1985, Contact mechanics, Cambridge University Press

[57] J.A. Greenwood and J.H. Tripp, 1967, “Contact of Nominally Flat Surfaces” ASME, Journal of Applied Mechanics, Vol, 134, pp. 153.

[58] Y. Ju and L. Zheng, 1992, “A Full Numerical Solution for the Elastic Contact of Three Dimensional Real Rough Surfaces,” Wear, Vol. 157, pp.151-161.

[59] Y. Ju and T. N. Farris, 1996, “Spectral Analysis of Two-Dimensional Contact Problems”, Journal of Tribology, Vol. 118, pp. 320-328.

[60] H. M. Stanley and T. Kato, 1997, “An FFT-Based Method for Rough Surface Contact,” Journal of Tribology, Vol. 119, pp. 481-485.

[61] S. Liu, Q. Wang and G. Liu, 2000, "A Versatile Method of Discrete Convolution and FFT (DC-FFT) for Contact Analyses," Wear, Vol. 243, pp. 101-111.

[62] G. Liu, Q. Wang and S. Liu, 2001, "A Three-Dimensional Thermal-Mechanical Asperity Contact Model for Two Nominally Flat Surfaces in Contact," Journal of Tribology, Vol. 123, pp. 595-602.

[63] S. Liu and Q. Wang, 2001, "A Three-Dimensional Thermo-mechanical Model of Contact between Non-Conforming Rough Surfaces," Journal of Tribology, Vol. 123, pp. 17-26.

[64] W. W. Chen, S. Liu, Q.J. Wang, 2008, "Fast Fourier Transform Based Numerical Methods for Elasto-Plastic Contacts of Nominally Flat Surfaces," Journal of Applied Mechanics, Vol. 75, pp. 011022-1-011022-11.

[65] N. Ren, D. Zhu, W. W. Chen, Y. Liu and Q. J. Wang, 2009, "A Three Dimensional Deterministic Model for Rough Surface Line-Contact EHL Problems," Journal of Tribology, Vol. 131, pp. 011501-1-011501-9

[66] M. Hajjam and D. Bonneau, 2004, "Elastohydrodynamic Analysis of Lip Seals with Microundulations," Proc. IMechE, Part J: J.Engineering Tribology, Vol. 218, pp. 13-21.

[67] R. F. Salant, 1997, "Rotary Lip Seal Operation with an Ingested Meniscus," Journal of Tribology, Vol. 119, pp. 205-210.

[68] A. Gabelli, 1988, "Micro-elastohydrodynamic Lubricant Film Formation in Rotary Lip Seal Contacts," In proceedings of the 15th Leeds-Lyon Symposium on Tribology, Leeds, pp. 57-68.

[69] I. Etsion, Y. Kligerman and G. Halperin, 1999, "Analytical and Experimental Investigation of Laser-Textured Mechanical Seal Faces," Tribology Transactions, Vol. 42, Issue. 3, pp. 511-516.

[70] A. Ronen, I. Etsion and Y. Kligerman, 2001, "Friction-Reducing Surface Texturing in Reciprocating Automotive Components," Tribology Transactions, Vol. 44, Issue. 3, pp. 359-366.

[71] G. Ryk, Y. Kligerman and I. Etsion, 2002, “Experimental Investigation of Laser Surface Texturing for Reciprocating Automotive Components,” Tribology Transactions, Vol. 45, Issue. 4, pp. 444-449.

[72] V. Brizmer, Y. Kligerman and I. Etsion, 2003, “A Laser Surface Textured Parallel Thrust Bearing,” Tribology Transactions, Vol. 46, Issue. 3, pp. 397-403.

[73] I. Etsion, G. Halperin, V. Brizmer and Y. Kligerman, 2004, “Experimental Investigation of Laser Surface Textured Parallel Thrust Bearings,” Tribology Letters, Vol. 17, pp. 295-300.

[74] G. Ryk, Y. Kligerman, I. Etsion and A. Shinkarenko, 2005, “Experimental Investigation of Partial Laser Surface Texturing for Piston Rings Friction Reduction,” Tribology Transactions, Vol. 48, Issue. 4, pp. 583-588.

[75] G. Ryk and I. Etsion, 2006, “Testing Piston Rings with Partial Laser Surface Texturing for Friction Reduction,” Wear, Vol. 261, pp. 792-796.

[76] I. Etsion and E. Sher, 2009, “Improving Fuel Efficiency with Laser Surface Textured Piston Rings,” Tribology International, Vol. 42, pp. 542-547.

[77] A. Shinkarenko, Y. Kligerman and I. Etsion, 2009, “The Effect of Surface Texturing in Soft Elasto-Hydrodynamic Lubrication,” Tribology Letter, Vol. 36, pp. 95-103.

[78] A. Shinkarenko, Y. Kligerman and I. Etsion, 2009, “The Effect of Surface Texturing in Soft Elasto-hydrodynamic Lubrication,” Tribology International, Vol. 42, pp. 284-292.

[79] A. Shinkarenko, Y. Kligerman and I. Etsion, 2010, “Theoretical Analysis of Surface-Textured Elastomer Sleeve in Lubricated Rotary Sliding,” Tribology Transactions, Vol. 53, pp. 376-385.

[80] A. Shinkarenko, Y. Kligerman and I. Etsion, 2009, “The Validity of Linear Elasticity in Analyzing Surface Texturing Effect for Elastohydrodynamic Lubrication”, Journal of Tribology, Vol. 131, pp. 021503-1-021503-7.

[81] R. B. Siripuram and L. S. Stephens, 2004, "Effect of Deterministic Asperity Geometry on Hydrodynamic Lubrication," Journal of Tribology, Vol. 126, pp. 527-534.

[82] J. Paige and L. S. Stephens, 2004, "Surface Characterization and Experimental Design for Testing of a Radial Lip Seal," Tribology Transactions, Vol. 47, Issue. 3, pp. 341-355.

[83] K. H. Warren and L. S. Stephens, 2009, "Effect of Shaft Microcavity Patterns for Flow and Friction Control on Radial Lip Seal Performance-A Feasibility Study," Tribology Transactions, Vol. 52, pp. 731-743.

[84] V. Kanakasabai, K. H. Warren and L. S. Stephens, 2010, "Surface Analysis of the Elastomer in Lip Seals Run against Shafts Manufactured with Micro-cavity Patterns," Proc. IMechE, Part J: J.Engineering Tribology, Vol. 224, pp. 723-736.

[85] D. M. Impellizzeri, 2006, "Model Development and Investigation of Micro-Deterministic Asperity Features/Textures Using the Jakobsson-Floberg-Olsson (JFO) Cavitation Condition Modified Reynolds Equation," M.S. Thesis, University of Kentucky, Lexington, KY.

[86] P. C. Hadinata and L. S. Stephens, 2007, "Soft Elastohydrodynamic Analysis of Radial Lip Seals with Deterministic Microasperities on the Shaft," Journal of Tribology, Vol. 129, Issue. 4, pp. 851-859.

[87] T. Belytschko, W. K. Liu and B. Moran, 2001, "Nonlinear Finite Elements for Continua and Structures", ISBN 0-471-98774-3

[88] Y.C.Fung and Pin Tong, 2007, "Classical and Computational Solid Mechanics," World Scientific Publishing Co. Pte. Ltd. ISBN-9789810241247.

[89] J. M. McDonough, "Lectures in elementary fluid dynamics: physics, mathematics and applications," Department of mechanical engineering and mathematics, University of Kentucky.
http://www.engr.uky.edu/~acfd/lecturenotes1.html

[90] Susan R. Harp, "A computational method for evaluating cavitating flow between rough surfaces," Ph.D. dissertation, Department of mechanical engineering, Georgia Institute of Technology, Atlanta, GA.

[91] J. M. McDonough, "Lectures in basic computational numerical analysis," Department of mechanical engineering and mathematics, University of Kentucky. http://www.engr.uky.edu/~acfd/lecturenotes1.html

[92] J. M. McDonough, "Computational Numerical Analysis of Partial Differential Equations", Departments of Mechanical Engineering and Mathematics, University of Kentucky.
http://www.engr.uky.edu/~acfd/lecturenotes1.html

[93] W. H. Press, S. A. Teukolsky, W. T.Vetterling and B. P. Flannery, "Numerical Recipes", Cambridge University Press, ISBN 9780521430647

[94] M. Arghir, N. Roucou, M. Helene and J. Frene, 2003, "Theoretical Analysis of the Incompressible Laminar Flow in a Macro-Roughness Cell," Journal of Tribology, Vol. 125, pp. 309-318.

[95] F. Sahlin, S. B. Glavatskih, T. Almqvist and R. Larsson, 2005, "Two Dimensional CFD Analysis of Micro-Patterned Surfaces in Hydrodynamic Lubrication," Journal of Tribology, Vol. 127, pp. 96-102

[96] A. de Kraker, Ron A. J. van Ostayen, A. van Beek and D. J. Rixen, 2007, "A Multi-scale Method Modling Surface Texture Effects", Journal of Tribology, Vol. 129, pp. 221-230

[97] Y. Feldman, Y. Kligerman, I. Etsion and S. Haber, 2006, "The Validity of the Reynolds Equation in Modeling Hydrostatic Effects in Gas Lubricated Textured Parallel Surfaces," Journal of Tribology, Vol. 128, pp. 345-350.

[98] M. B. Dobrica and M. Fillon, 2008, "About the Validity of Reynolds Equation and Inertia Effects in Textured Sliders of Infinite Width", Proceedings of the Institution of Mechanical Engineers - Part J: Journal of Engineering Tribology, Vol. 223, pp. 69–78.

[99] L. Gao and R. Hewson, 2012, "A Multiscale Framework for EHL and Micro-EHL," Tribology Transactions, 55, pp. 713-722.

[100] P. Brajdic-Mitidieri, A. D. Gosman, E. Loannides and H. A. Spikes, "CFD Analysis of a Low Friction Pocketed Pad Bearing," Journal of Tribology, Vol. 127. pp. 803-812.

[101] R. K. Avva, A. Singhal, and D. H. Gibson, 1995, "An Enthalpy Based Model Of Cavitation," Cavitation and Gas-Liquid Flow in Fluid Machinery and Devices (ASME FED), Vol. 226, pp. 63–70.

[102] P. D. Schmidt, C. J. Rutland and M. L. Corradini, 1999, "A Fully Compressible Two-Dimensional Model of Small, High Speed, Cavitating Nozzles," Atomization Sprays,Vol.9, pp.255-276.

[103] S. Yoshimoto, M. Yamamoto and K. Toda, 2007, "Numerical Calculations of Pressure Distribution in the Bearing Clearance of Circular Aerostatic Thrust Bearings with a Single Air Supply Inlet," Journal of Tribology, Vol. 129, pp. 384-390.

[104] Z. Luan and M. M. Khonsari, 2006, "Numerical Simulations of the Flow Field Around the Rings of Mechanical Seals," Journal of Tribology, Vol. 128, pp. 559-565.

[105] F. Billy, M. Arghir and G. Pineau, 2006, "Navier-Stokes Analysis of a Regular Two-Dimensional Roughness Pattern Under Turbulent Flow Regime," Journal of Tribology, Vol. 128, pp. 122-130.

[106] M. Hartinger, M. L. Dumont, S. Loannides, D. Gosman and H. Spikes, 2008, "CFD Modeling of a Thermal and Shear-Thinning Elastohydrodynamic Line Contact," Journal of Tribology, Vol. 130, pp. 041503-1:041503-16

[107] T. Almqvist and R. Larsson, 2002, "The Navier-Stokes Approach for Thermal EHL Line Contact Solutions," Tribology International, Vol. 35, pp. 163–170.

[108] D. Dowson, and G. R. Higginson, 1977, Elastohydrodynamic Lubrication, Pergamon, Oxford.

[109] Müller, H.K. and Nru, B.S.,1998, “Fluid Sealing Technology”, Marcel Dekker, Inc., New York.

VITA

Wei Li was born in NanJing, JiangSu, China on January 11, 1982. He received the degree of Bachelor of Science in Mechanical Engineering from Southeast University, NanJing, China, 2004. He worked as a graduate level research assistant from 2005 to May, 2007 in the Department of Mechanical Engineering at Southeast University, NanJing, China.

In August 2007, he enrolled in the graduate school at the University of Kentucky. During his graduate years at the University of Kentucky, he has 4 (first author) conference proceeding publications and 1 journal article (first author).